UNIVERSITY OF OKLAHOMA

GRADUATE COLLEGE

SEISMIC FACIES CLASSIFICATION OF THE LOWER STRAWN FORMATION, BEND-ARCH, FORT WORTH BASIN, NORTH CENTRAL TEXAS

A THESIS

SUBMITTED TO THE GRADUATE FACULTY

in partial fulfillment of the requirements for the

Degree of

MASTER OF SCIENCE

By

ENKAR DAVID PRADO BARROS
Norman, Oklahoma
2016

SEISMIC FACIES CLASSIFICATION OF THE LOWER STRAWN FORMATION, BEND-ARCH, FORT WORTH BASIN, NORTH CENTRAL TEXAS

A THESIS APPROVED FOR THE
CONOCOPHILLIPS SCHOOL OF GEOLOGY AND GEOPHYSICS

BY

_____
Dr. Roger Slatt, Chair

_____
Dr. Kurt Marfurt

_____
Dr. Matthew J. Pranter

To God for guiding me through all steps in my life and provide all that I always need.

To my wife Yamile for being my strong support during this adventure.

To my parents, my brother George and my sister Camila who have been passing through many challenging times during my time at OU.

"God is Good all times"

"Have I not commanded you? Be strong and courageous. Do not be afraid; do not be discouraged, for the Lord your God will be with you wherever you go."

Joshua 1:9

Acknowledgements

I would like to thank Dr. Slatt for everything; his kindness, generosity, great heart, and obviously for all the knowledge, advise and financial support during my time here at OU. God bless you Dr Slatt.

Also to my committee members, Dr. Marfurt, and Dr. Pranter for all their guidance.

I would like to thank Lennon Infante, Tao Zhao for their support and for having shared time and knowledge during this project.

I would like to thank all other friends that gave me their support: Javier Tellez, Carlos Molinares, Emilio Torres, Tobi Olorunsola, Henry Galviz, Daniela Becerra and many others.

Also, I would like to thank Schlumberger and Hamson-Russelll for providing the software licenses used in this thesis.

I would like to thank the owner of the data set for providing access to the seismic and well data.

Additionally, I am very thankful with the “New Star Family Church” who really were our family during this time in Norman. Thank you Pastors Steve, Santos, Jessica and Yamile (my wife who was ordered as pastor here). And all other members of this great Church.

Special thanks to my aunt “Tere” in Arlington Texas and to my friend Xinliang Zhang “James” and his wife Annie in Houston.

Table of Contents

List of Figures

Abstract

The Bend Arch- Fort Worth Basin is a tectonically active area along north-central Texas that exhibits a complex sediment distribution. While Pennsylvanian plays have been one of the main exploratory targets, the depositional history and 3D seismic expression of the Desmoinesian Lower Strawn Formation described by Van-wagoner (1975), Gun (1979) and Pranter (1989) as a turbidite / submarine fan complex is only partially documented. In this thesis, a post-stack 3D seismic volume was conditioned to structural oriented filtering and time-frequency domain-based spectral balancing from which a set of attributes were extracted, including P-impedance, and other elastic attributes that were computed once S-impedance was predicted. Appropriate attributes were then used for unsupervised facies classification with the aim of geometrically differentiating sand bodies and architectural elements present along the Lower Strawn. After data conditioning, a suite of candidate attributes was computed. The next "exploratory data analysis" step involved comparing candidate attributes to areas where well control showed the desired sand to be present or absent. Analysis showed that several of the eight texture attributes that measure the lateral homogeneity, entropy, and other properties of the reflector exhibited value. To simplify the classification, these eight measures were reduced into one represented by the first principal component. The resulting five attributes used in classification were P-impedance, precondition seismic amplitude, peak spectral frequency (from the time-frequency analysis), the first principal component of the eight texture attributes, and the relative stratal location. The same analyses were performed to simplify ten elastic attributes. Five different classification techniques (supervised and unsupervised) were evaluated with the goal of comparing a diverse set of results: K-means clustering analysis, Self-organizing Maps

(SOM), Principal Component Analysis (PCA) Generative Topographic Maps (GTM), and Principal Support Vector Machines (PSVM). The results show that some classification techniques can highlight architectural elements better than others. Although K-means and GTM were able to highlight possible channels, SOM, and PSVM, were able to discriminate more subtle facies changes along a specific area (sinuous sand bars-, fans, and possible crevasse splays features). It was the PSVM supervised classification through its binary discrimination (sandstone vs mudstone), combined with key attributes that showed strong correspondence with the evolution of geomorphological features (architectural elements), which led the interpretation of the multiple sediment source areas that compose the target sandstones of the Lower Strawn Formation.

Chapter 1: Introduction

The Bend Arch-Fort Worth Basin, located in north-central Texas (Figure 1), is a mature petroleum province where the first indication of hydrocarbons were shows of oil and gas in wells drilled during the mid to late 1800's. The first commercial oil accumulations were discovered in the early 1900's. Since then it has been intensely drilled reaching a mature stage in the late 1960's. Before the 1990's much of the commercially viable hydrocarbons production was from Pennsylvanian age reservoirs such as the Cisco, Canyon, Strawn, Wichita, Bend, and Marble Falls Groups (Ball and Perry, 1996); however, more recently with the development of the Mississippian Barnett Shale as an unconventional play the spectrum of targeted units has changed.

The Bend Arch extends north from the Llano Uplift; it is a broad subsurface, north-plunging, positive structure formed as a hinge line by down-warping of its eastern flank. This was due to subsidence of the Fort Worth Basin during early stages of development of the Ouachita structural belt in the Late Mississippian, combined with west tilting in the late Paleozoic which resulted in the formation of the Midland Basin (Pollastro et al, 2007). Thus, the Bend Arch is a flexure and structural high that formed without being actively uplifted and did not act as a physical barrier to sediment transport or as a sediment source (Thompson, 1982). The Bend Arch represents the major and final westernmost hinge line of the present-day Fort Worth Basin (Walper, 1977, 1982; Tai, 1979).

On the most northwest corner of the Bend Arch-Fort Worth Basin area, another structural element is present, named the Knox-Baylor Trough. Gun (1979) presented this feature as a sub-basin of Desmoinesian age located in north-central Texas south to the Red River Arch, northwest of the Concho platform, and west of the Bend Arch (Figure 2). It was

formed by the disruption of the Fort Worth Basin depositional systems caused by major movement along the Ouachita fold belt during the early-middle Pennsylvanian. The result was the movement of the Desmoinesian depositional center towards the west acting as an avenue for the sediments derived from the Muenster-Red River Arch complex and transported towards the Midland Basin (Lovick, Mazzine, and Kotila, 1982). According to Gun (1979), within this trough two distinct depositional systems can be separated. 1) Fluvio Deltaic and 2) Deep-water. Stratigraphically these two styles of deposition correspond to the Strawn Group in which the Lower Strawn is related to the underlying Atoka Group in lithology and distribution, and the middle and upper Strawn are related to the Canyon Group in terms of depositional history and facies represented. (Turner, 1957; Brown et al, 1973).

The Atoka and lower Strawn constitute basin fill for the Fort Worth Basin and were not deposited beyond the western flank of the basin. Fan deltas and slope depositional systems (including turbidite deposits) make up most of the basin fill (Brown et al, 1973). These deep water deposits have a lack of published information due to the unknown geometry and distribution of the unit within the Fort Worth Basin (Thompson, 1988). Only a few authors have published their studies of this interval (Van-Wagoner, 1975; Gun, 1979; and Pranter, 1989) who describe it as turbidites / submarine fan complex deposits.

Data Available

For the development of this project a data set was provided from an independent oil and gas company who wished to remain anonymous. This data set is composed of the following elements:

- A post-stack, migrated 3D seismic volume with an area of approximately 35 square miles located in north-central Texas.
- Twenty edited well logs with DT (P and S), GR and some dynamic elastic parameters (MU, PR, K).

Objectives

The main objective of this thesis is to determine the areal distribution of the sand bodies within the Lower Strawn Formation. Due to the lack of seismic reslution in the target interval, this challenge was addressed by appliying machine learning techniques to generate seismic facies classifications wit the aim to get better visualization of the main structural elements.

Workflow

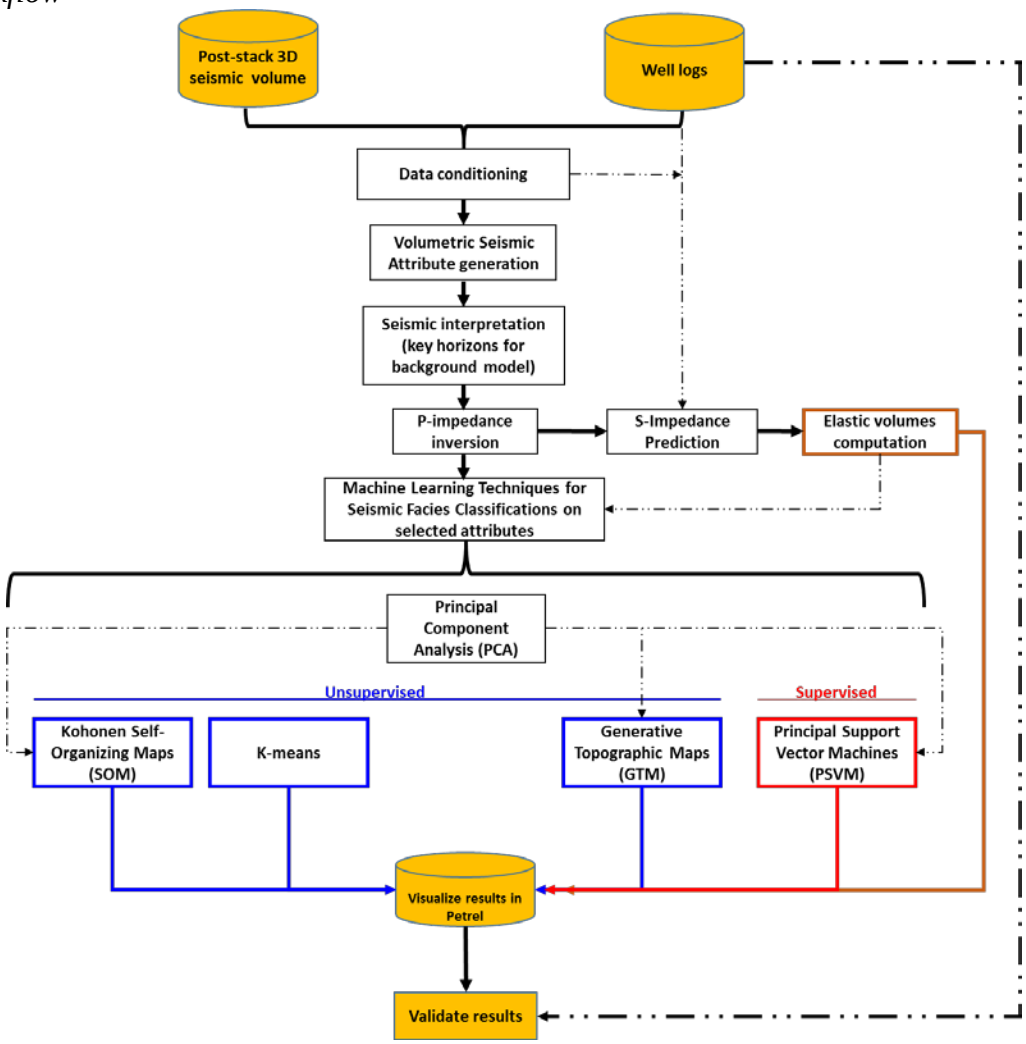

Figure 1. Workflow used for developing the thesis.

Chapter 2: Geologic Setting

The 3D seismic survey is located in the North-Central part of the Fort Worth Basin, that is a north-south-elongated Paleozoic foreland basin that covers roughly 38,000 square kilometers (Montgomery et al, 2005). This basin was formed during the late Paleozoic Ouachita orogeny, a major event of thrust-fold deformation resulting from the collision of ancestral North American and Afro-South American plates (Walper, 1982; Thompson, 1988). It is bounded on the east by the Ouachita Thrust Belt, on the north by the Red River and Muenster Arches, on the south by the Llano Uplift, and on the west by the Concho Platform – Bend Arch (Figure 2).

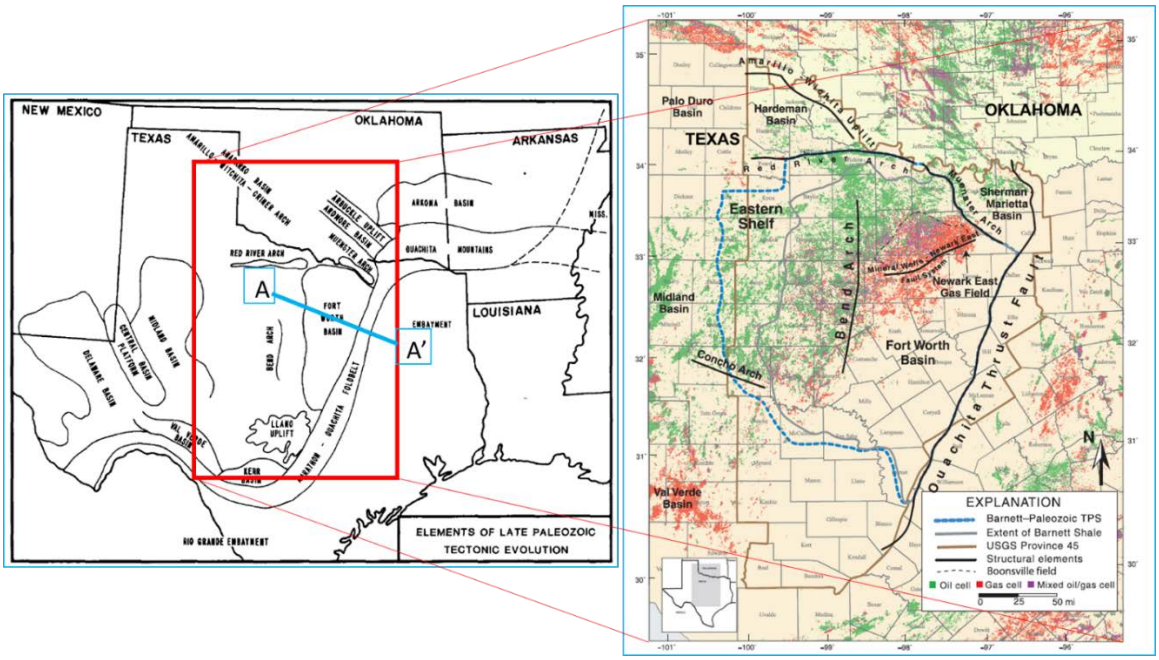

Figure 2. Elements of Late Paleozoic Tectonic Evolution (Walper, 1982) and Bend Arch–Fort Worth Basin province with major structural features. (Pollastro et al, 2007)

According to Montgomery (2005), the Fort Worth basin is a wedge-shaped, northward-deepening depression. Its axis trends roughly parallel to the Ouachita structural front, which bounds the basin to the east (Figures 2, 3). A northern margin is formed by fault-

bounded basement uplifts of the Red River and Muenster Arches and have been interpreted to be part of the northwest-striking Amarillo–Wichita uplift trend, created when basement faults associated with the Oklahoma aulacogen were reactivated during Ouachita compression (Walper, 1977; 1982).

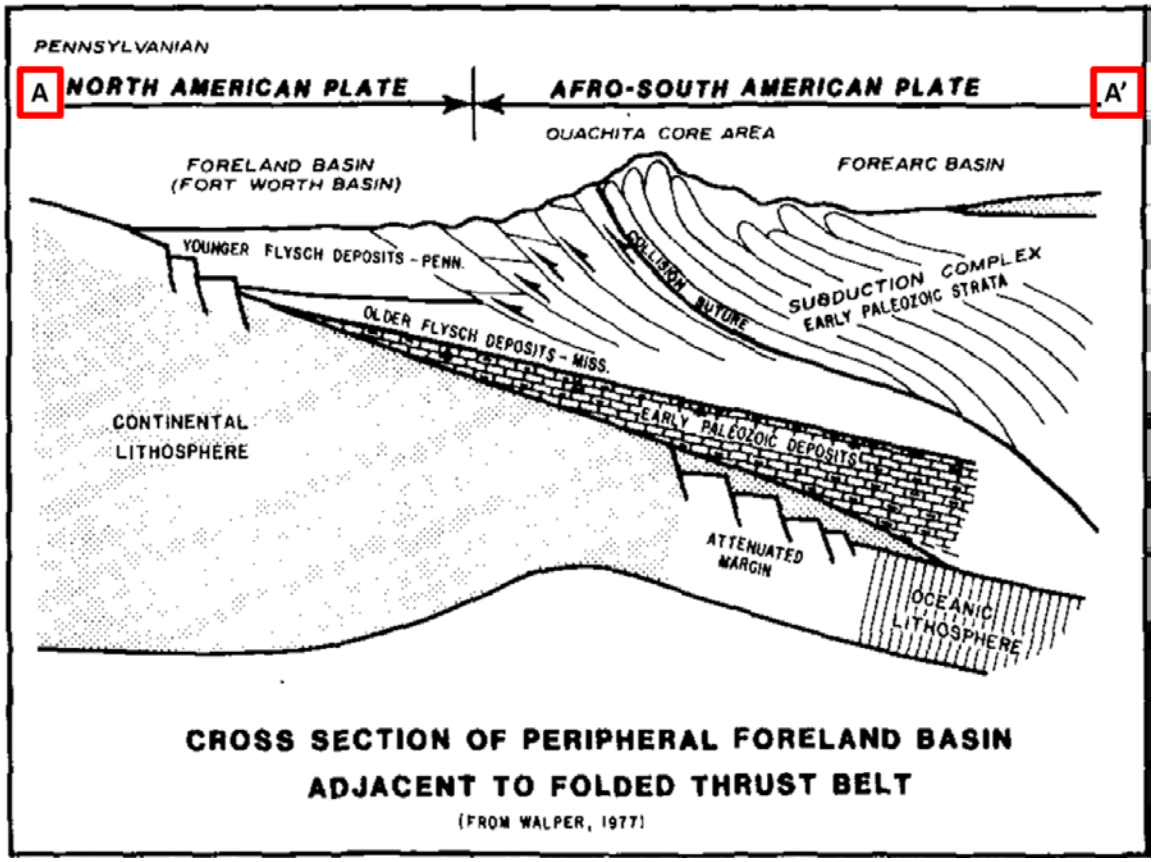

Figure 3. Tectonic Cross Section during Late Paleozoic Tectonic Evolution (Walper, 1977)

An important structural feature in this area is the Mineral Wells fault (see Figures 2, 4 and 5), a prominent northeast- southwest structure more than 65 mi (104 km) in length that bisects the Newark East field in north Texas. Apparently, the origin of the Mineral Wells structure is not well understood because it does not appear directly related to either the Muenster–Red River Arch or the Ouachita front (Montgomery, 2005). Proprietary seismic

data suggests that the Mineral Wells fault is a basement feature that underwent periodic rejuvenation, particularly during the late Paleozoic. Studies have shown that the fault exerted significant control on the deposition of upper Atokan sediments (Thompson, 1982) and that it also directly influenced depositional patterns and thermal history of the Mississippian units, as well as hydrocarbon migration in the northern Fort Worth Basin (Pollastro et al, 2003).

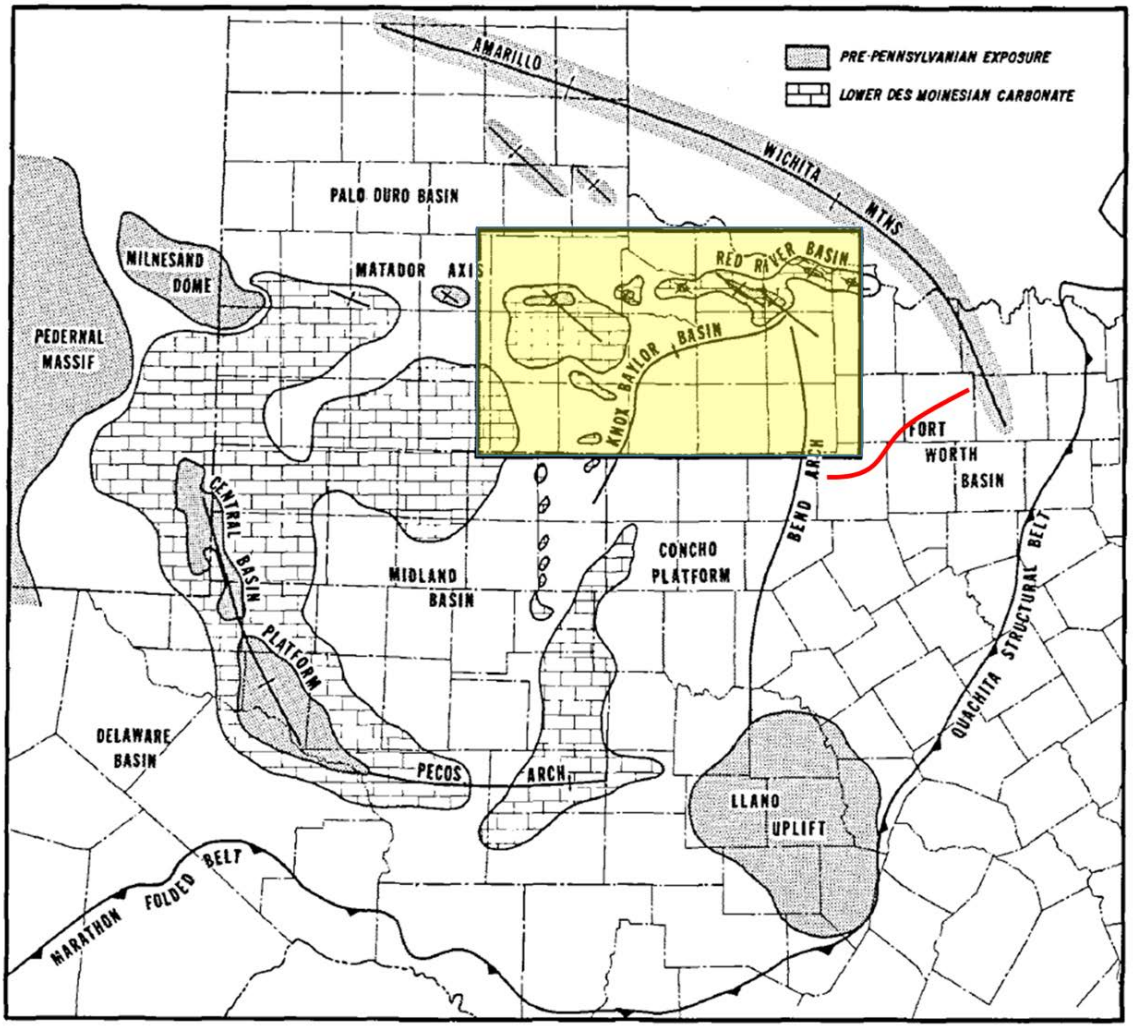

Figure 4. Regional tectonic setting of Knox-Baylor basin (yellow) in Late Desmoinesian time. The Minerals Wells fault system is in red. (modified from Gun, 1979).

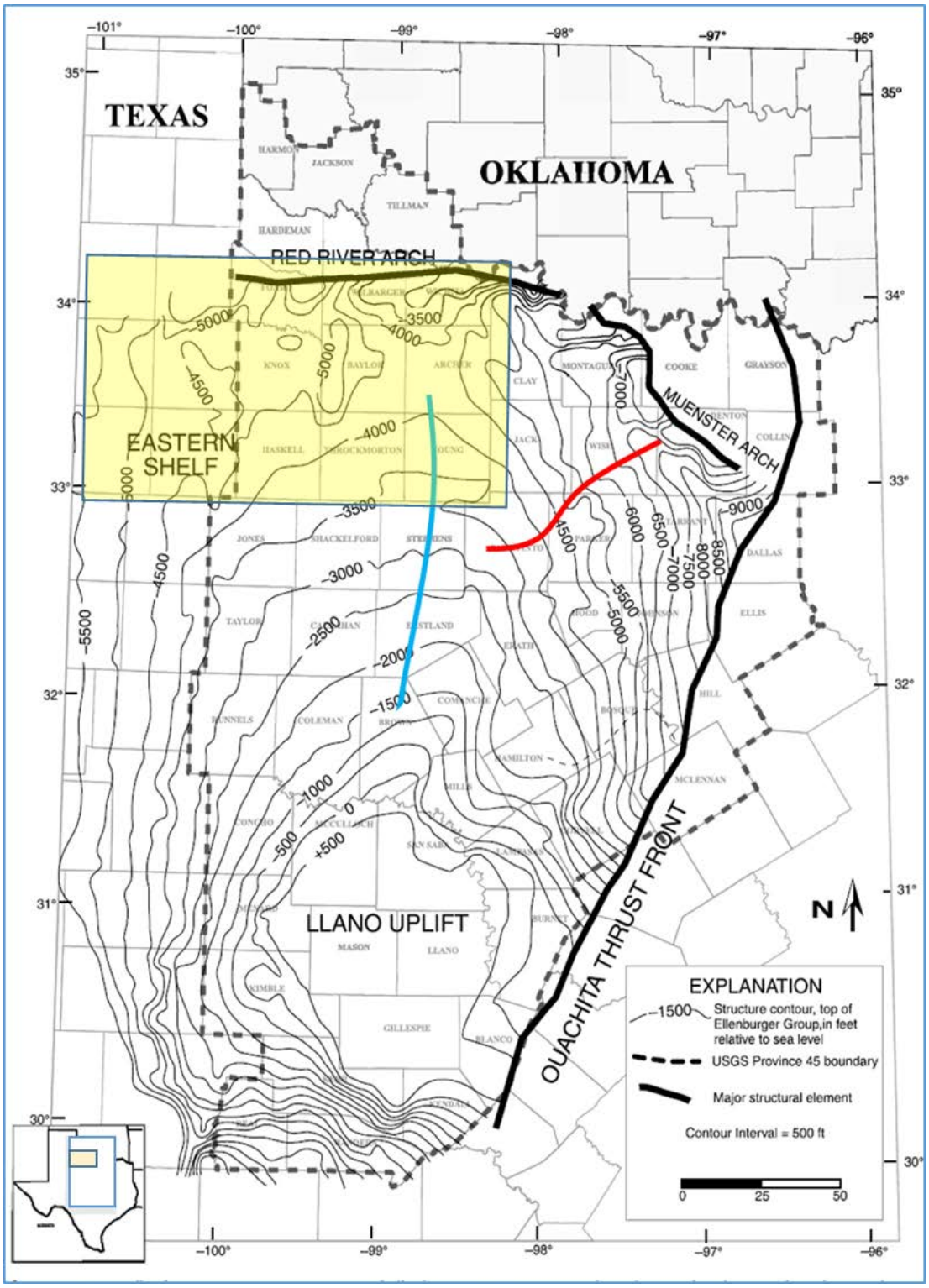

Figure 5. Generalized structure contour map, top of Ellenburger Group, Fort Worth Basin–Bend Arch area of north-central Texas. The Minerals Wells fault system is in red. Bend-Arch axis is in blue. Knox-Baylor basin is in yellow (Modified from Pollastro, 2007).

Stratigraphy

Sedimentary rocks in the Bend Arch-Fort Worth Basin reach a maximum thickness of about 12,000 ft adjacent to the North-East area of the basin (Muenster Arch) and consist of Ordovician-Mississippian shales and carbonates, Pennsylvanian clastics and carbonates, and in the eastern part of the basin, a thin remnant of Cretaceous rocks (Pollastro et al, 2007). This sedimentary cover is underlain by Precambrian granite and diorite basement (Flawn et al., 1961; Henry, 1982; Lahti and Huber, 1982; Thompson, 1988). Generalized stratigraphy of the Fort Worth basin is shown in Figure 6.

Montgomery (2005) states the total Paleozoic section can be roughly divided into three intervals, reflective of tectonic history: (1) Cambrian–Upper Ordovician platform strata (Riley–Wilberns, Ellenburger, Viola, Simpson), deposited on a passive continental margin; (2) middle– upper Mississippian strata (Chappel Formation, Barnett Shale, and lower Marble Falls Formation), deposited during the early phases of subsidence related to tectonism along the Oklahoma aulacogen; and (3) Pennsylvanian strata (upper Marble Falls Formation, Atoka, etc.), representing the main phase of subsidence and basin infilling related to the advancing Ouachita structural front. A regional unconformity is covering the lower Paleozoic section. Silurian and Devonian strata are absent in the basin (Flippin, 1982). The upper section of Mississippian and lower part of Pennsylvanian deposits appear conformable but may include disconformities in some areas (e.g., proximal to the Muenster Arch) (Flippin, 1982; Henry, 1982).

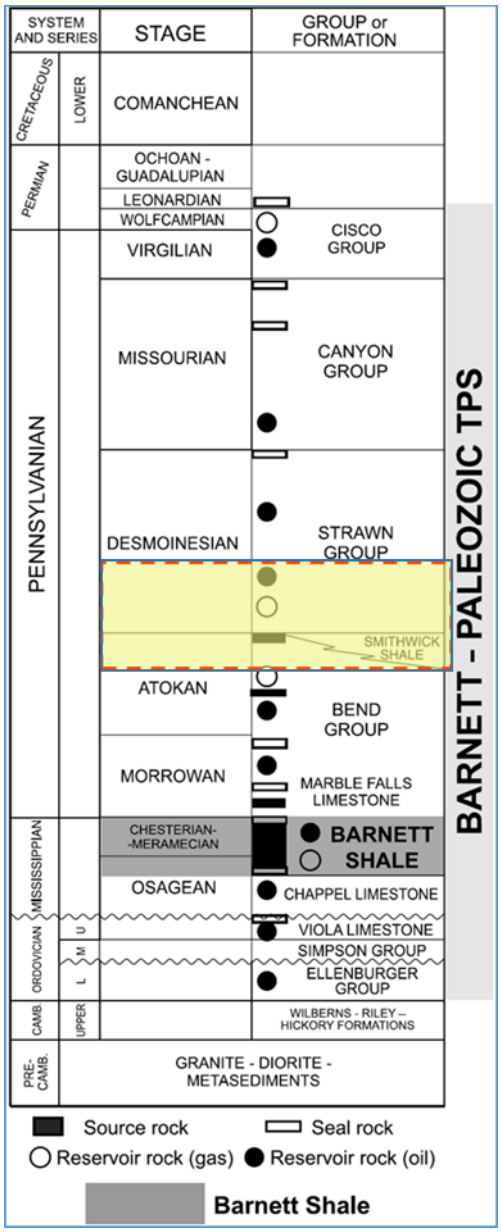

Figure 6. Generalized subsurface stratigraphic section of the Bend Arch–Fort Worth Basin. The target interval is in yellow (Modified from Pollastro, 2007).

Sedimentary rocks are underlain by Precambrian igneous basement (Figure 5). From the Cambrian to the Mississippian, the current Fort Worth Basin was part of a stable cratonic shelf, with deposition dominated by carbonates (Turner, 1957; Burgess, 1976). According to Pollastro (2007), “Ellenburger Group carbonate rocks represent a broad epeiric

carbonate platform that covered virtually all of Texas during the Early Ordovician". A pronounced drop in sea level at the end of Ellenburger deposition caused a prolonged platform exposure generating extensive karst features in the upper part of the carbonate sequence (Sloss, 1976; Kerans, 1988). Moreover, posterior erosional events should have removed any Silurian and Devonian rocks present in that area (Henry, 1982). The Barnett Shale was deposited over the resulting unconformity over most of the Fort Worth Basin.

According to Pollastro et al (2007), "Mississippian rocks consist of alternating shallow-marine limestones and black, organic-rich shales; however, the Mississippian section is not well defined because of lack of sufficient diagnostic fossils". The Pennsylvanian (Morrowan) Marble Falls Limestone overlies the Barnett Shale (Figures 4). The lower shale succession of the lower Marble Falls is used as a marker unit and sometimes is erroneously referred on subsurface well logs as the Barnett Shale (Pollastro et al 2007). Flippin (1982), and Henry (1982) state the "uppermost Mississippian and lowermost Pennsylvanian rocks appear conformable but may include disconformities in some areas (e.g., proximal to the Muenster Arch)".

According to Cleaves (1982) and Thompson (1988), "Pennsylvanian rocks deposited over the Marble Falls consist of clastic and mixed carbonate deposits that represent a range of westward-prograding fluvial-deltaic environments, and transgressive carbonate bank deposits". Terrigenous clastics were originated mainly from uplifts of the Muenster Arch and the Ouachita fold and thrust belt to the north and east and represent the main phase of subsidence and basin infilling during major advancement of the Ouachita structural front (Thompson, 1988). Sediment loading and basin formation by the westward-advancing thrust front caused a progressive westward shift of depocenters (Thompson, 1988).

Thompson (1982) concludes that “Lower Pennsylvanian deposits consist of Atokan conglomerates, sandstones, shales, and thin limestones deposited in settings ranging from marine to marginal marine to continental”. By studying the depositional patterns in Lower Pennsylvanian (Atokan) rocks, Lovick et al (1982) indicated that “the Muenster Arch was an active sediment source prior to major uplift.” Thick-skin tectonics along the Muenster Arch probably involved the rejuvenation of older, deeper basement faults, associated in part with the Oklahoma aulacogen (Flawn et al., 1961; Walper, 1977, 1982).

Permian rocks occur in some areas of the Fort Worth Basin, but no Triassic or Jurassic rocks have been identified, probably because of the pre-Cretaceous erosional events that took away previous sediments. According to Walper (1982), “Cretaceous rocks of the Comanche series overlie the tilted and eroded Paleozoic sequence along the eastern part of the basin.”

Local Geology

Brown, et al (1973), presented an extensive description of the Pennsylvanian depositional systems in North-central Texas; however, his work does not get into the details of the sediments deposited below the Upper Strawn Formation (Target of this thesis). Notwithstanding, he states that the sediments of the Lower Strawn Formation can be inferred from subsurface data as slope deposits which constitute the main fill of the Knox-Baylor basin (see Appendix Figure A8). These sediments were deposited by turbidity currents, mass gravity movement, grain flow, and possible traction flow (Brown, et al, 1973). Therefore, and stated early, only three authors have some published information about the Lower Strawn Formation (Van-Wagoner, 1975; Gun, 1979; and Pranter, 1989)

who describe it as turbidites / submarine fan complex deposits. From these authors, Gun, (1979) is the only one who studied the Lower Strawn in the north-central area of the Fort Worth Basin (Knox-Baylor Basin) in which the data set available for this thesis is enclosed (Figure 4). From his work, Gun (1979) stated that the Knox-Baylor trough was the result of a series of tectonic disruptions that moved the Desmoinesian depositional center of the Fort Worth basin towards the west, in which sediments coming from the north and north-east were transported towards the midland basin. Figure 7 shows a structure map on top of the Lower Desmoinesian units (Gun, 1979) in which it is possible to state more than one hypothetical direction of source of sediments, not only coming from the north-east, but also from north, north-west and from the south. This map is also indicating the most probable area for the deposition of the deepwater sand deposit which would be aligned along the axis of the trough (Gun,1979).

Among the evidences that Gun (1979) presents to characterize these sandstones as deepwater deposits are core analyses from three different locations within the map shown (Figure 7) in which the composition, texture, and sedimentary structures are all uniquely similar (high quartz concentration, coarsening upward sequence, lack of bioturbation, convolute laminations), which could indicate an anoxic environment and also reworking during long-distance transport. Figure 8 shows a photograph of a specific part of one core in which the convolute laminations are indicating a highly liquid condition during deposition.

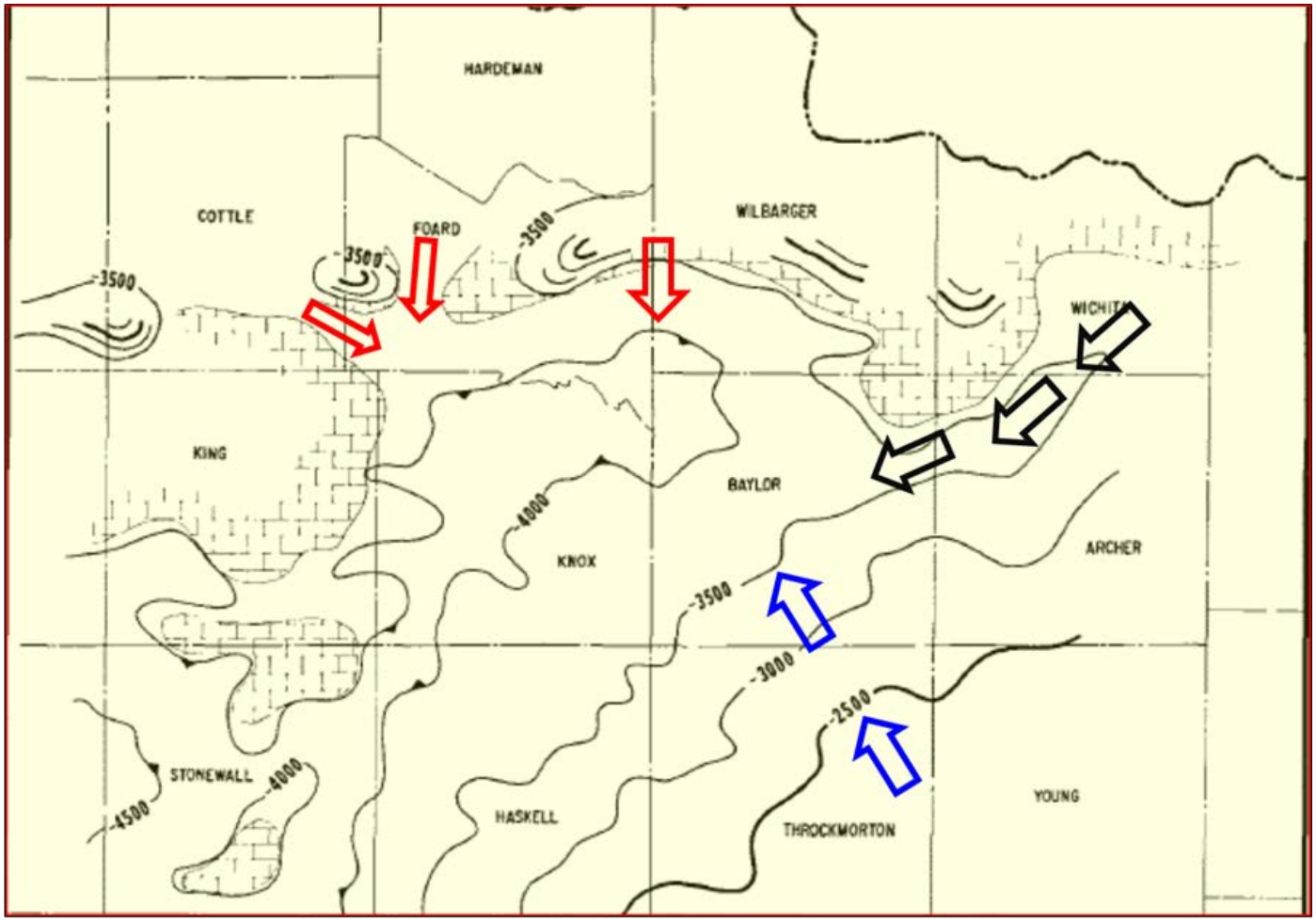

Figure 7. Structure map on top of Lower Desmoinesian units indicating the depositional topography of early Desmoinesian time (Modified from Gun, 1979). Colored arrows indicate possible directions of sediment transport.

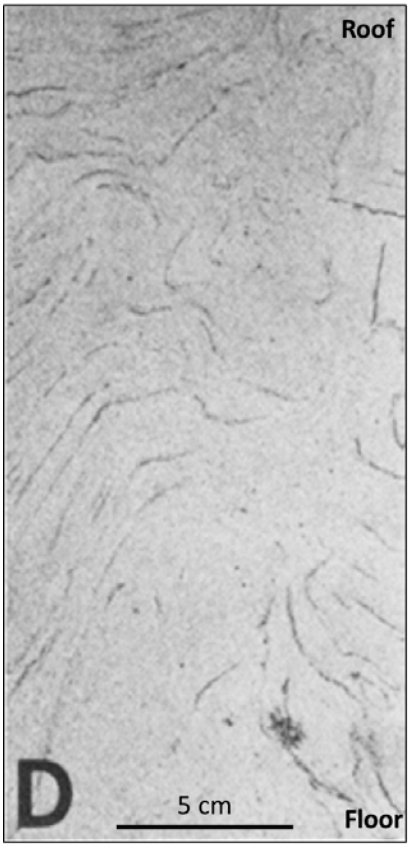

Figure 8. Sedimentary structure (deep: 5400 ft) in one of the cores that Gun (1979) used for his analysis. This is showing a sandstone with convolute bedding. (Modified from Gun, 1979).

Figure 9 shows a cross section composed of three wells located within the area of interest. The section is flattened on Top of the Smithwick Shale and from the highlighted target sandstone interval Clearly one can distinguish that each one of the wells has a different sandstone geometry that could be interpreted as deepwater deposits (X1: channel-levee complex; X2: amalgamated sandstone from channel complex; and X3: sheet sandstone with a shale break). This is just an initial interpretation from well logs that will be validated upon the seismic facies classification results.

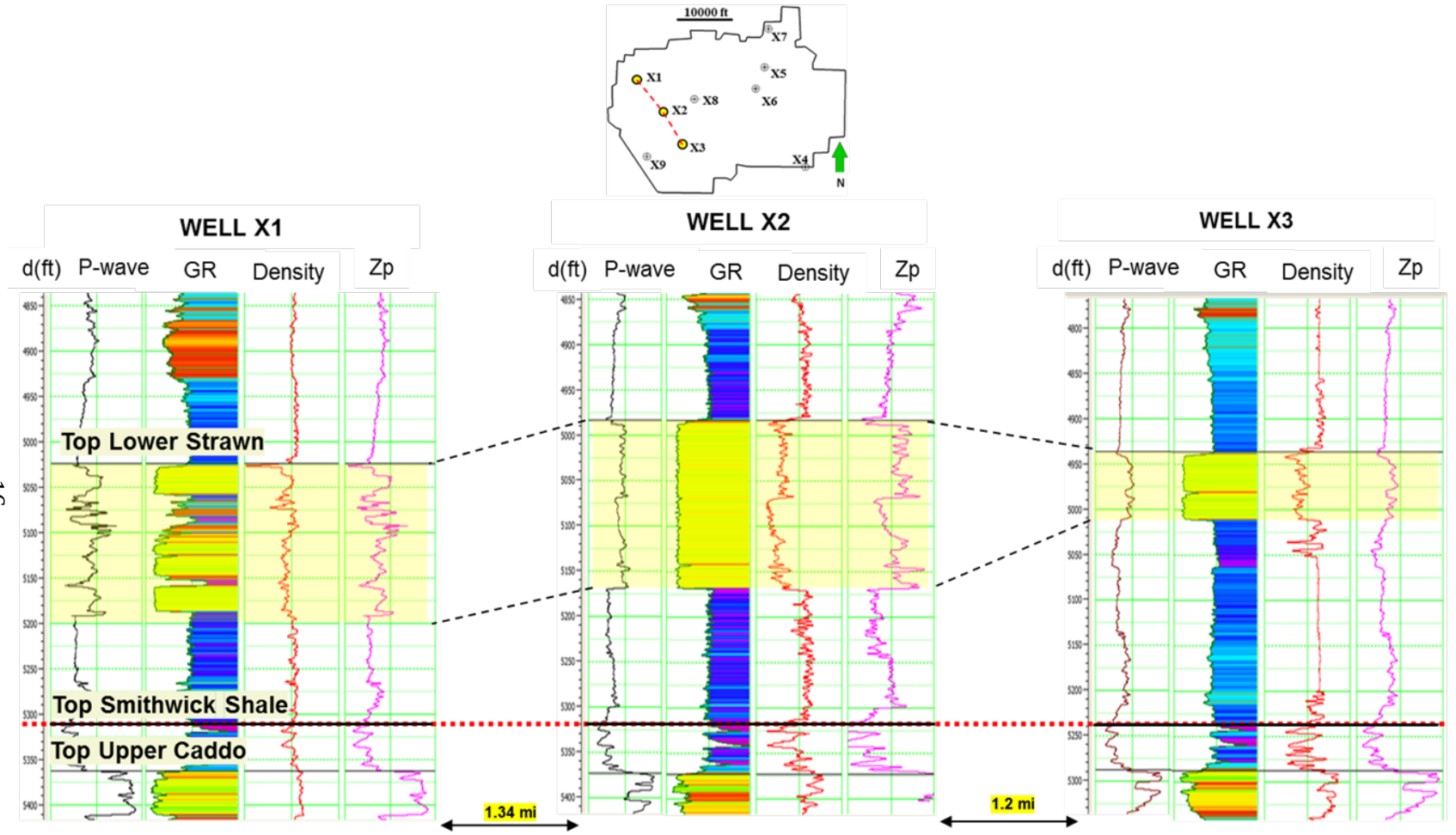

Figure 9. Cross section highlighting the sandstone target interval for this thesis. Note the blocky geometry in well X2 (+- 200 ft of thickness). X1: channel-levee complex; X2: amalgamated sandstone from channel complex; and X3: sheet sandstone with a shale break.

Chapter 3: Seismic Interpretation of Key Horizons

Data Conditioning

Information that was provided consists of a post-stack time migrated volume, full azimuth acquired by Vibroseis and processed in 2105 with a sample interval of 1 ms and a record length of 1500 ms. After loading and visualizing the data into an interpretation software package, and with the aim to improve further quantitative seismic interpretation steps as P-impedance inversion, the quality of the seismic information along the target unit zone (Lower Strawn Fm) was improved using the program sof3d (Structure-oriented Filtering of Post-Stack Data) and the program spec_cmp (Computing Spectral Components Using a Complex Matching Pursuite Algorithm) developed by the AASPI ™ group (Attribute Assisted Seismic Processing & Interpretation) in the University of Oklahoma under the guidance of Dr Kurt Marfurt. By using these techniques, it was possible to remove random noise, improve lateral continuity and enhance vertical resolution along the target unit (Chopra and Marfurt, 2006).

By computing Structure-oriented Filtering (SOF), the change of the volume was minimum, however, running Spectral Components using a Complex Matching Pursuite Algorithm (CMP) over the resulting filtered data, improved the resolution and continuity of the reflectors (Figures 10a, 10b and 10c). Having obtained this result, a set of seismic attributes was extracted from SOF and CMP volumes for further use on quantitative interpretation.

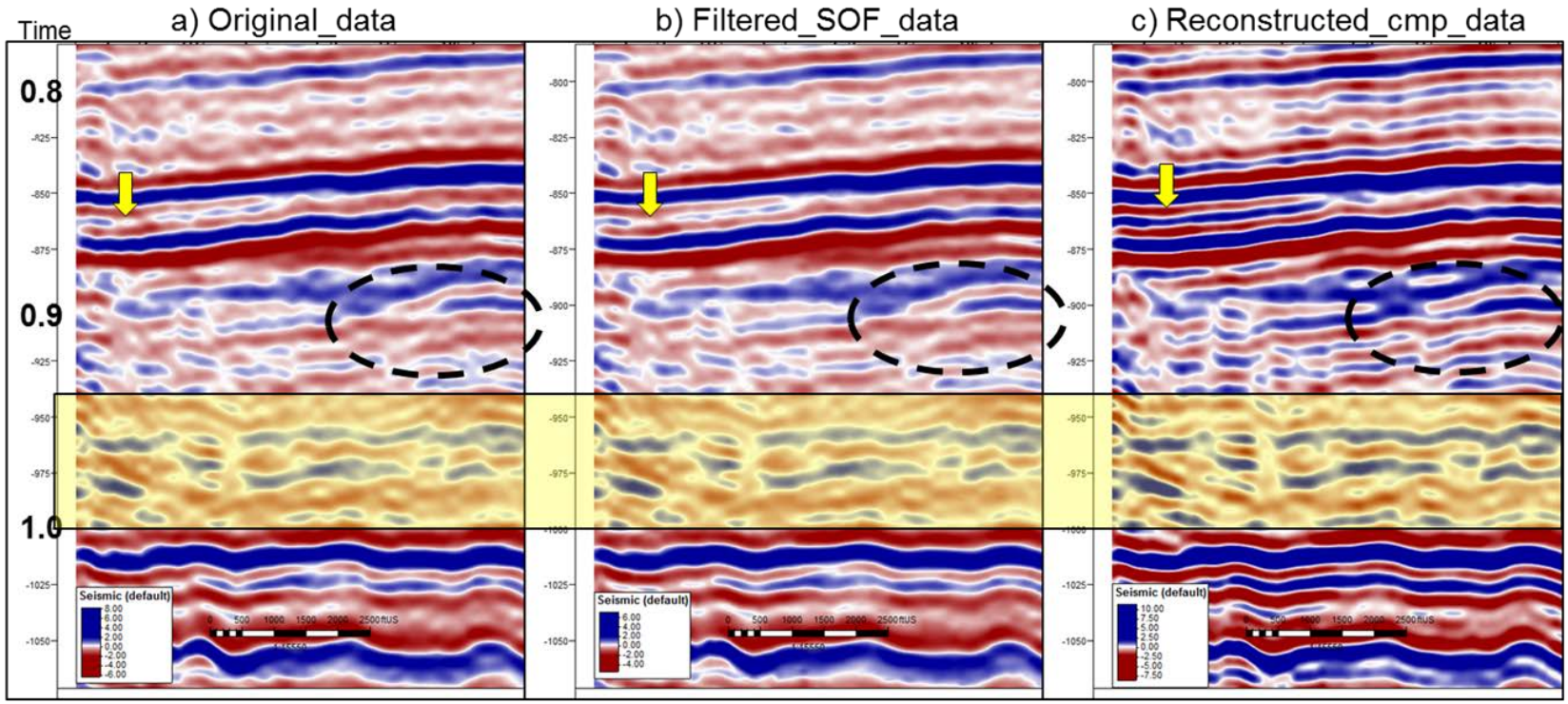

Figure 10a) original data provided. 10b) data after applying structure-oriented filter. 10c) filtered data after applying CMP spectral decomposition. Note that by using CMP it is possible to visualize and differentiate reflectors that were difficult to separate on the original data (yellow arrows and doted black ovals). Yellow square corresponds to the target interval.

After conditioning the data through structure-oriented filtering and spectral balancing instantaneous, geometric and texture attributes were computed to help to interpret the top of the main units in the area of interest (Figure 16). Also, twenty (20) well logs that fall within the 3D seismic survey containing DT (compressive) and DT-S (shear) were then carefully edited to control subsequent seismic inversion.

Well to seismic tie

A good well to seismic tie is necessary to align the well log response with the corresponding events seen in the data. All information, including well logs, formation tops and seismic volumes were loaded into a commercial software package, with the objective of finding a "match" between well logs and seismic. First, different statistical wavelets from the seismic data itself and wavelets from wells were extracted. Next, the program uses sonic velocities and density data from well logs to compute the acoustic impedance. With this information, the program computes the reflection coefficients at each point where impedance changes. After multiple iterations with different wavelets, the wavelet extracted from the interval between -700 ms to -1050 ms that contains the target unit (Strawn Fm) was selected (see Figure 9). With this synthetic seismogram, the well-tie for each one of the 22 wells with more than 70% of correlation were evaluated for further steps. Figure 11 shows the well to seismic tie for well X-2. Because the seismic wavelet changes through the overburden, different wavelets are used for different targets. In this case the target formation ranges from -800 ms to -1050 ms , which is sufficient for the purpose of the project.. Figure 12 shows the complete 3D volume and the cropped volume containing the target unit over which further processes were done.

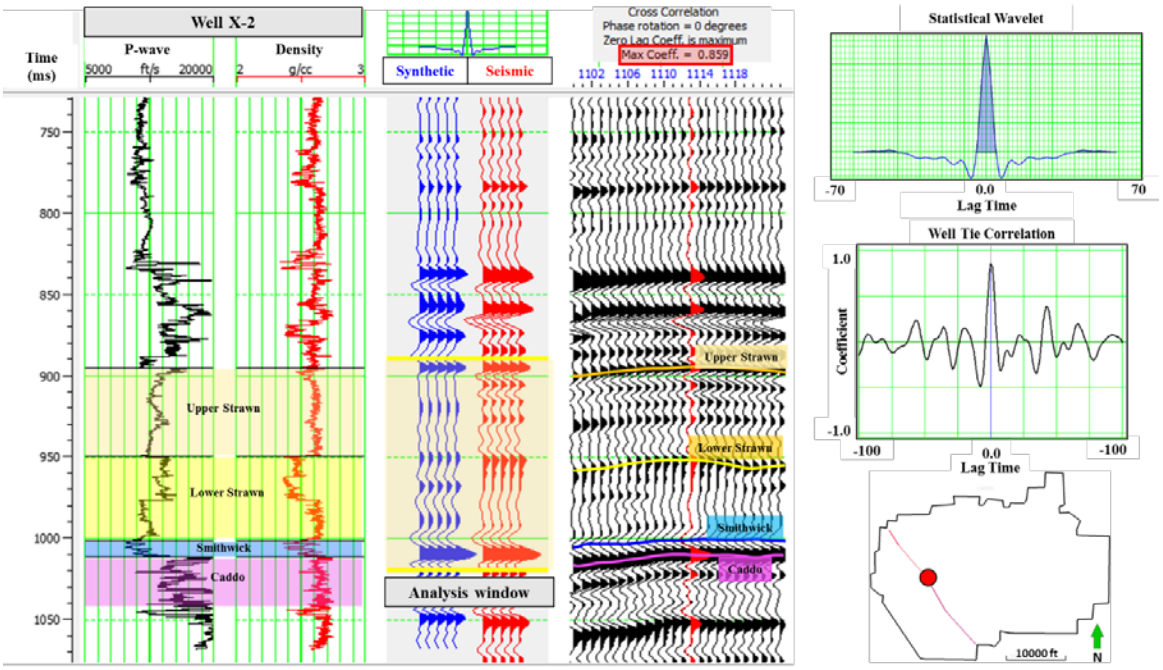

Figure 11. Well to seismic tie for well X-2

Stratigraphic Interpretation

With a good correspondence between well logs and seismic, seismic amplitude (original, filtered and reconstructed), instantaneous attributes (envelope, frequency and phase), relative acoustic impedance and cosine of the phase were used to provide a stratigraphic interpretation of 6 horizons. In some cases, where it was not possible to interpret the horizons through the whole area, attributes were displayed on “proportional slices” or “stratal slices.” These surfaces are from youngest to older as follows:

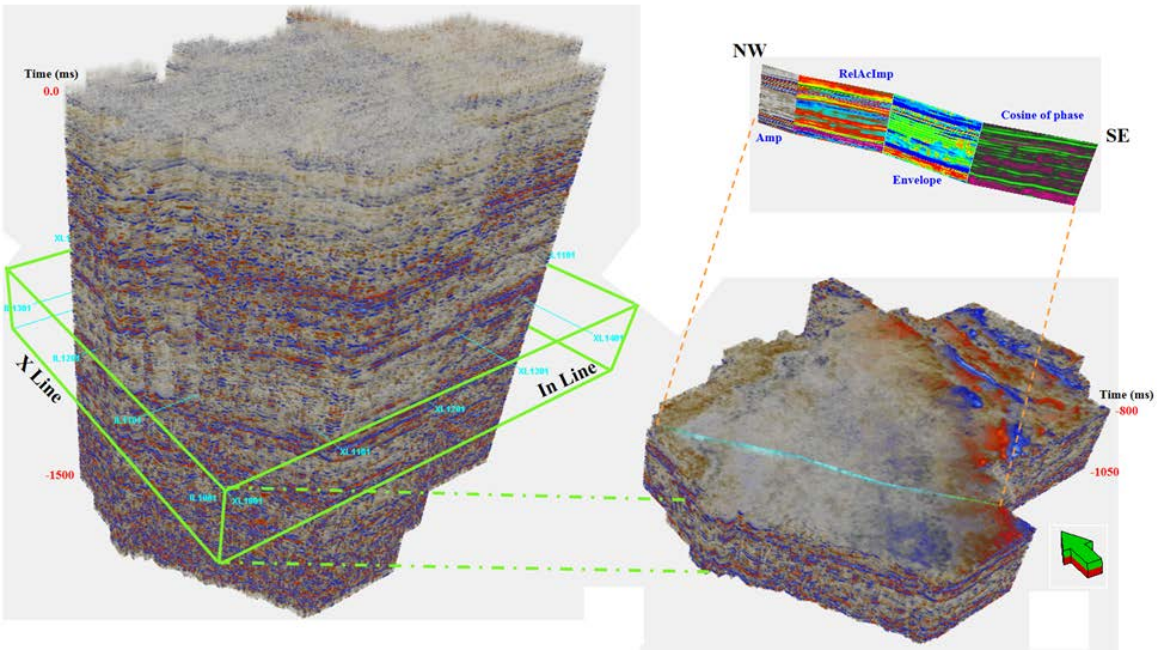

Figure 12. Original 3D seismic volume, cropped volume and NW-SE composite vertical section showing some of the attributes used for the interpretation.

1. Top Upper Strawn Fm
2. Horizon subdividing Upper Strawn Fm into two sections (US-1)
3. Top Lower Strawn Fm (proportional slice-1)
4. Continuous horizon along the target sandstone (SU) and proposed Channel Base (Sch)
5. Top Smithwick Shale
6. Top Upper Caddo

Starting the interpretation, an initial 10X10 grid of in-lines and cross-lines was used; however, due to the difficulty in following some reflectors, local 5X5 or less grids were used. Figure 13 shows the interpretation grid used for project on the upper Caddo surface. Note the structurally higher areas located on the east part of the volume are aligned with

the NW-SE structural trend. This trend is consistent with which states that the Knox-Baylor Basin was the path to transport sediments from the Muenster Arch to the Midland Basin. This NW-SE trend is clearly seen on all time-structured maps on all horizons (Figures 14 to 17). Figure 15a represents an attempt to interpret the proposed base of a Channel-like shape that in some cases corresponds with the *SU* horizon. In figure 15b, this horizon can be easily interpreted along the whole 3D seismic volume. It could be a flooding surface (Figure 15 b and c). Due to the difficulty in following the Top of the Lower Strawn Formation horizon, it was necessary to create a proportional slice (Figure 16a) that approximately mimics the behavior of the original one. Figure 16b shows the interpreted horizon that subdivides the Upper Strawn Fm into two units. Figure 17 shows a time structure map of the Upper Strawn Fm, which is the younger horizon interpreted. Figures 18 and 19 depict two vertical NW-SE and SW-NE sections showing the key interpreted horizons along the 3D seismic volume and wells through them with gamma-ray log displayed. Figure 20 shows a NW-SE amplitude section intersecting two wells and a proportional slice crossing the targeted sandstone body. Figure 21 shows a 2D view of the proportional slice where it is possible to see some channel-like features supporting the proposed interpretation of the *Sch* horizon.

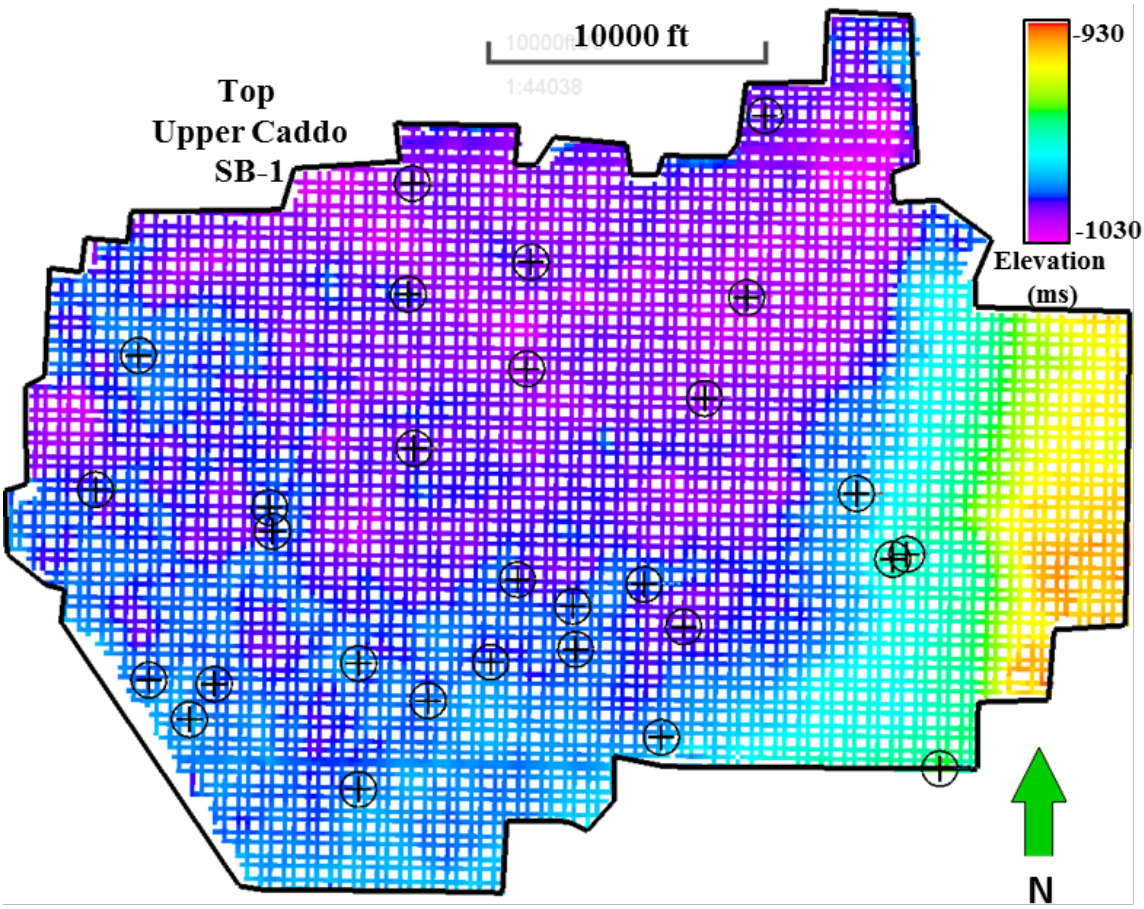

Figure 13. Interpretation grid used to follow key horizons along the volume. In black are wells used in the thesis.

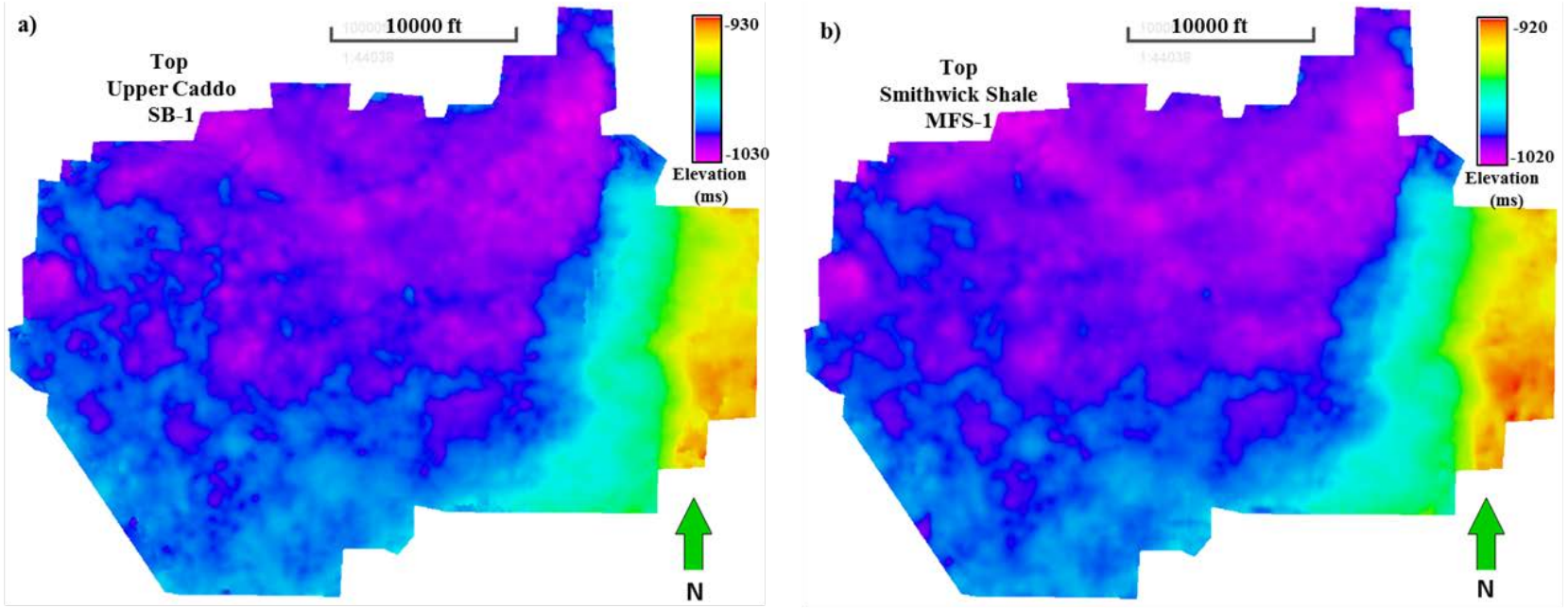

Figure 14. Time structure map of: (a) Top of Upper Caddo, and (b) Top of Smithwick Shale.

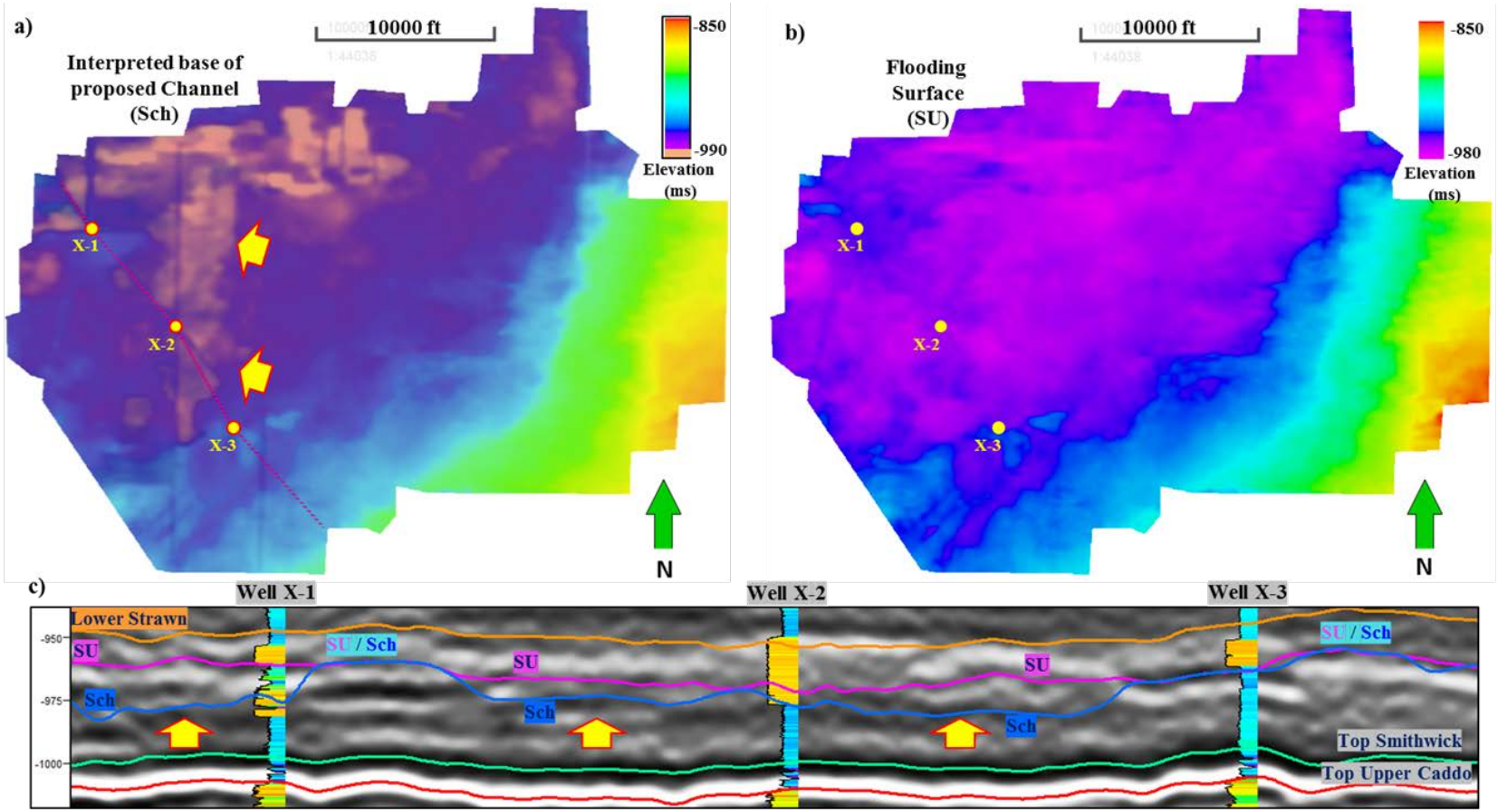

Figures 15 (a) The time structure map of Sequence boundary-2. Yellow arrows indicate channel-like shapes. (b) Time structure map of *SU* surface. c) NW-SE amplitude section showing both horizons and three wells through the section. .

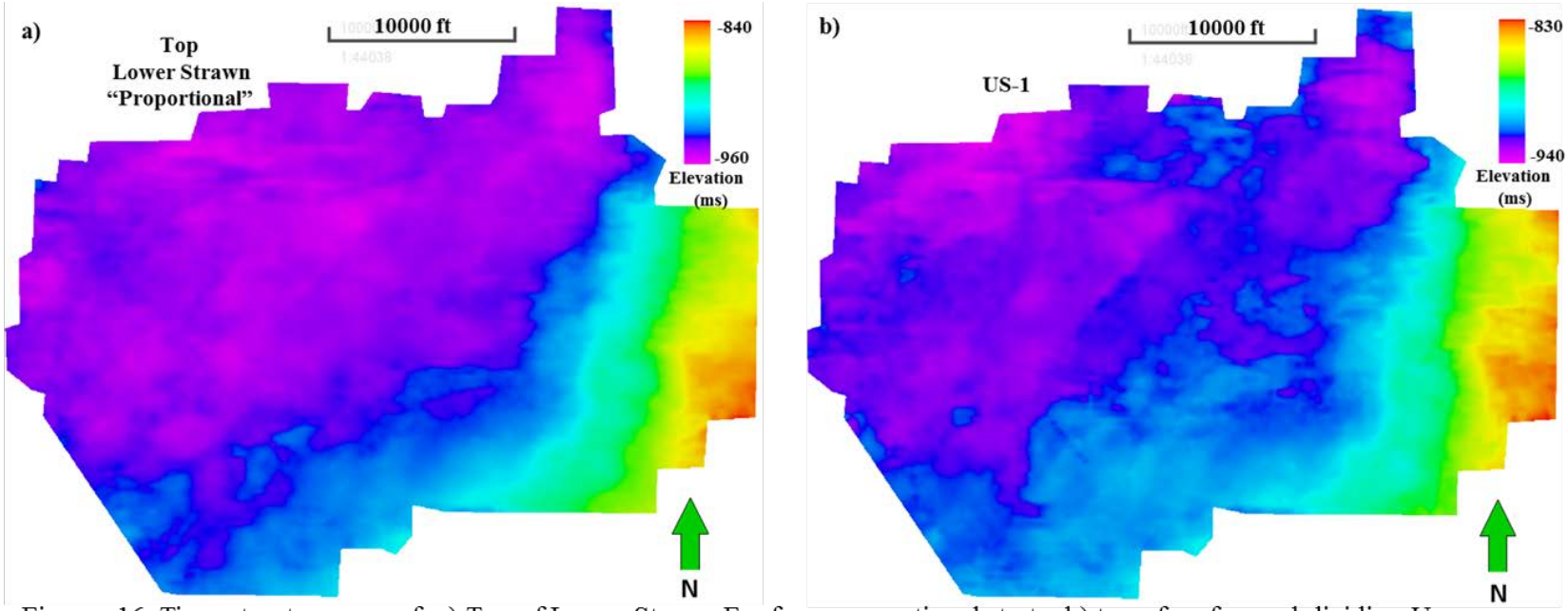

Figures 16. Time structure map of: a) Top of Lower Strawn Fm from proportional strata, b) top of surface subdividing Upper Strawn Formation into two zones (US-1).

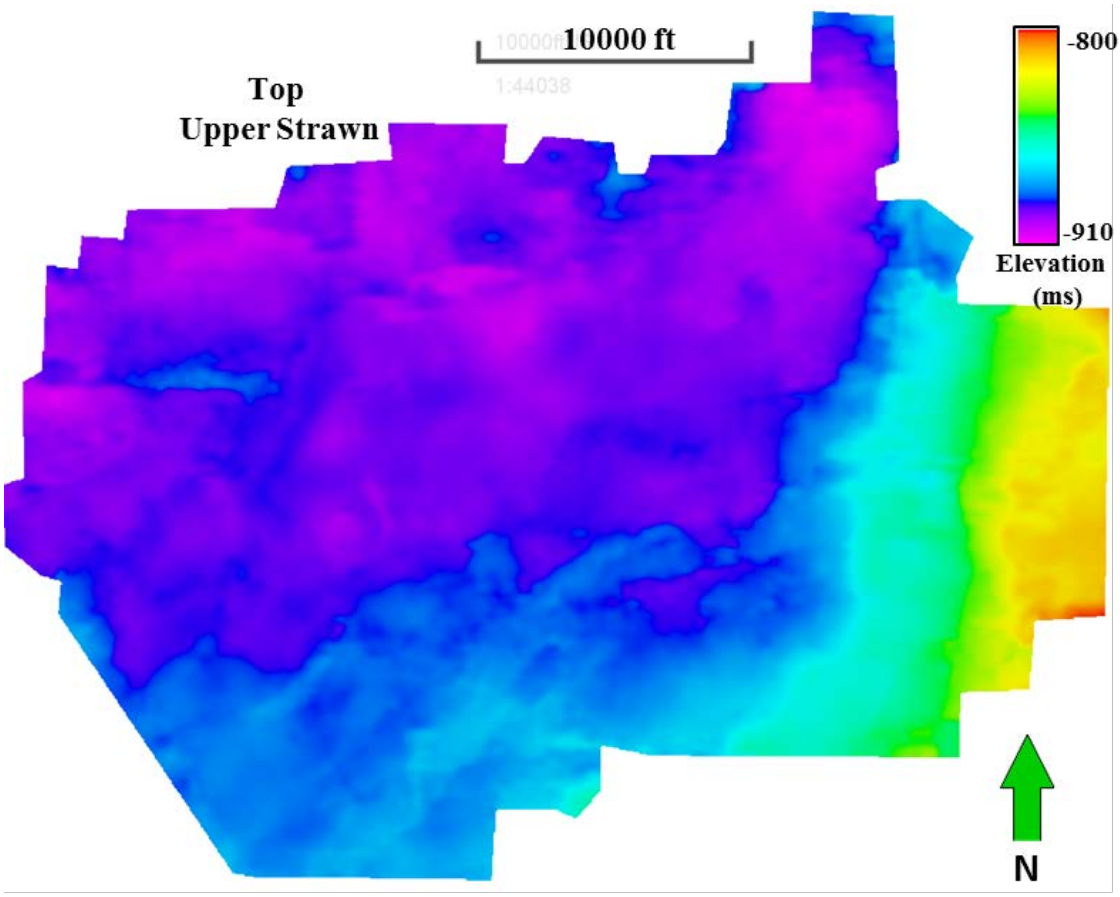

Figures 17. Time structure map of Upper Strawn Fm.

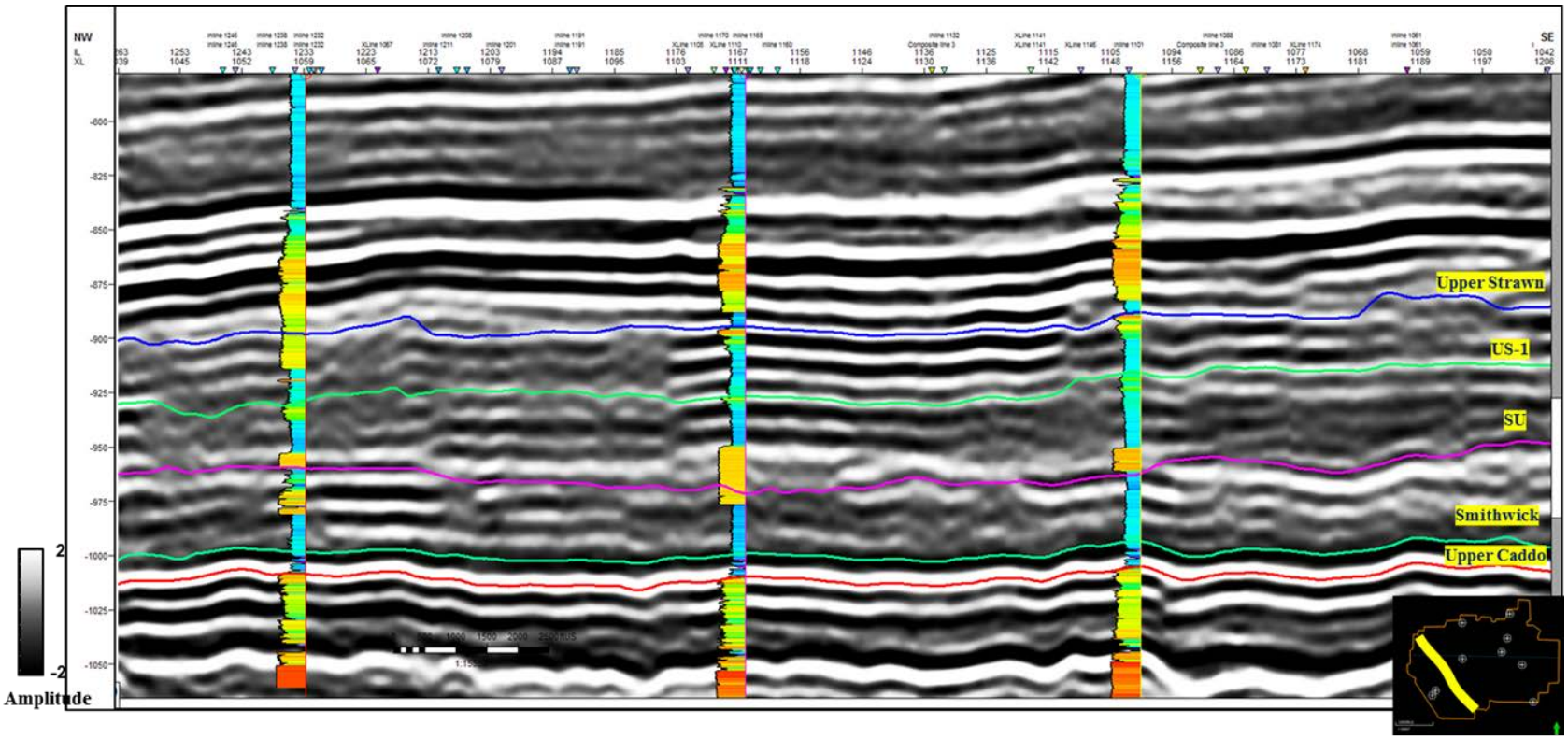

Figure 18. NW-SE vertical section showing key horizons interpreted at this stage of the project. Gamma Ray log is displayed on well locations.

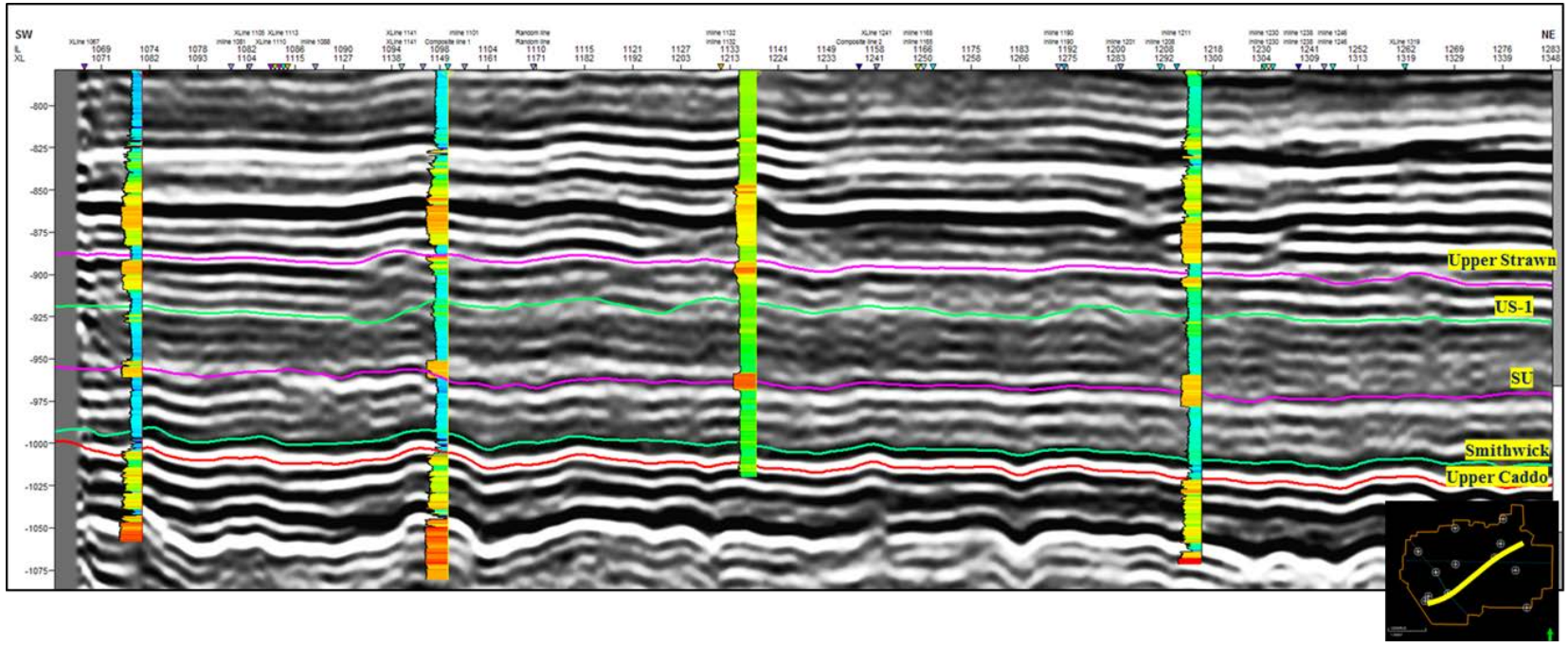

Figure 19. SW-NE vertical section showing key horizons interpreted at this stage of the project. Gamma Ray log is displayed on well locations

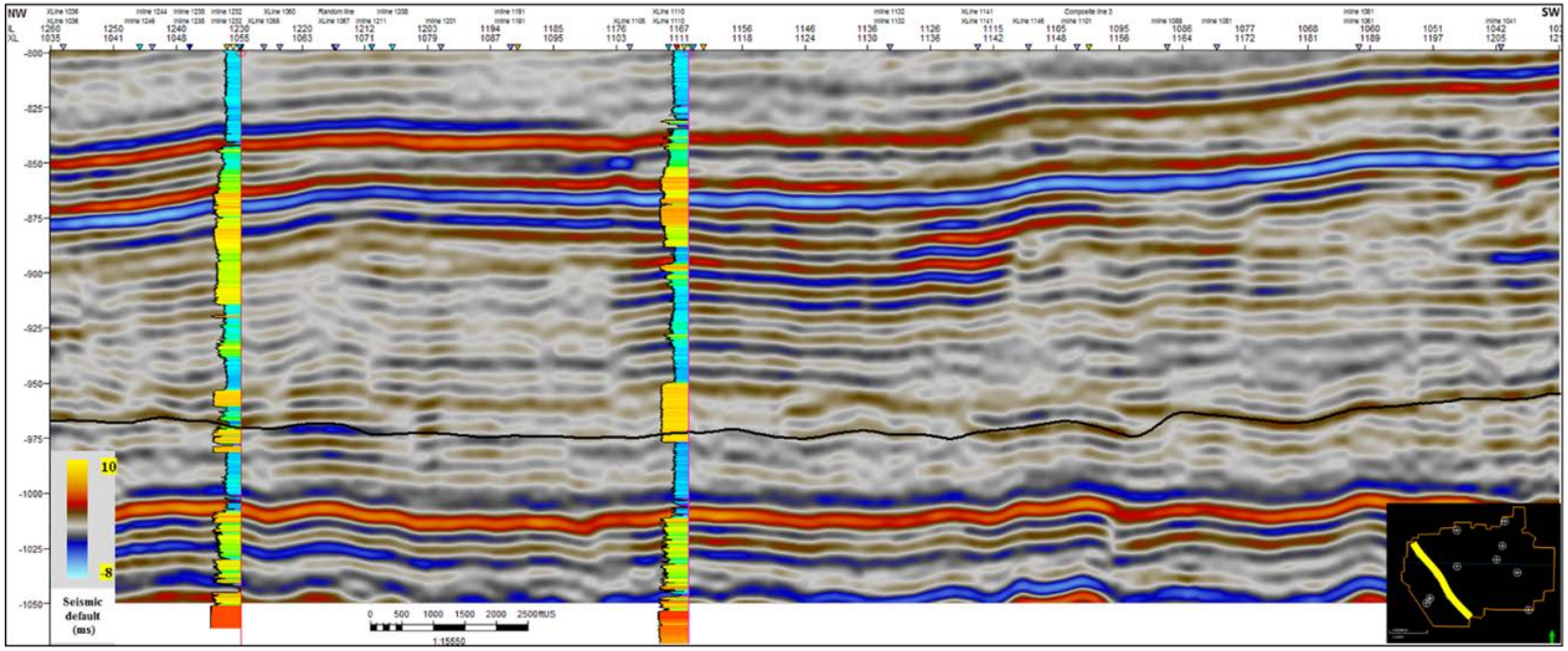

Figure 20. Amplitude seismic section (-800 ms to -1050ms) showing two wells and a proportional horizon between the Smithwick Shale and the interpreted top of the Lower Strawn Fm (black line).

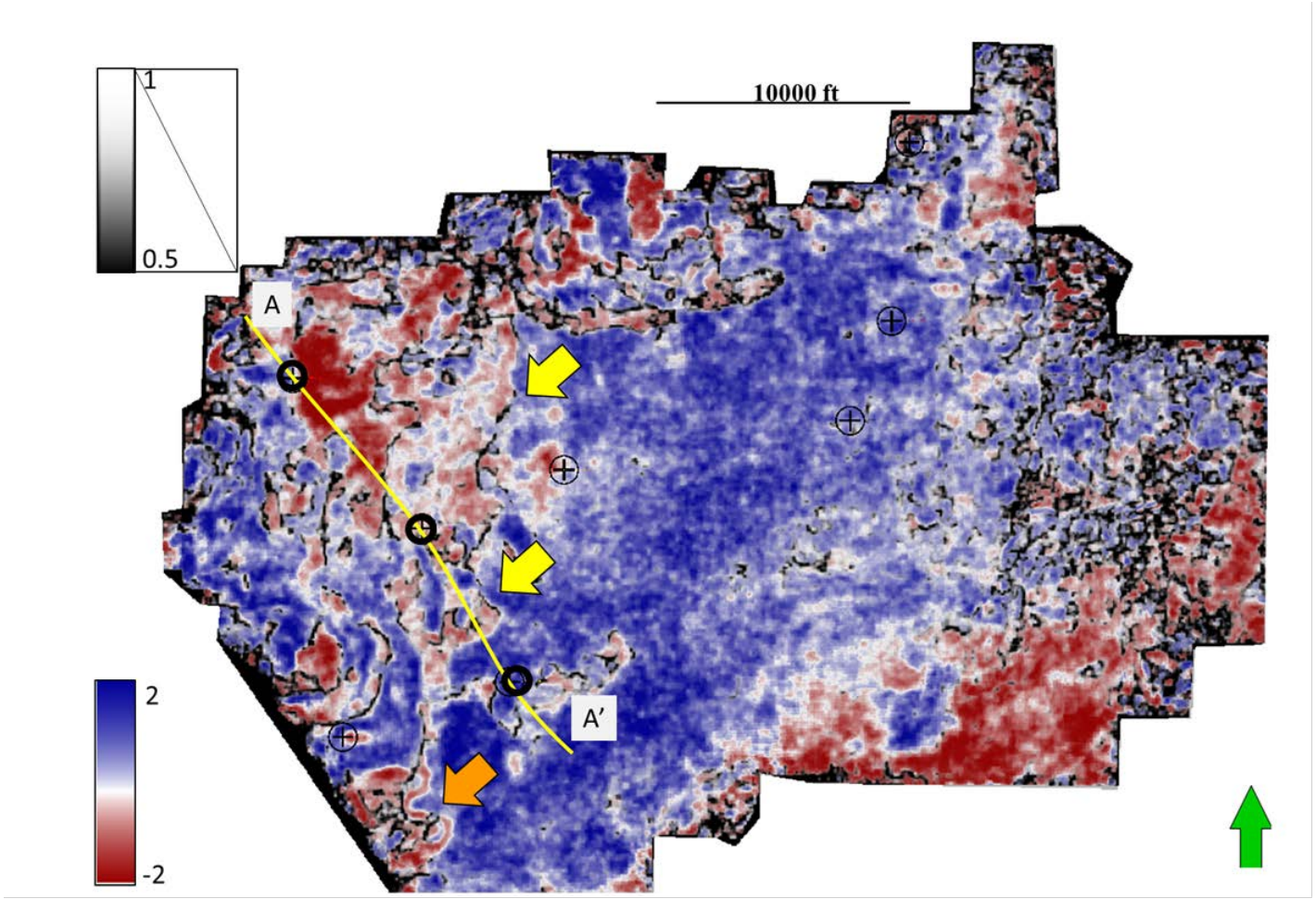

Figure 21. Amplitude co-rendered with the energy ratio similarity on proportional slice through the target sandstone unit. White arrows are pointing out some edges of channel-like features. Orange arrow indicates a tiny channel. Well X1 (north) and X2 (south) are in yellow. White line AA' is the location of the cross-section in Figure 16 and 18.

Even if it is possible to visualize some channel-like features on a proportional slice, it is not possible to clearly interpret them using common interpretation techniques. Hypothesize that by removing the seismic wavelet and unravelling the effects of overlying and underlying strata, P-impedance inversion better delineate the objective.

Chapter 4: Seismic Inversion

Thanks to enhanced computing power, seismic inversion is routinely used for reservoir characterization. The product of the density times acoustic wave velocity is the impedance, and is a function of mineralogic composition, porosity and fluid. Acoustic impedance can be extracted through the seismic inversion process that can help us to discriminate between different lithologies if there is a contrast of impedance between adjacent rocks. Usually, the seismic data acquisition workflow goes from the rock itself (lithology) to the seismic information. However, the inversion process goes from seismic information to the lithology (see Figure 22).

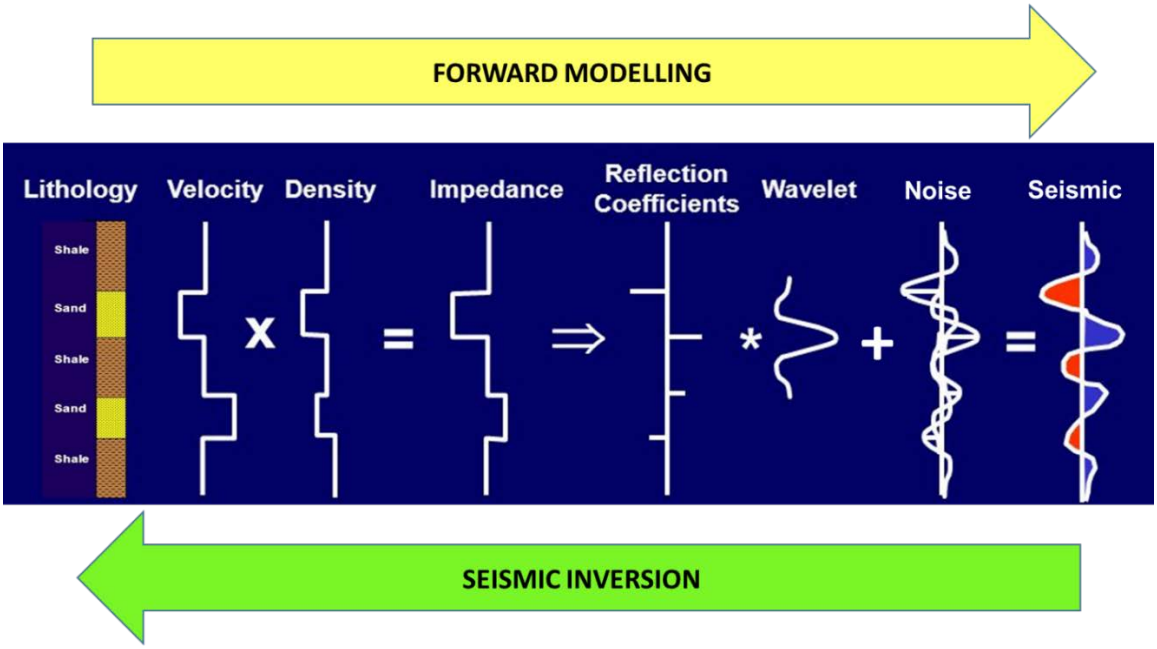

Figure 22. Sketch showing forward modeling from lithology to seismic information and seismic inversion process from seismic information to lithology. (Modified from ExxonMobil 2006).

Simultaneous inversion to obtain S-impedance and density cannot be done with post-stack data, as is used here. However, with P-waves on all wells, and S-waves in most of them, there is enough information to perform and achieve a robust P-impedance inversion and

also to predict S-impedance volume. P-impedance, S-impedance and Vp/Vs ratio were computed from logs and then cross plotted over the specific target sandstone using well log information. Figure 23 show a table with a series of cross plots generated on wells X1 and X2 (location in Figure 25) which shows it is possible to differentiate mudstones from sandstones. Also, the P-impedance (Zp) vs S-impedance (Zs) cross plot shows that the range of values of Zs is much less than Zp making the S-impedance prediction valuable.

P-Impedance Inversion

In chapter 6 a "preliminary" P-impedance inversion was performed. It was called preliminary because there were just two wells used, and because the low-frequency model was created by using the default workflow model (inverse-distance interpolation) provided by the commercial software package. In this chapter, a new methodology is introduced providing a "more robust low-frequency model for seismic impedance inversion" (Ray and Chopra 2016), that, once used in the inversion process, provides a more reliable result. To start building this low-frequency model it was necessary to do the following steps:

- Check the seismic amplitude spectrum to visualize the area with low-frequency gap (6-17 Hz). See figure 24.
- Create P-impedance logs in the 9 wells picked (see chapter 7)
- Filter these P-impedance logs to get only low frequencies between 6-17 Hz. Figure 25
- Create a low-frequency model using a single well
- Generate a relative acoustic impedance volume from colored inversion

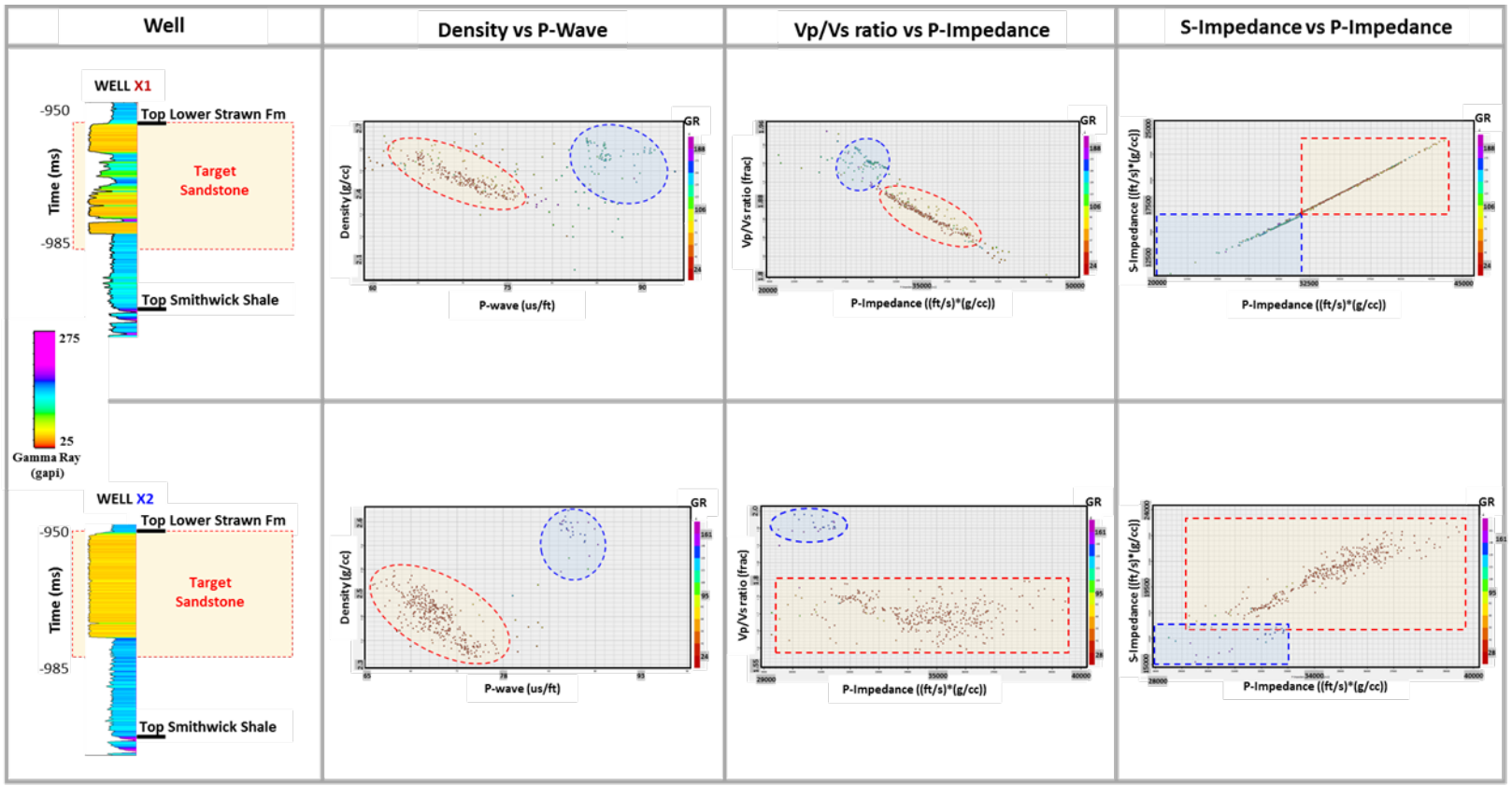

Figure 23. From left to right, wells showing Gamma-ray response over the target sandstone. Cross plots show the following relationships: Density vs. P-wave, Vp/Vs vs. P-impedance, and S-impedance vs. P-impedance constrained on this specific interval. Circles represent the possible discrimination of sandstone (light yellow) and mudstones (light blue). Vertical color bar corresponds to Gamma-ray values. These cross-plots can be seen in a bigger scale in the Appendix section.

With these inputs, plus instantaneous amplitude, instantaneous frequency volumes and interpreted seismic horizons, a low-frequency model was generated from a multi-attribute regression method by using Emerge Module in Hampson-Russell ™. Figure 24 shows a sketch of this workflow.

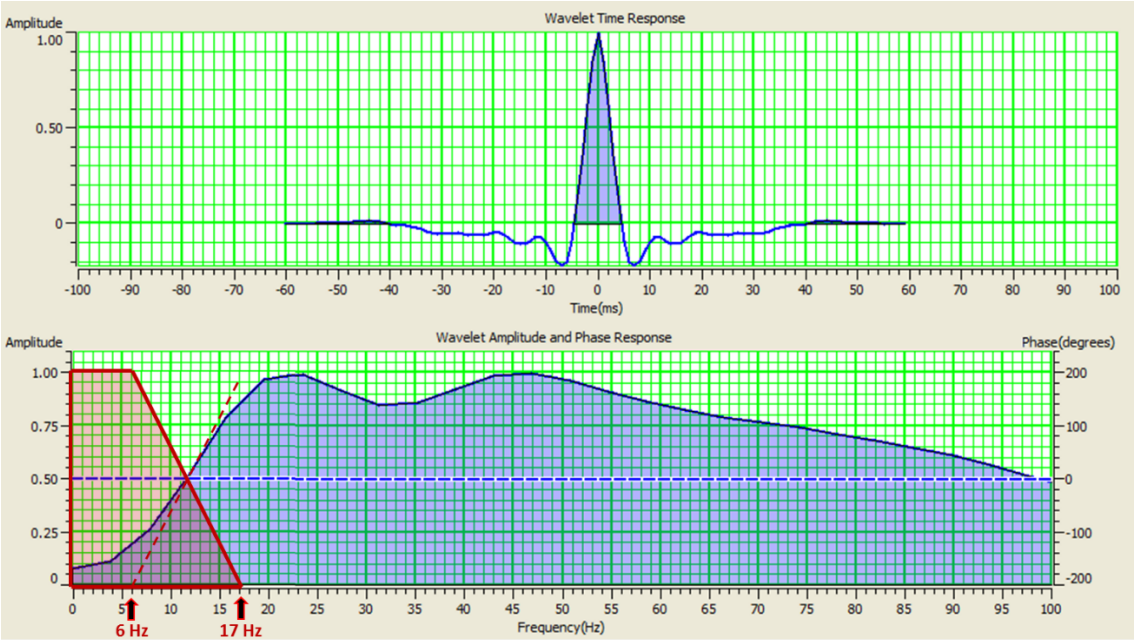

Figure 24. Wavelet and amplitude spectrum showing the low-frequency gap.

Figure 27 shows the result of these two methodologies applied on horizon *SU*. It is possible to observe in Figure 27a that low-frequency impedance model has smooth changes in values along the surface, and even at the surrounding area of the wells thus, giving a more geologically realistic model. Figure 27b represent a low-frequency model generated from an inverse-distance interpolation method, which shows anomalies or clusters around most of the wells, which will surely result in problems if it is applied to the impedance inversion process (Ray and Chopra, 2016).

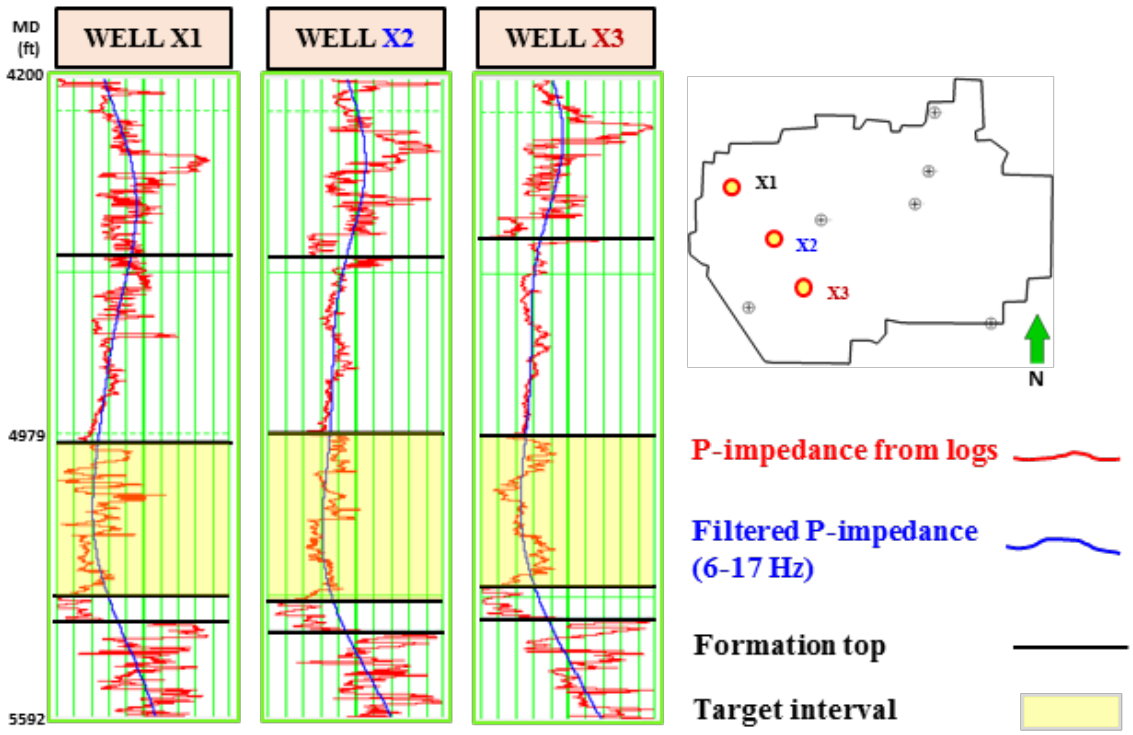

Figure 25. P-impedance (red) and filtered P-impedance from logs (blue) for wells X1, X2 and X3.

A wavelet for preliminary inversion has been extracted (Figures 9 / 22), and the best 9 wells have been chosen from the well to seismic tie process (correlation >70%). The P-impedance inversion analysis is performed on a window from -800 ms to -1050 ms. Figure 28 shows the inversion analysis results on wells X1, X2 and X3 with 99.44%, 99.71% and 99.72% of correlation respectively. The rest of the wells also have similar correlations percentages.

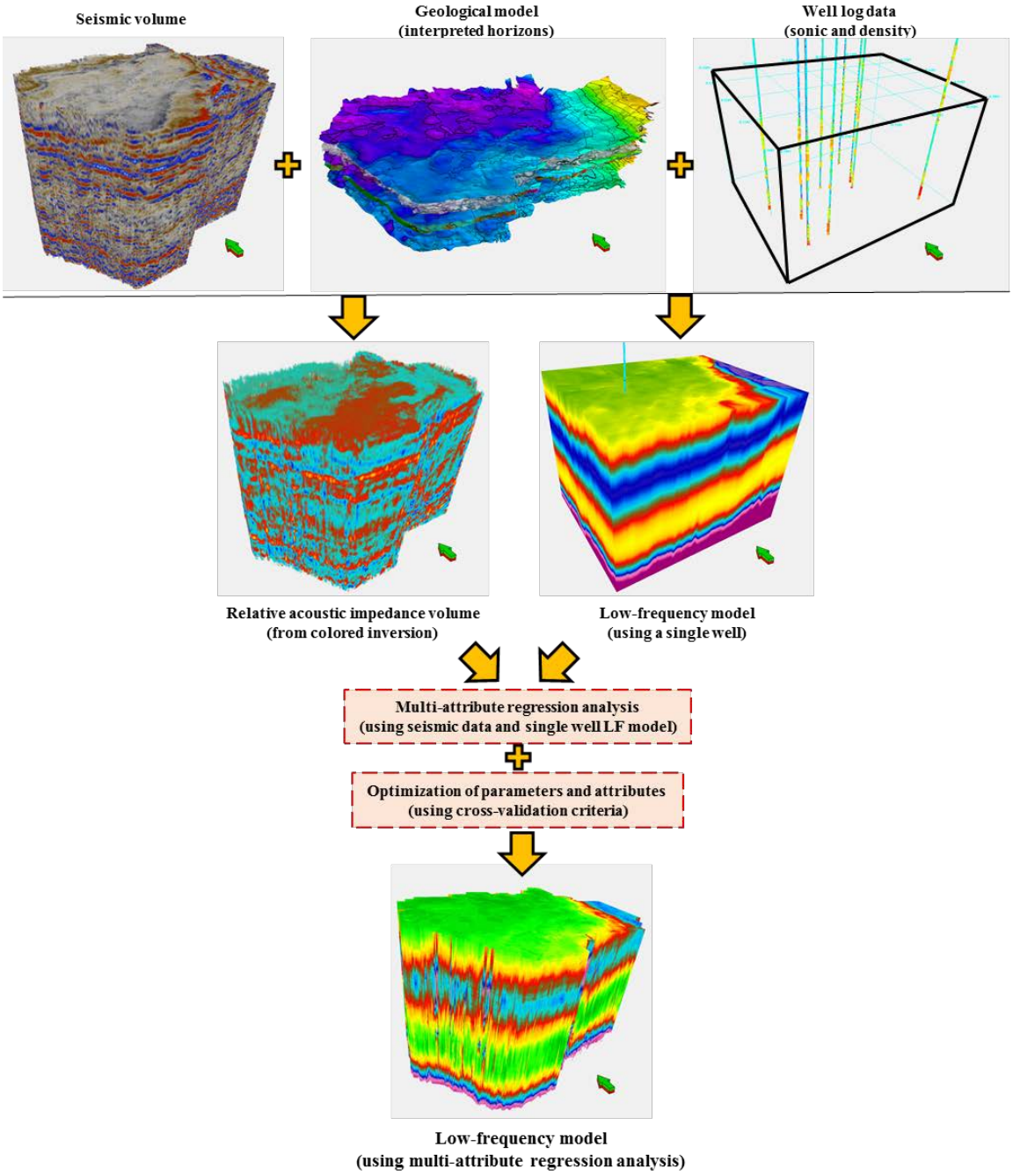

Figure 26. Workflow for generating low-frequency model using multi-attribute regression. (Modified from Ray and Chopra 2016)

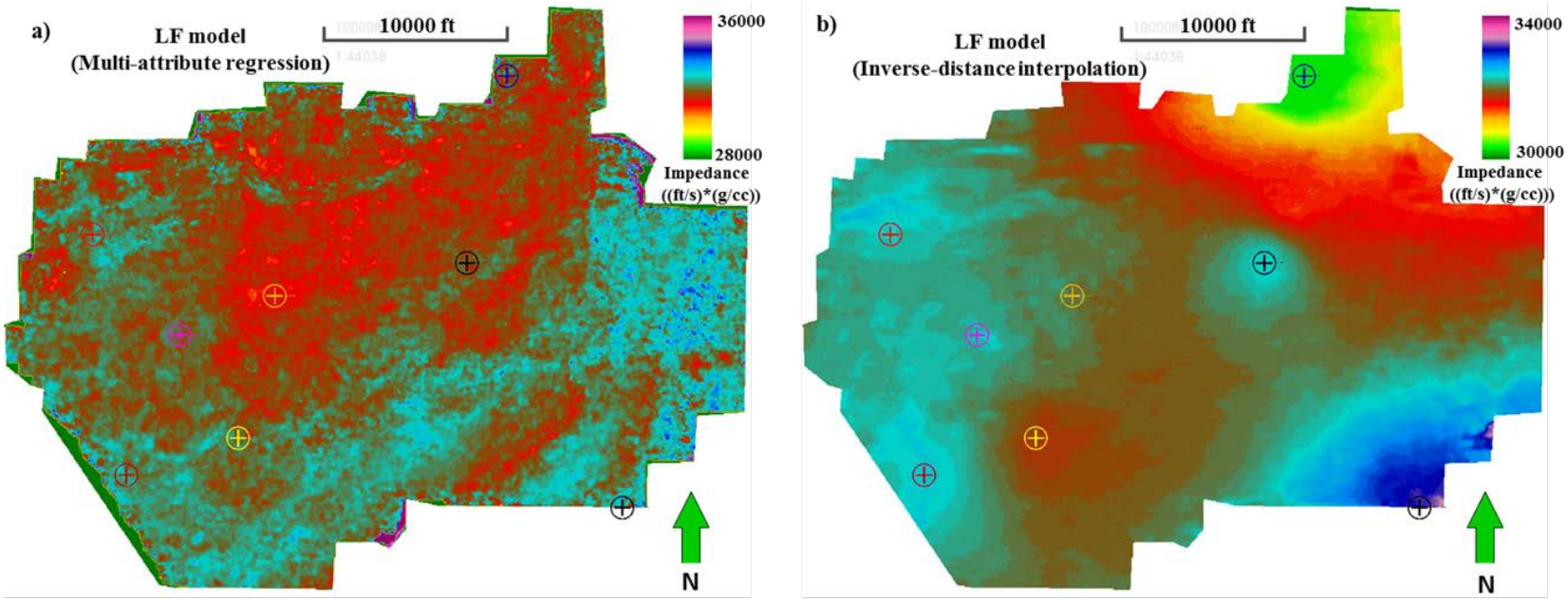

Figure 27. Acoustic impedance (Zp) low-frequency model generated using (a) *multi-attribute regression method* and (b) *inverse-distance interpolation method* on *SU* surface.

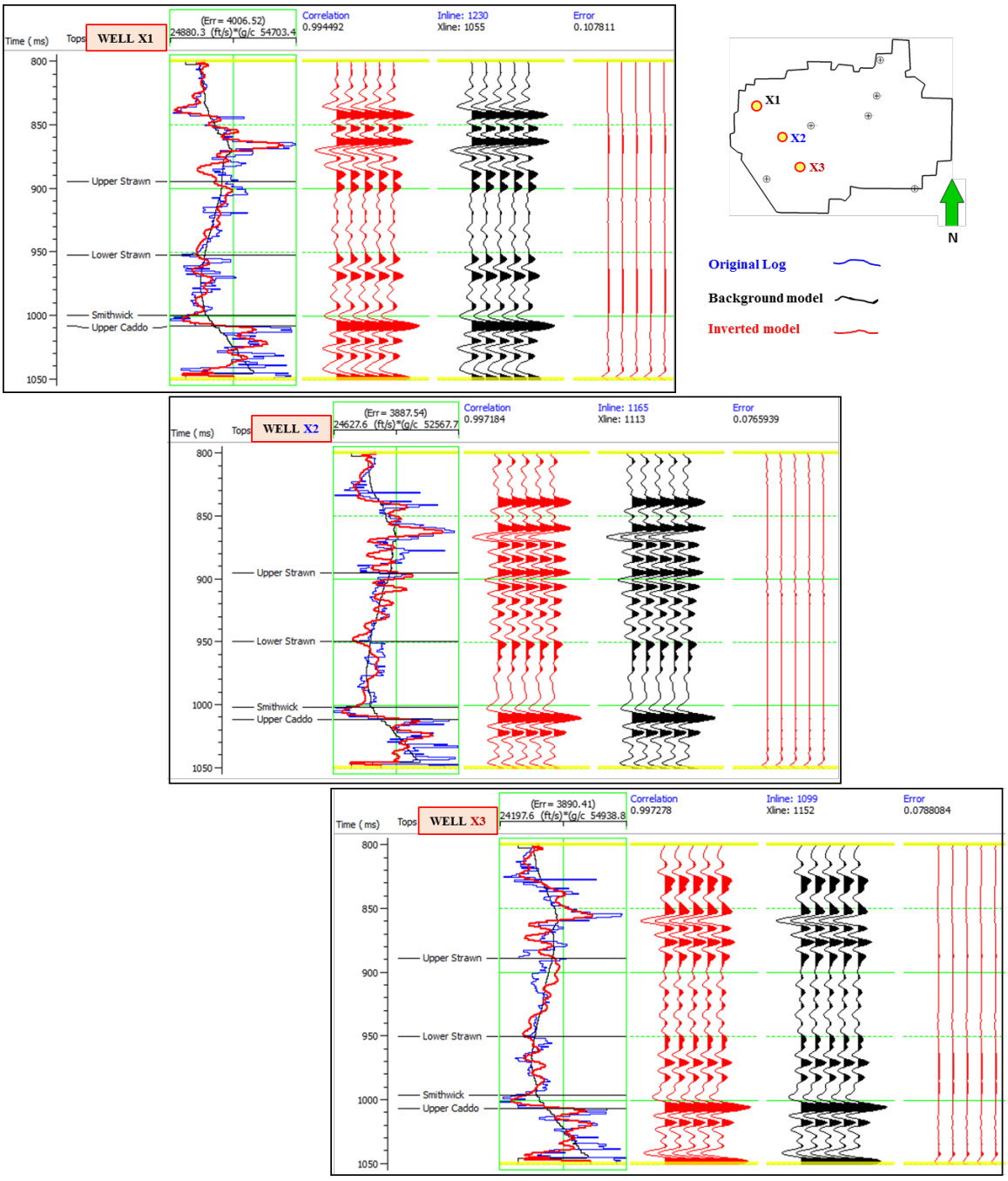

Figure 28. P-impedance analysis results and correlations on wells X1, X2 and X3. These wells were used in the background model which resulting in high correlations.

Inversion error

Next, the inversion results were tested in Hampson-Russell ™ software through the equation (sqrt(Data-inverted_Synˆ2)) (Dr Marfurt Quantitative seismic interpretation class 2016), for which the original stack data and the resulting inverted synthetic need to be used. Figure 29 shows in red areas with high percentage of error corresponding to the higher paleo-topographic areas along the time window analyzed (-800 ms to -1050 ms). On these areas, the horizon interpretation process was difficult due to the lack of reflector continuity. The green arrow indicates an area close to one of the wells with anomalies that must be checked (note that this well has a low error value). The purple arrow points out an area with well information that has a high error value. This well is located on the boundaries of the survey and along the high-error trend area. In this case, this well won't be used in next processes.

At this point, it is important to compare results of this new inversion process to the preliminary one. However, it is also important to see a comparison between different inversion results by using different seismic volumes and different low-frequency models as inputs. To do that, additional P-impedance inversion processes were performed, with the same number of wells but using the following data set as inputs:

- Amplitude volume with Structure-oriented Filtering (SOF) and low-frequency model from *inverse-distance interpolation method.*
- Amplitude volume with Structure-oriented Filtering (SOF) and low-frequency model from *multi-attribute regression method*.
- Reconstructed amplitude volume (from spectral decomposition) and low-frequency model from *inverse-distance interpolation method.*

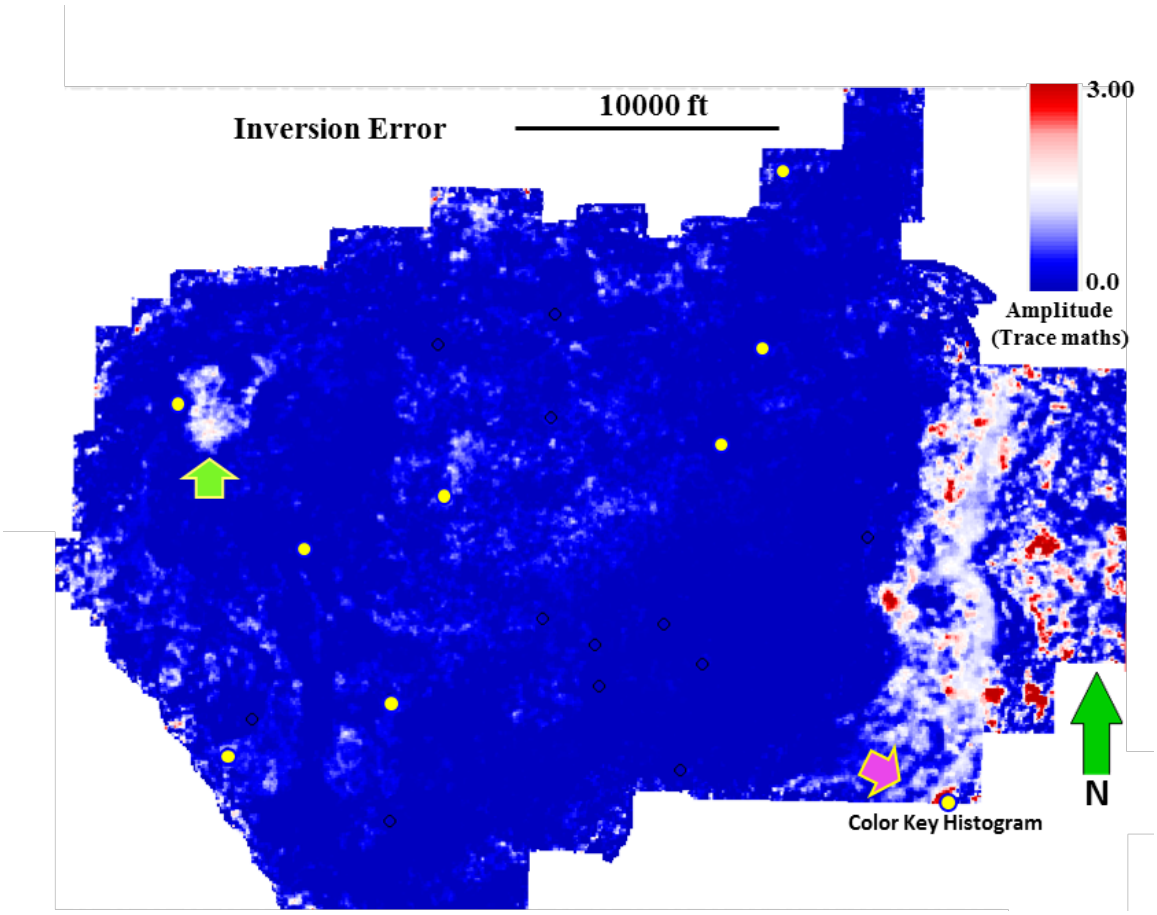

Figure 29. Map showing inversion error. Red indicates area of high error, and blue indicates area of low error. Well location are shown as yellow circles.

With all these processes completed, there are five (5) P-impedance volumes to compare. Figures 31 a - f show these comparisons along an arbitrary NW-SE composite line containing wells X1, X2 and X3 (Figure 30) represented by their Gamma-Ray log.

Inversion results

Figure 31a shows preliminary seismic inversion using just two wells and the default low-frequency model from Hampson-Russell ™. Figure 31b shows the new-final P-inversion (Zp) result that was generated using the spectrally balanced amplitude volume and low-

frequency model from multi-attribute regression method (new LFM). Note the dynamic range change and the enhanced level of detail in the target unit (Lower Strawn Fm) which can support a refining process of previous interpretation and make it possible to differentiate depositional events within the Lower Strawn Fm along this composite line. Figure 31c shows inversion results by using the SOF amplitude volume with the default low-frequency model (inverse-distance interpolation method). Figure 31d shows the resulting impedance volume by using the SOF amplitude volume with the low-frequency model from multi-attribute regression. Figure 31e and 31f are comparing inversion results using the spectrally balanced amplitude volume with the low-frequency model from the inverse-distance interpolation method (e), and low-frequency model from multi-attribute regression (f).

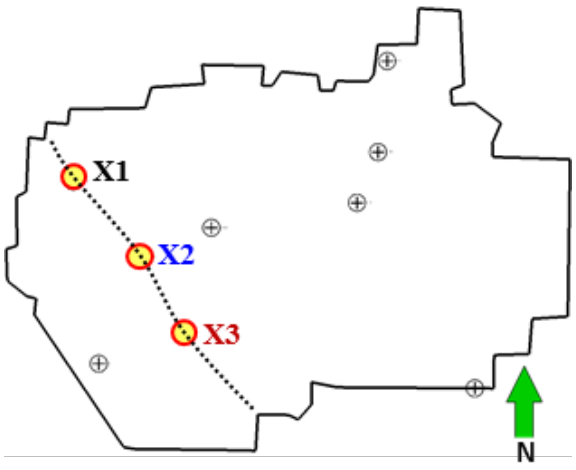

Figure 30. Arbitrary NW-SE composite line containing the wells X1, X2 and X3

Supported on the P-impedance results, a hypothetical model is interpreted separating three different events of deposition (see Figure 32). This model partially can be validated on Figure 33 where clearly can be seen a N-S channel-like shape.

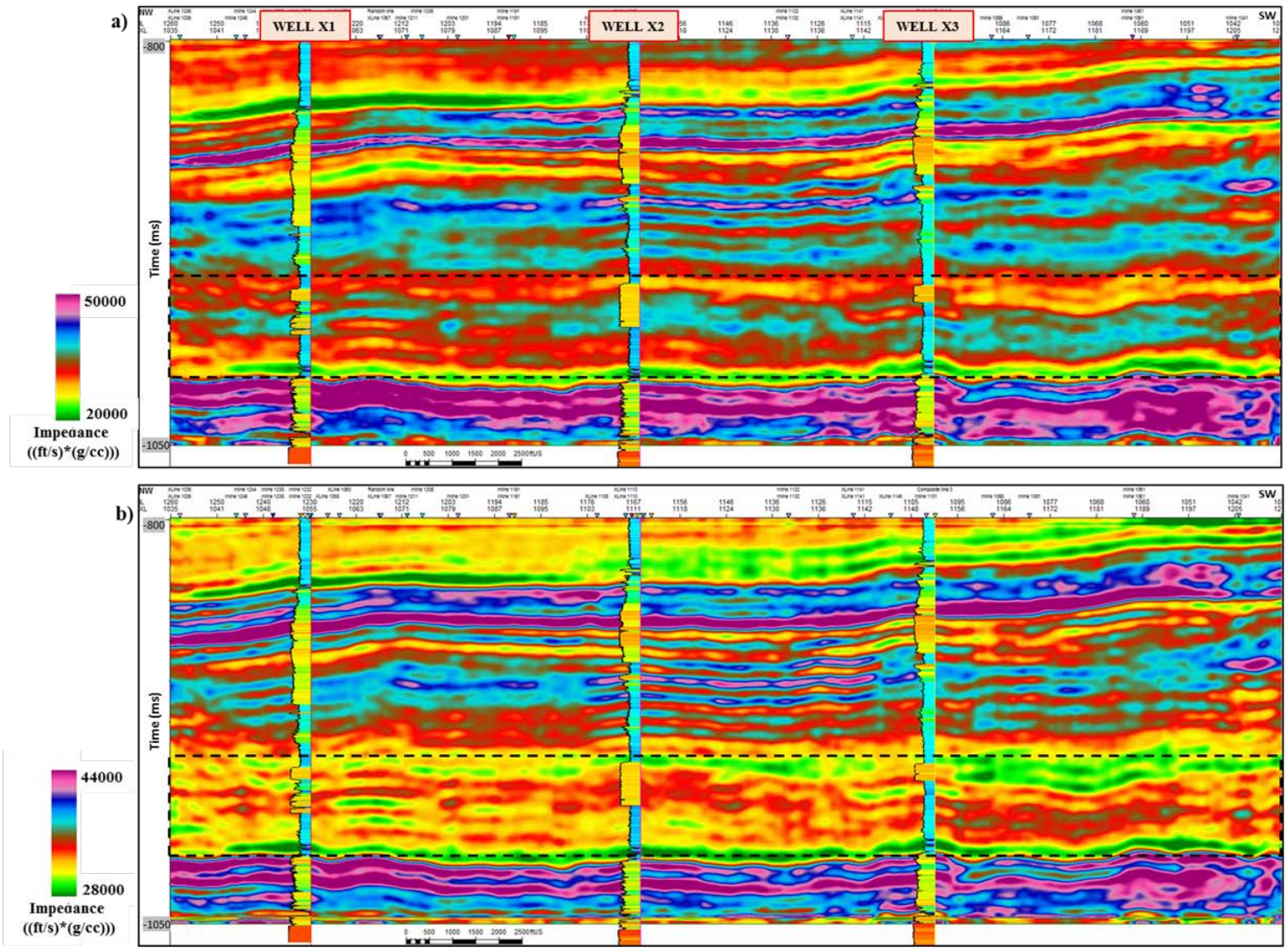

Figure 31. a) preliminary Zp. b) final Zp. Lower Strawn Fm in dotted black square.

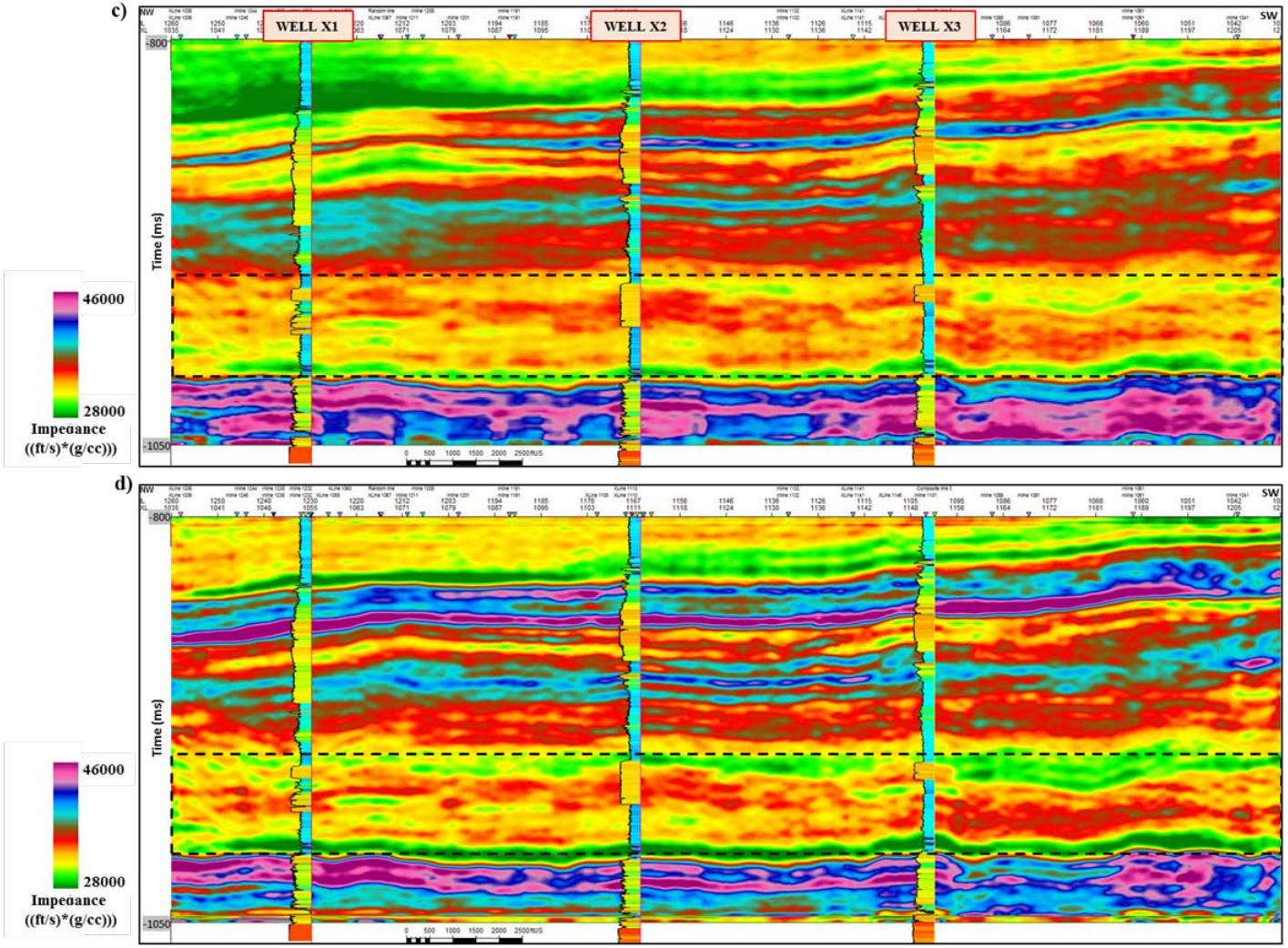

Figure 31. c) Zp from SOF amplitude volume and default LFM d) Zp from SOF amplitude and new LFM method. Lower Strawn Fm in dotted black square..

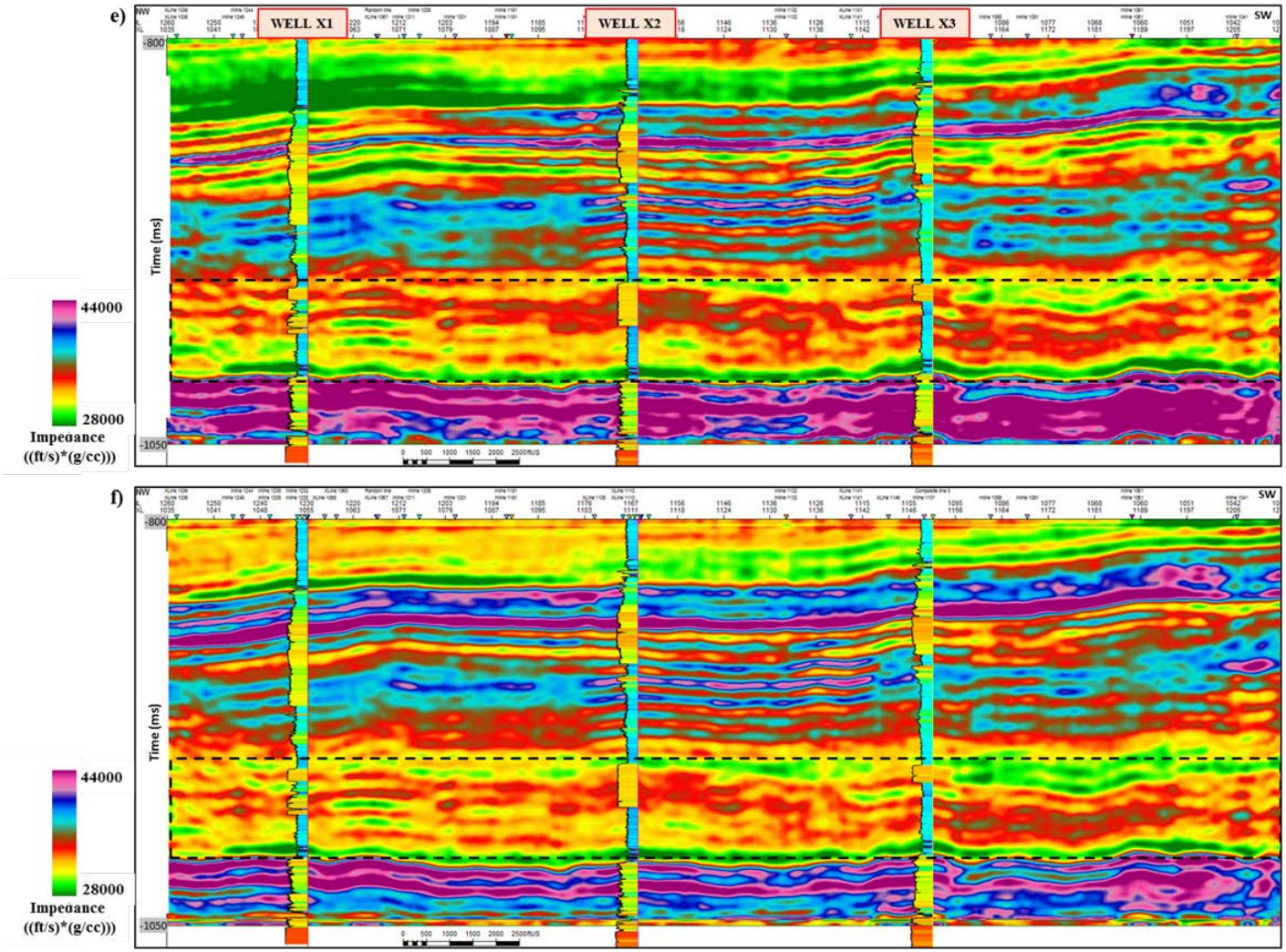

Figure 31. e) Zp from spectrally balanced data and default LFM f) Zp from spectrally balanced data and new LFM method. Lower Strawn Fm in dotted black square.

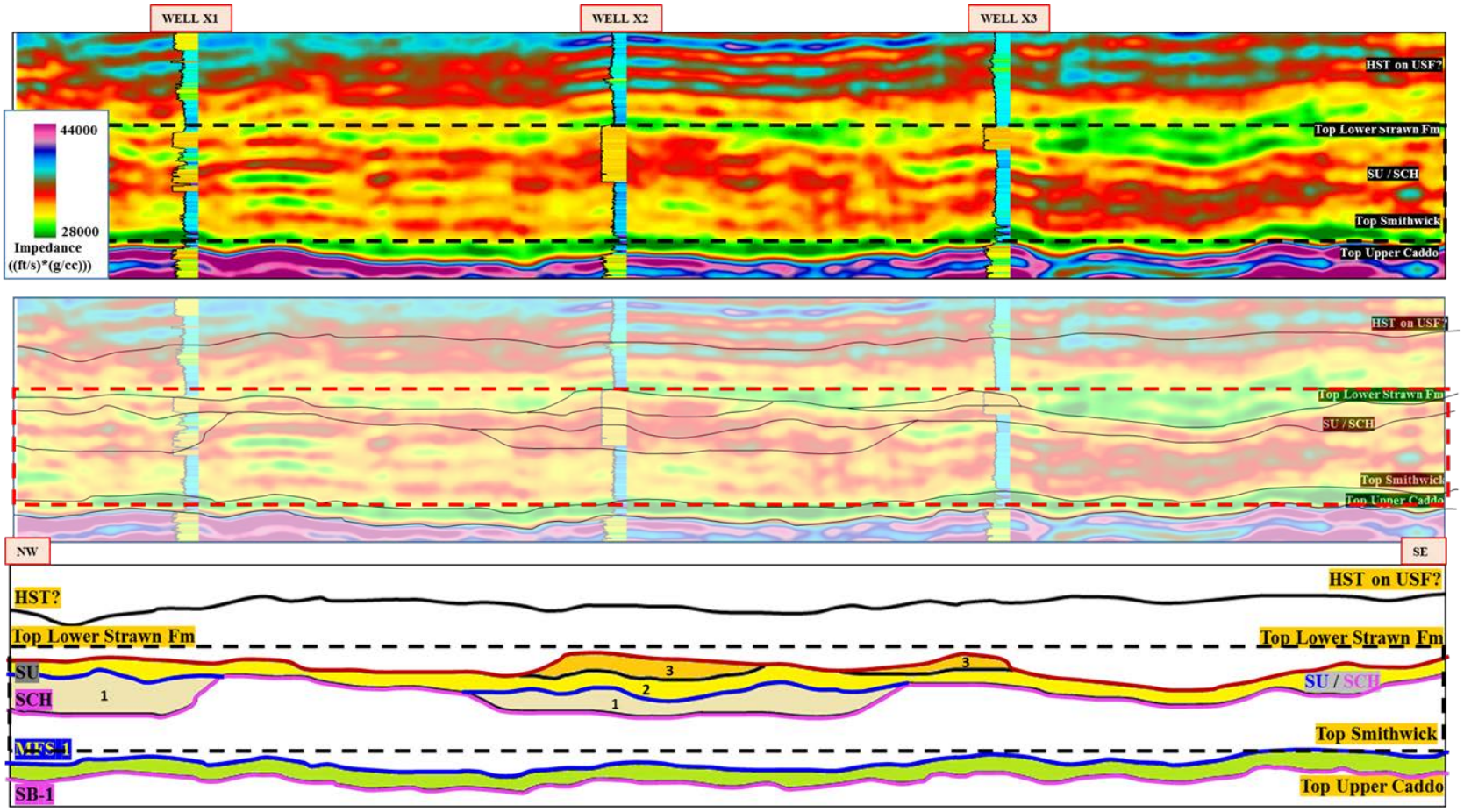

Figure 32. Schematic model along NW-SE composite line in which by using the P-impedance results along with other attributes it is possible to interpret different events within the Lower Strawn Fm. Lower Strawn Fm in dotted square.

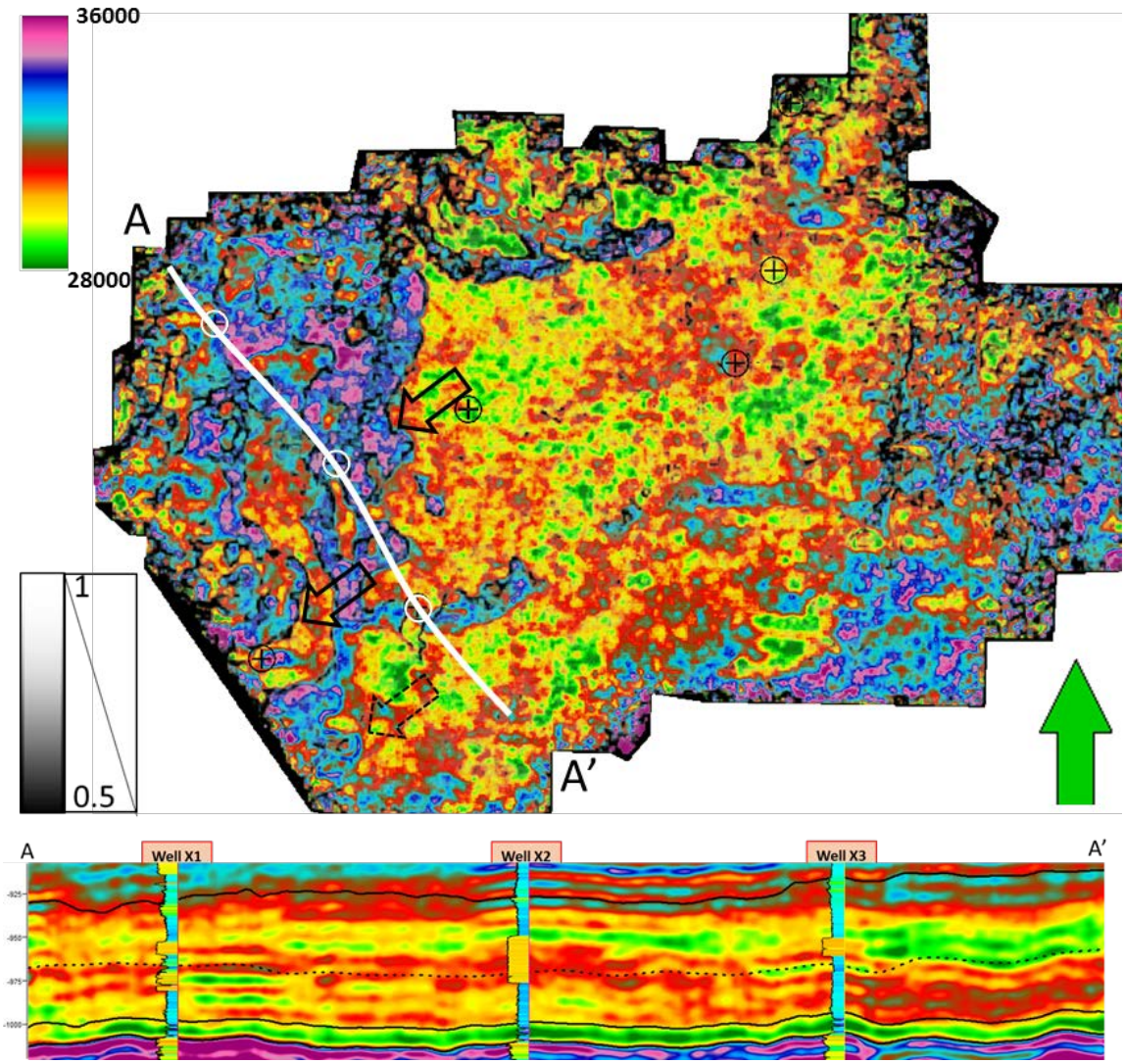

Figure 33. P-Impedance co-rendered with energy ratio similarity on proportional slice through target unit (black dotted line on section A-A'). Black arrows indicate edges of channel-like features. Dotted-black arrow indicates a tiny channel. Wells X1, X2 and X3 in white ovals. White line is representing the location of the cross-section A-A'.

From the analysis of the inversion process it is likely that by using a low-frequency model generated through multi-attribute regression (Ray and Chopra, 2016), the resulting inversion is going to provide more detail to improve ability to interpret.

S-Impedance Prediction and Elastic Parameters

Through the previous processes, it is only possible to 'partially' characterize a reservoir in the acoustic domain. Moreover, applying multi-attribute analysis and probabilistic neural networks, it is feasible to predict the S-impedance volume that, when combined with the P-impedance, gives access to another dimension of results represented by the dynamic elastic modulus (Lambda-Rho, μ-Rho, Poisson ratio, and Young's modulus). These moduli can be mathematically computed from well logs and seismic volumes (P-impedance and S-impedance), thus improving lithology discrimination due to their sensitivity to rock and fluid properties.

S-wave log prediction

It is necessary to check all wells for S-wave log and for those without it (depending on their number), to apply multi-attribute regression to predict them. In this study, only one well (X1) does not have S-wave, which guarantees the confidence of results. *Emerge Log Predict workflow* from Hampson-Russell ™ software was used to determine the optimal number of wells and logs/attributes to use for prediction through a process called "step-wise regression."

Six (6) wells and 3 attributes (logs) were used for this prediction (P-wave**2, Gamma Ray and Density**2), which resulted in a correlation of 99.41% and a validation of 99.35%. Figure 34 to 36 shows the location of the wells used, the cross-correlation between the original and the predicted value and validation results on this log prediction. The next step was to predict the S-impedance volume using logs and seismic attribute volumes through the same methodology adding probabilistic neural networks to the workflow.

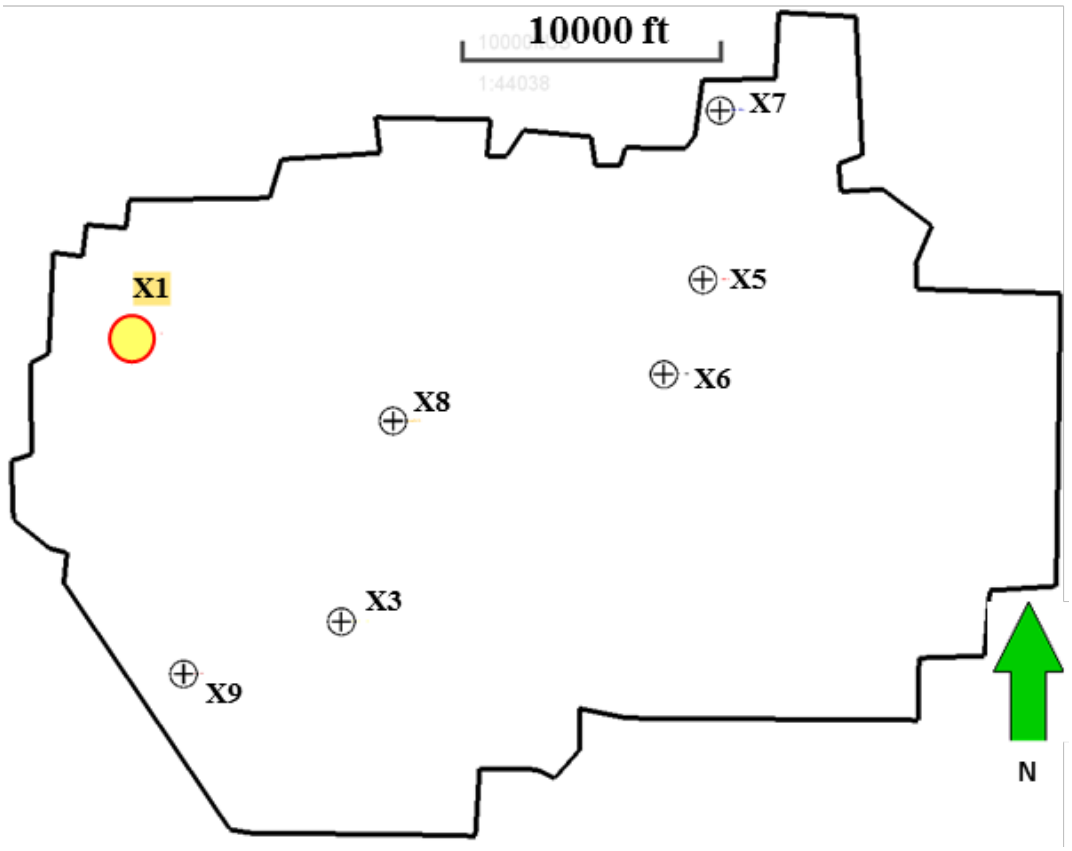

Figure 34. Location map of six wells used for S-wave prediction. In yellow is well X1.

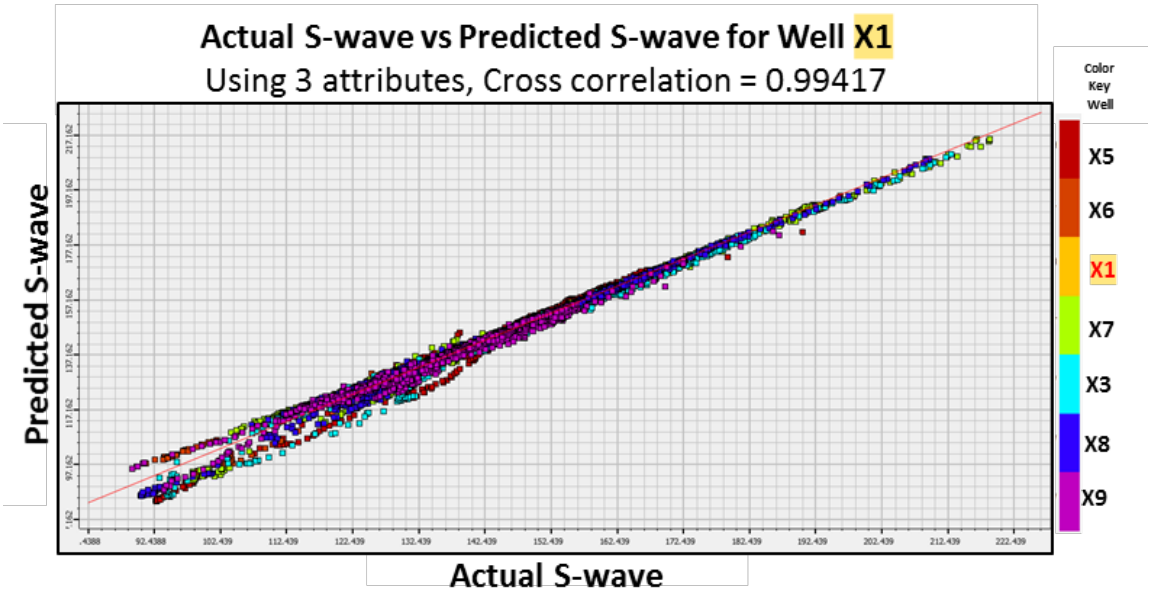

Figure 35. Cross plot of actual S-wave vs predicted S-wave showing a correlation of 99.41%.

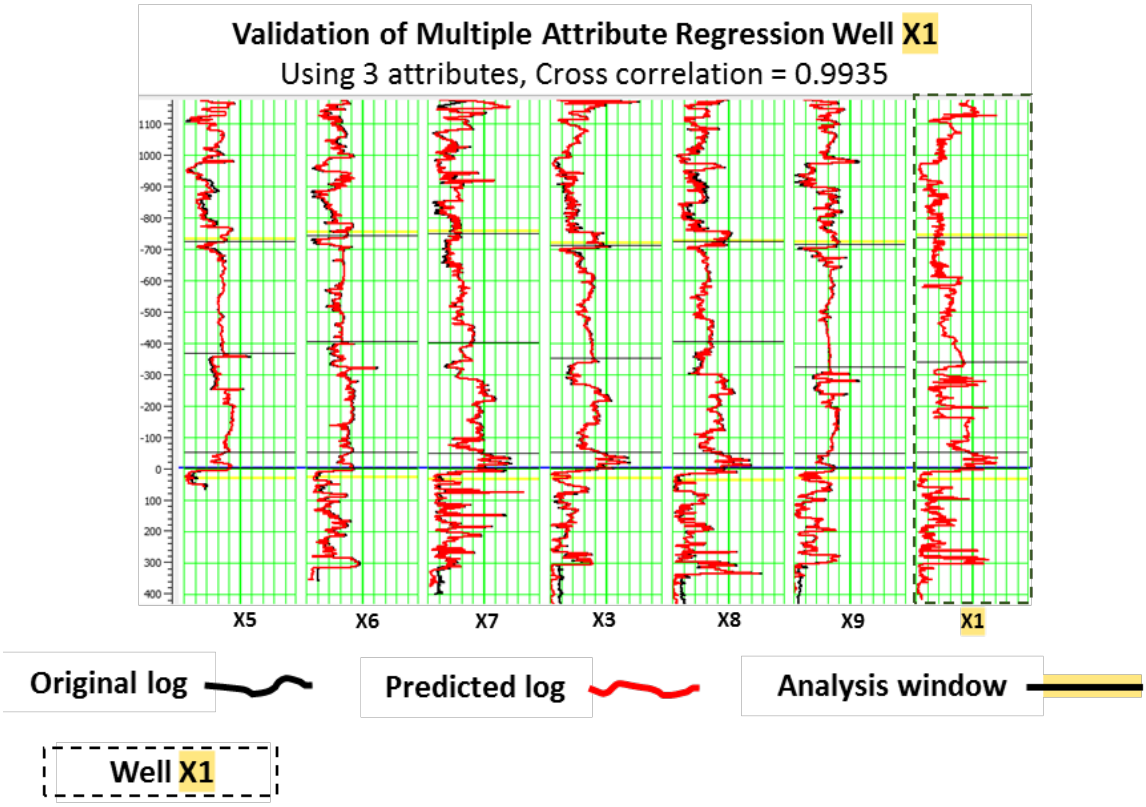

Figure 36. Validation of Multi-Attribute Regression in well X1. For reference, all wells are flattened at the top of the Upper Caddo Fm.

S-Impedance prediction

Input wells for this process were the same as used for the previous P-impedance inversion process (8 wells) plus the well X1 from which S-wave was predicted for a total of 9 wells (see Figure 30). S-impedance (S-wave_velocity * Density) was then computed from logs for all these 9 wells using *Emerge Training and Apply workflow* from Hampson-Russell software ™. Besides the well log information, inputs from some seismic attributes (P-impedance, instantaneous frequency and conditioned seismic amplitude from the time-frequency analysis) were used to run a multi-attribute regression analysis. In this step, the software performs a linear regression between S-impedance from logs and seismic attributes with the best match to the S-impedance log. The initial results show two wells

too far from the average error (X4 and X7), therefore, the process was re-run without these wells; this gave a correlation of 78.79%, an average error of 6.18% and a validation of 75.72% (see Figure 37). The process determines that the seismic attribute with the best match is P-impedance, the optimum number of attributes to be used is 11 and the operator length of 3 points have less validation error (see Figure 40).

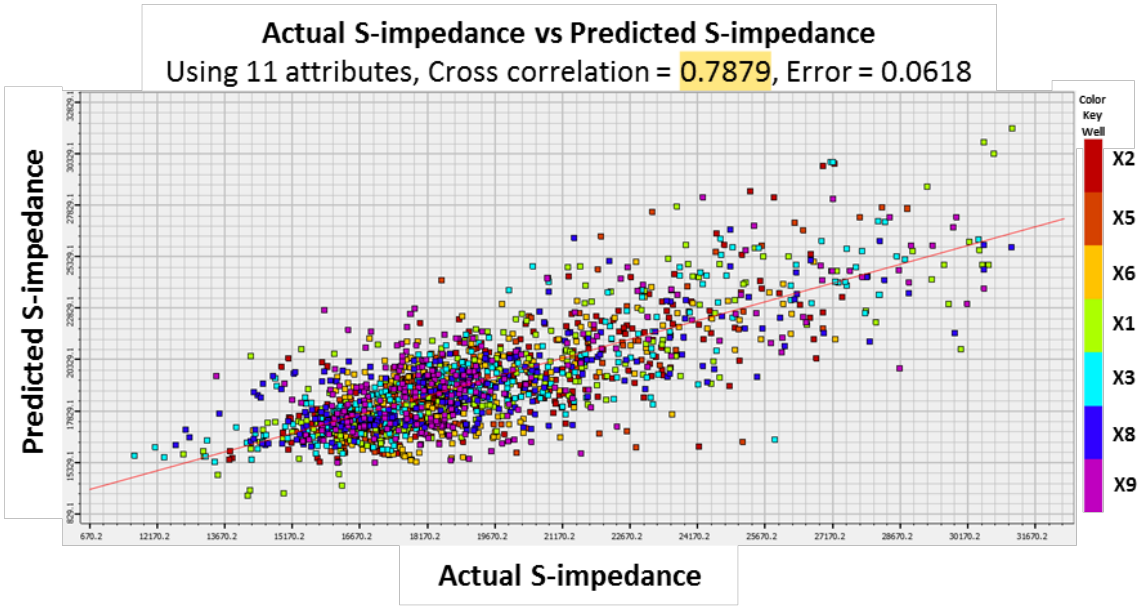

Figure 37. Cross plot of actual S-impedance vs predicted S-impedance from multi-attribute regression analysis. Cross-correlation 78.79%

Notwithstanding, the correlation factor is still too low to be used. Therefore, a Probabilistic Neural Network (PNN) that uses non-linear relationships was applied to correlate the input data (logs and seismic volumes). This process is different than the previous method that used linear regression (Figure 37). Through this method, and with the previous multi-attribute list as input, the cross-correlation improved from 78.79% to 88.58% (see Figure 38), with a validation of 76.57%.

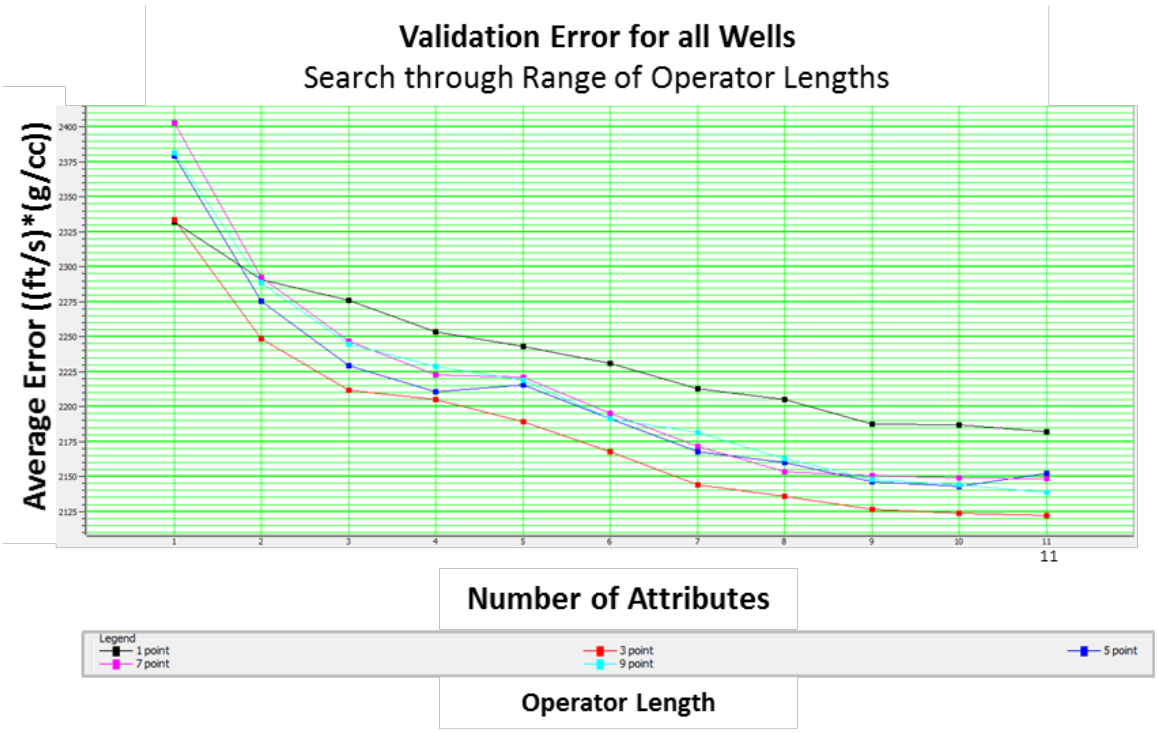

Figure 38. Validation error for all wells used in the multi-attribute regression. Note that the error decreases until reach 11 attributes and using an operator length of 3. This graph was arbitrarily cropped, but as the number of attributes increases, so does the validation error. The 11-attribute used were: *Zp**2, filter 5/10-15/20, filter 15/20-25/30, integrated absolute amplitude, time, filter 45/50-55/60, apparent polarity, filter 35/40-45/50, dominant frequency, derivative instantaneous amplitude, and average frequency.*

Figure 41 shows the improvements in the correlation when passing from linear regression to non-linear regression. Note the enhanced correlation on the target interval (Lower Strawn Fm) by applying PNN in which the predicted S-impedance curve (red) has a better match to the actual S-impedance value (black). This makes the results more reliable for further elastic parameters computation and for interpretation purposes. Figure 42a shows predicted S-impedance results while Figure 42b shows the P-impedance results along an arbitrary cross-section NW-SE. Note that one can better distinguish the sandstones with the S-impedance results than P-impedance (see S-impedance response along NW-SE section and the good match with the Gamma-ray log).

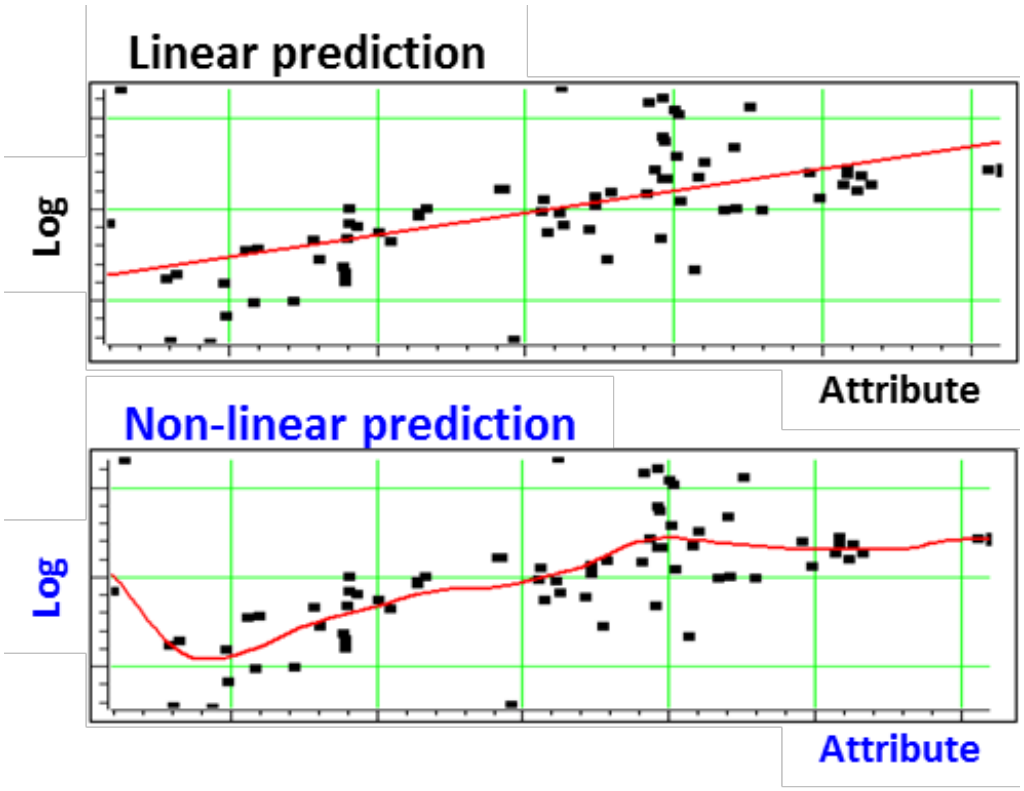

Figure 39. Sketch illustrating differences between Multi-attribute regression (linear) and Neural Network (non-linear). (Modified from CGG Geosoftware 2016)

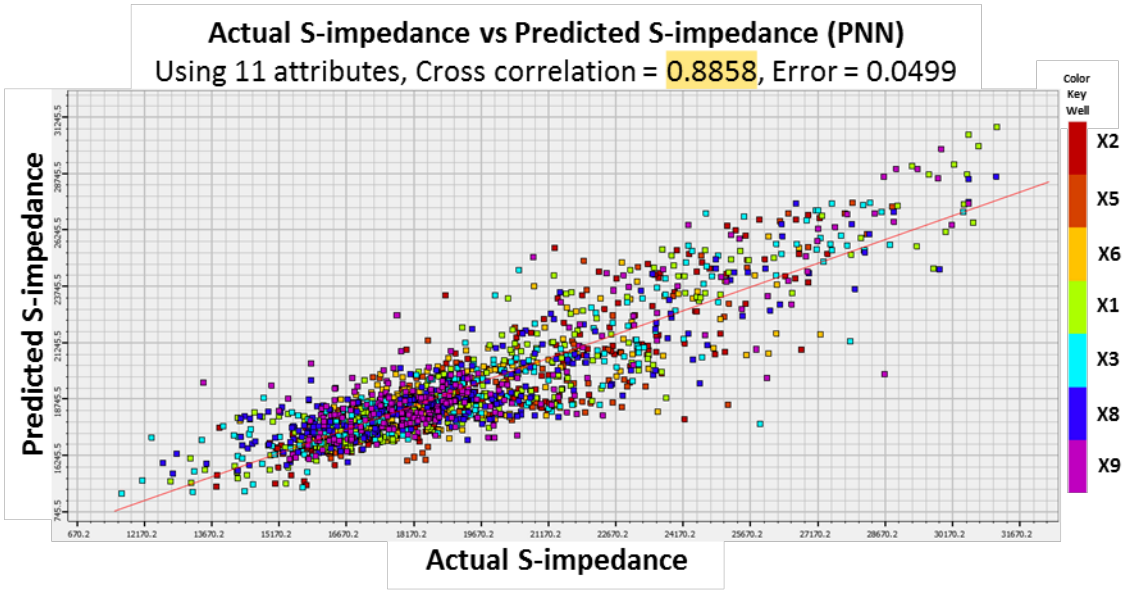

Figure 40. Cross plot of actual S-impedance vs predicted S-impedance from probabilistic neural network using the multi-attribute list previously generated. Cross-correlation 88.58%

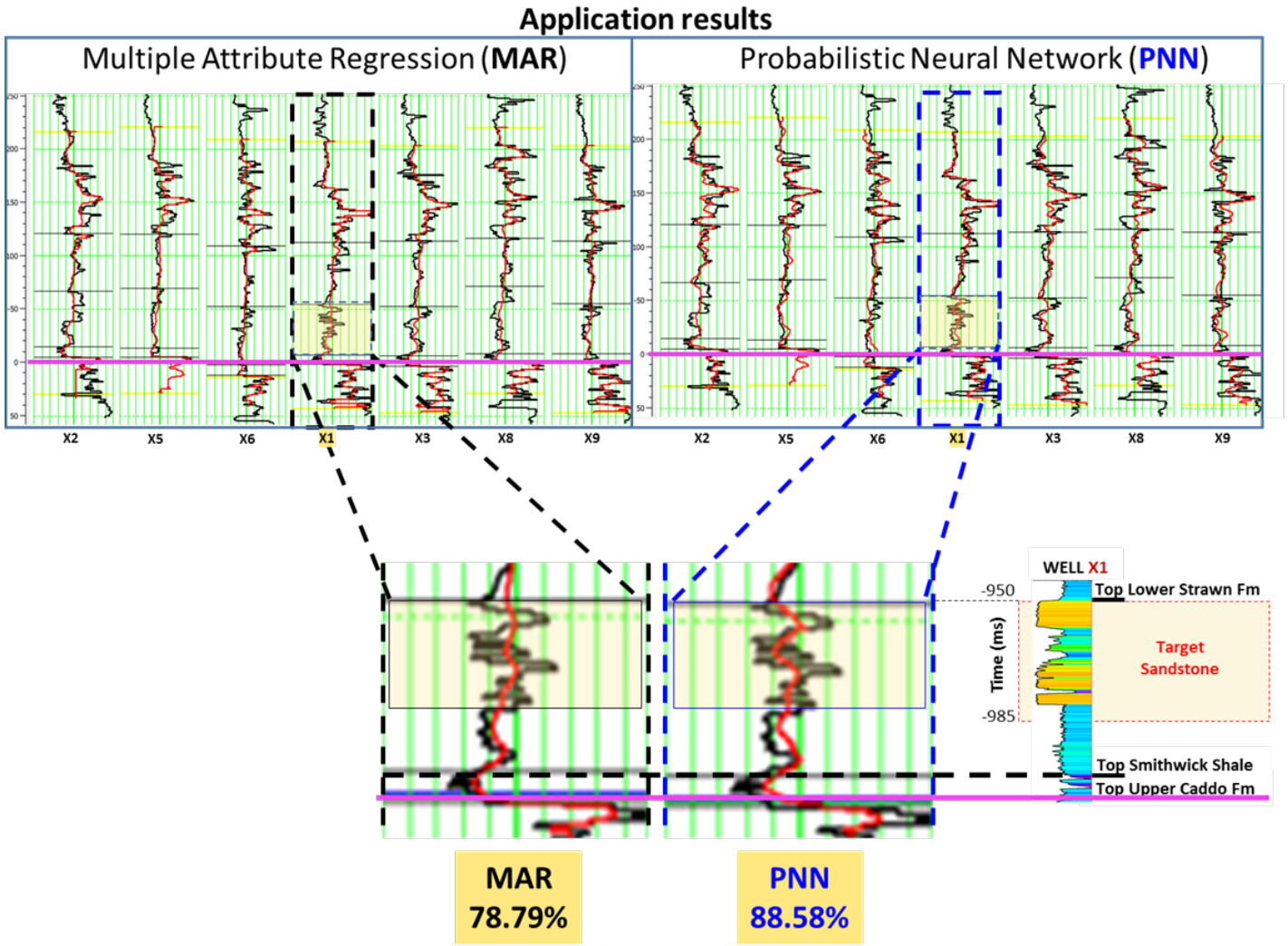

Figure 41. Comparison between results from linear and non-linear methods applied for S-impedance prediction. For reference, all wells are flattened at the Top of the Upper Caddo Fm.

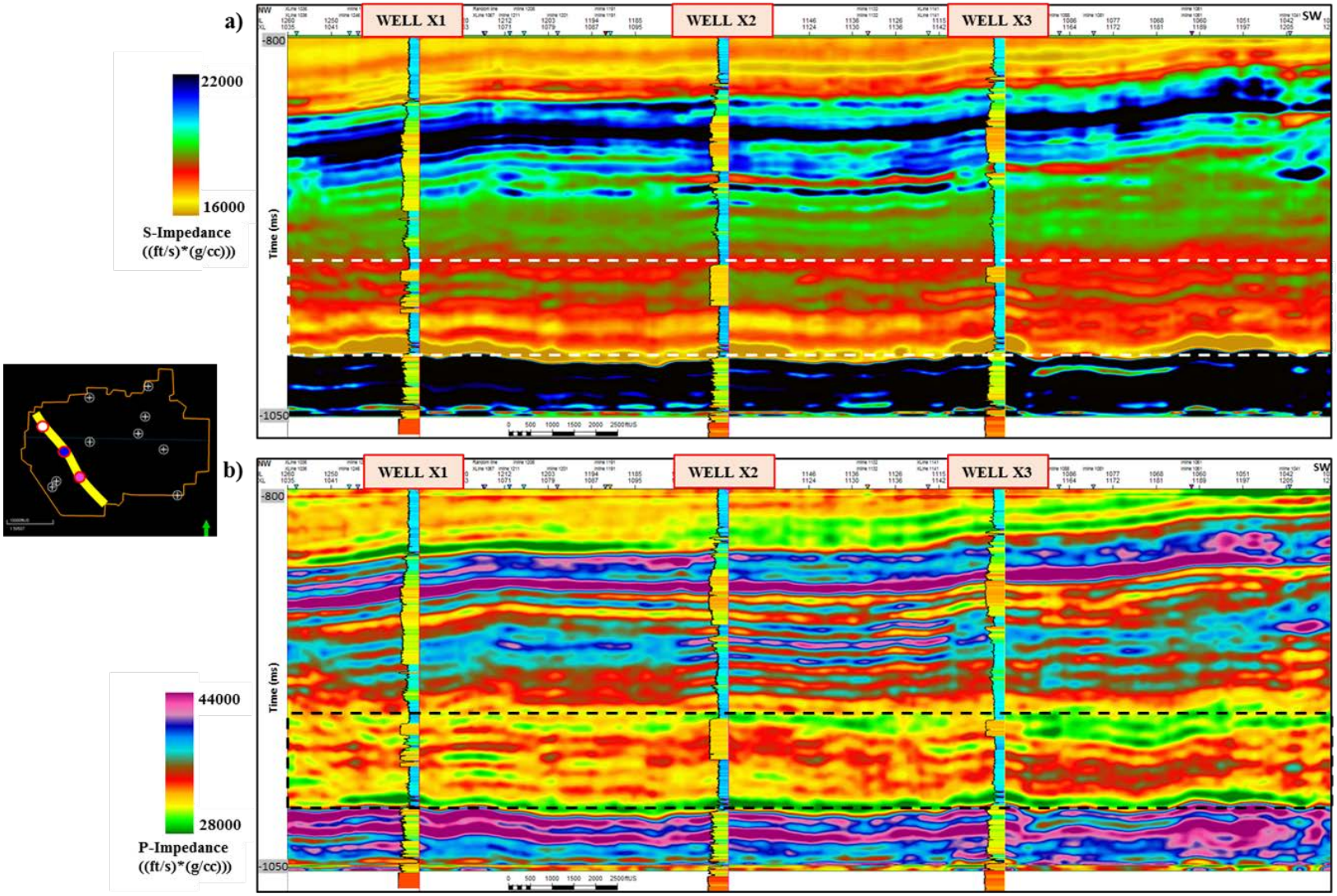

Figure 42. NW-SE vertical section showing a) Predicted S-impedance, b) P-impedance results. Lower Strawn Fm in dotted square.

Elastic parameter computation

Having acoustic impedance, shear impedance and well logs, the elastic parameters of Lambda-Rho, μ-Rho, Poisson ratio, and Young's modulus can be easily computed. This provides a means to extend the relationships between rock /fluid properties and seismic information along the whole 3D volume in order to visualize their variations both horizontally and laterally.

Without the pre-stack inversion, there is no density volume, which is fundamental for computation of Young's modulus. However, this elastic parameter was available in 19 of the 21 digital wells and in 7 of the 9 used for the inversion purposes. In this way, a Young's modulus volume can be predicted as was done for S-impedance. The process is the same as done before by using Hampson-Russell software ™. The property along the 3D volume was predicted using the P-impedance volume, S-impedance, and other attributes. For the volume prediction a cross-correlation of 91.44% using 8 attributes and an operator length of five and PNN was determined.

The following table shows the equations used to compute the four elastic parameters.

Elastic Parameters	**E** Young's modulus (Gpa)	**V** Poisson's ratio	**λρ** LambdaRho	**μρ** MuRho
Equation	$\rho Zs^2(3Zp^2-4Zs^2)/Zp^2- Zs^2$	$\frac{1}{2}(Zp^2- 2Zs^2/Zp^2- Zs^2)$	$\frac{4}{3}\ Zp^2- 2Zs^2$	Zs^2

Where Zp = P-impedance; Zs = S-impedance; and ρ = Density

In addition to these volumes, Zp/Zs ratio, Poisson's impedance (PI), and two attributes of PI, Lithology impedance (LI) and Fluid impedance (FI) were generated.

Poisson impedance

These additional attributes were used with a knowledge of the difficulty of separating sandstones from shales where gas sandstones have similar Zp and Zs response (Charma and Chopra 2013). Poisson impedance as originally presented by Quakenbush et al (2006), was used to allow better discriminating the "litho-fluid distribution" by rotating the axis of the Zp vs Zs plot to be parallel with the correlation trend (Figure 43). The method for calculating the Poisson impedance can be written as:

$$\mathbf{PI = Zp - cZs}$$

Where *c* is the parameter for rotation optimization that for this purpose can be calculated from well logs as the inverse of the slope of the regression line. In this case, figure 41 (right) shows the cross-plot of Zp vs Zs for well X1, with a correlation line slope of 0.601277.

Therefore, ***c*** *= 1/0.601277 = 1.663, then,* **PI = Zp – *1.663**Zs**

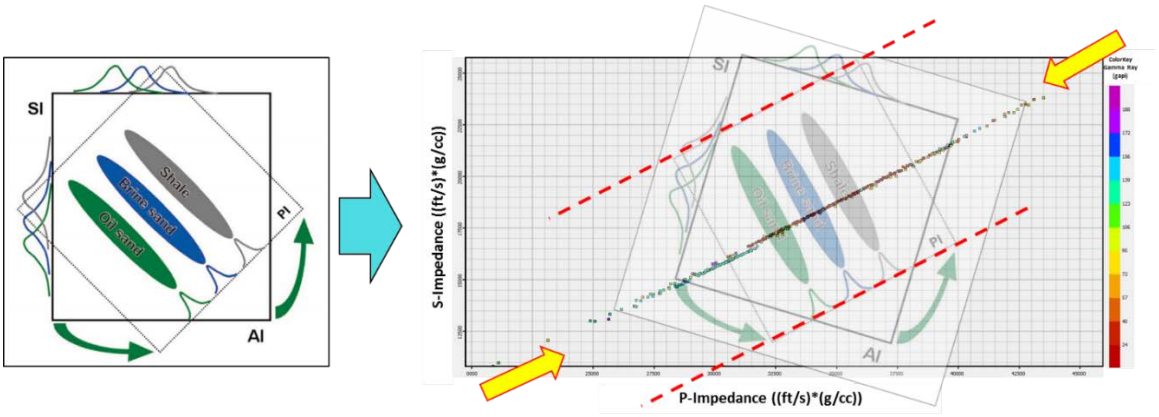

Figure 43. Schematic illustration of Poisson impedance (modified from Quakenbush et al., 2006). Note the axis rotation to be parallel to the regression trend (between the yellow arrows).

Furthermore, by determining the maximum correlation coefficient of PI values to Gamma Ray (GR) and porosity (Ø) logs for different values of *c*, two attributes of Poisson impedance can be computed:

- Lithology impedance (LI) using the value of *c* when the correlation coefficient for GR is maximum
- Fluid impedance attribute (FI) using the value of *c* when the correlation coefficient for porosity (Ø) is maximum.

To calculate the correlation coefficients, it is necessary to use the method called "Target Correlation Coefficient Analysis" (TCCA) (Tian, et al., 2010). The method is illustrated below, using an analog sandstone reservoir.

Lithology impedance (LI) = **PI = Zp – *2.78**Zs**

Fluid impedance (FI) = **PI = Zp – 1.75*Zs**

Poisson impedance (PI) = Zp – *1.663Zs** (calculated previously)

In general, these three additional attributes have strong sensitiveness for lithology or fluid contrast so they were computed along with the other seismic volumes.

This produced 10 elastic-derived attributes volumes to choose and use as inputs for subsequent unsupervised and supervised facies classification.

Chapter 5: Unsupervised and Supervised Facies Classification

A set of facies classification was generated using unsupervised learning techniques (Kohonen self-organizing maps (SOM), K-means clustering classification and generative topographic mapping (GTM). Also, a supervised learning technique (proximal support vector machine or PSVM) was used. In this chapter, the last step is presented in the attempt to seismically characterize the sandstones of the Lower Strawn Fm. by generating a seismic facies classification that discriminates sandstones from shales, and allows further characterization of these sandstone bodies. As inputs, a lot of seismic attribute volumes previously generated during early stages of this thesis (instantaneous, geometric, amplitude, spectral decomposition, acoustic-shear inversion and elastic) were available for further processes (process-1 and 2).

An overview of these classification methods is presented below.

Unsupervised Methods

K-means

Sabeti et al (2009) stated that "k-means clustering algorithm uses an iterative algorithm that minimizes the sum of distances from each sample to its cluster centroid over all clusters. This algorithm moves samples between clusters until the sum cannot be decreased further. The result is a set of clusters that are as compact and well-separated as possible."

Self-Organizing Maps (SOM)

SOM (Kohonen, 2001) clusters data such that the statistical relationship between multidimensional data is converted into a much lower dimensional latent space that preserves the geometrical relationship among the data points. Mathematically each SOM unit within the latent space preserves the metric relationships and topologies of the multidimensional input data. “SOM preserves the original topological structure within this dimensional attribute space, making it amenable for seismic facies analysis” (Chopra and Marfurt, 2008).

K-means vs PCA results

K-means vs PCA calculations were performed to compare results and try to choose the best aproach that preserves the input geometry from P-impedance attribute. In this case k-means over the raw attributes gives a better image (Figure 44 and 45).

Principal Component Analysis (PCA)

PCA was used to reduce the number of attributes to those that are meaningful and that contain the most variability along the whole volume (Roden, 2015). To achieve this goal, the application *pca3D* in AASPI software ™ was used over the ten chosen attributes using the boundaries of the target unit (Top Lower Strawn Fm, Top Upper Caddo) as constraining parameters. Figure 44 shows an illustration of the PCA process.

Generative topographic mapping (GTM)

This technique was developed as an alternative to solve the shortcomings of the Kohonen self-organizing maps and represents a nonlinear dimension reduction method based on Bayesian principles "providing a probabilistic representation of the data vectors in latent space" (Chopra and Marfurt, 2014).

Supervised Methods

Supervised seismic facies classification using proximal support vector machines (PSVM)

This technique is a variant of the initial method of support vector machine (SVM) developed by Cortes and Vapnik (1995), that defines a plane called "decision boundary" separating clusters by support vectors, builds two parallel planes that approximate two data classes, and between these two, the decision-boundary falls (Zhao et al., 2014, 2015). In general, PSVM is a useful supervised technique that in the present case (binary facies classification) can give a meaningful result due to its mathematical meaning.

Process-1(texture attributes)

In this case texture attributes, P-impedance, peak frequency from spectral decomposition, reconstructed data (amplitude), and the relative stratal location were used as inputs to run unsupervised classification techniques. Furthermore, to use just four attributes in this classification, principal component analysis was applied to the eight GLCM texture attributes generated in AASPI (contrast, correlation, dissimilarity, energy, homogeneity, mean, and variance) from which the first principal component (Texture_PCA-1) was used along with the other four attributes.

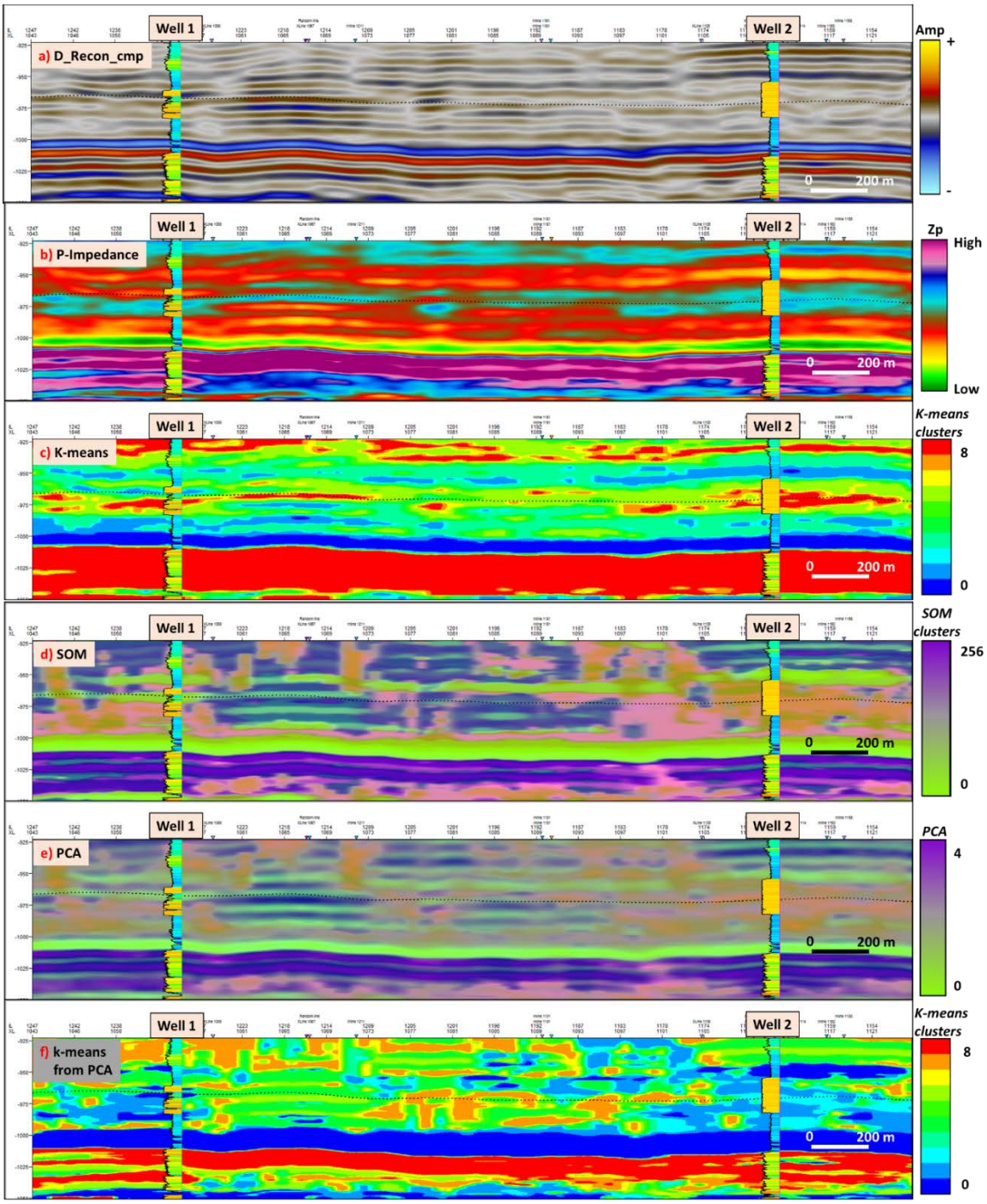

Figure 44 shows 6 cross sections along well 1 and well 2 (*see figure xx-d*) showing the target sandstone unit and the proportional slice through it (black dotted line): (a) reconstructed data (amplitude) from cmp -spectral decomposition algorithm, (b) P-impedance, (c) k-means, d) SOM axis 1 co-rendered with axis 2, e) PCA-1 co-rendered with PCA-2, f) k-means from PCA.

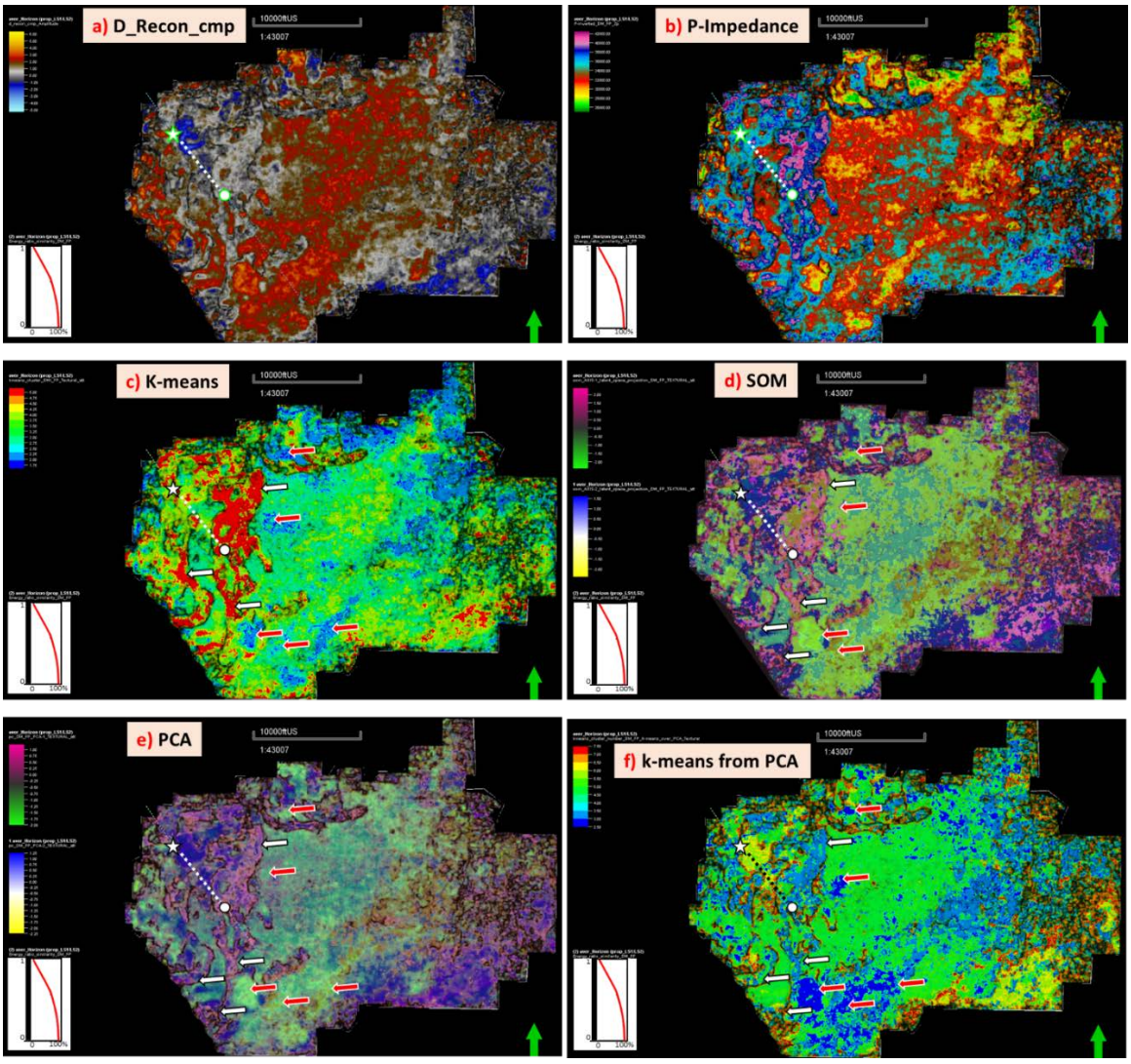

Figure 45 shows a proportional slice along the target sandstone (well-1-star, well-2-circle) (*see figure 42*) within the Lower Strawn Formation: (a) reconstructed data (amplitude) from cmp -spectral decomposition algorithm, (b) P- impedance, (c) k-means, d) SOM axis 1 co-rendered with axis 2, e) PCA-1 co-rendered with PCA-2, and e) k-means from the four principal components after PCA.

Process-2 (Elastic attributes)

Since the goal of the thesis was to lithologically differentiate the target unit (sandstone bodies of the Lower Strawn Fm), input attributes computed from P-impedance and S-impedance (elastic attributes) were used for process-2. These attributes have a closer relationship to the rock properties. However, that still leaves ten attribute-volumes. How

does one know which are the best attributes to use? Not all attributes contribute with the same weight, so those less representative attributes must be omitted in order to avoid introducing noise into the process. To overcome this situation, a multi-attribute analysis using principal component analysis (PCA) was performed (Figure 46)

a)

#	Attribute Name	Scaled Eigenvectors									
		1	2	3	4	5	6	7	8	9	10
1	Computed Youngs Modulus (CYM)	-8.05E-02	4.75E-01	1.87E-01	8.54E-01	-2.00E-04	5.73E-02	-6.03E-03	-9.48E-04	-2.53E-06	2.06E-06
2	Fluid Impedance (FI)	4.01E-01	-1.10E-02	-1.04E-02	4.71E-02	-1.39E-01	-7.29E-03	1.06E-02	3.53E-01	-3.55E-01	6.52E-01
3	Lambda-Rho	3.78E-01	1.72E-01	-8.95E-03	-6.57E-02	-3.44E-01	3.56E-02	-6.47E-01	-5.33E-01	-5.26E-04	1.05E-03
4	Lithology Impedance (LI)	3.58E-01	-2.37E-01	-7.34E-03	1.54E-01	-1.31E-01	1.92E-01	-6.77E-02	3.38E-01	3.09E-01	1.35E-01
5	Mu-Rho	-5.04E-02	5.15E-01	1.56E-02	-3.45E-01	1.47E-01	7.42E-01	-5.58E-02	1.95E-01	1.78E-04	-3.78E-04
6	Poisson Impedance (PI)	3.94E-01	9.97E-02	-1.12E-02	-8.26E-03	-1.33E-01	-1.04E-01	4.80E-02	3.32E-01	5.41E-01	-4.26E-01
7	Poisson ratio (PR)	3.96E-01	-2.42E-02	-4.16E-02	6.45E-02	8.89E-01	-8.55E-02	-1.69E-01	-1.07E-01	-1.09E-04	2.09E-04
8	P-Impedance (Zp)	2.84E-01	3.69E-01	-1.06E-02	-1.53E-01	-8.73E-02	-3.35E-01	1.36E-01	2.09E-01	-5.53E-01	-4.13E-01
9	Zp/Zs ratio	4.00E-01	-3.26E-02	4.96E-03	4.08E-02	-8.40E-02	2.73E-01	7.03E-01	-5.12E-01	-4.80E-04	9.72E-04
10	S-Impedance (Zs)	-5.61E-02	5.17E-01	-2.96E-03	-2.61E-01	3.50E-02	-4.50E-01	1.74E-01	-1.04E-01	4.24E-01	4.53E-01

b)

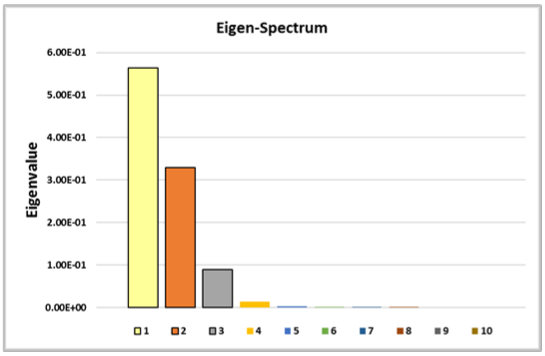

c)

Eigenvalues (fraction of data variability)		
Eigenvalue no.	Fractional Ene	Percentaje
1	5.63E-01	56%
2	3.30E-01	33%
3	8.97E-02	9%
4	1.32E-02	1%
5	2.81E-03	0%
6	9.85E-04	0%
7	3.47E-04	0%
8	5.85E-06	0%
9	1.90E-08	0%
10	-6.63E-09	0%

d)

#	Attribute Influence	Principal Component Analysis Results			
		1	2	3	Percentage
1	Zp	2.84E-01	3.69E-01	-1.06E-02	14%
2	Lambda-Rho	3.78E-01	1.72E-01	-8.95E-03	14%
3	PI	3.94E-01	9.97E-02	-1.12E-02	13%
4	FI	4.01E-01	-1.10E-02	-1.04E-02	11%
5	Zp/Zs	4.00E-01	-3.26E-02	4.96E-03	11%
6	PR	3.96E-01	-2.42E-02	-4.16E-02	11%
7	Mu-Rho	-5.04E-02	5.15E-01	1.56E-02	7%
8	Zs	-5.61E-02	5.17E-01	-2.96E-03	7%
9	CYM	-8.05E-02	4.75E-01	1.87E-01	6%
10	LI	3.58E-01	-2.37E-01	-7.34E-03	6%

Figure 46. Results from Principal Component Analysis in AASPI ™ utilizing 10 attributes.

Figure 46a shows the scaled Eigenvectors are given. Figure 46b shows the histogram of the eigenvalues for all attributes. Note that the first three eigenvalues dominate the

spectrum. In Figure 46c the percentage contribution of each Eigenvalue are given. Figure 46d shows the resulting attribute-influence order and their percentage contribution in the three principal components. This was achieved after some simple arithmetic using data in a) and c). From this process, the first six attributes (see Figure 46d) representing 73% of all variability along the data set were chosen to be used for GTM and PSVM. Eigenvalue and Eigenvector as stated by Roden (2015) defines: "An eigenvalue is the value showing how much variance there is in its associated eigenvector and an eigenvector is the direction showing the spread in the data."

Results and comparison

Figures 47 a-f, show a series of 2D views of the same time slice (-969 ms) and their respective NW-SE vertical section (enclosed in the Lower Strawn Fm), with the resulting unsupervised and supervised processes. One can visualize the channel-like features in each one of them. However, only in some of them it is possible to attempt to discriminate seismic facies as channel-fill deposits, point bars, fans, and overbank deposits (SOM, GTM and PSVM).

Figures 47e, f, shows the results from GTM and PSVM processes. Two facies were identified, yellow (Sandstone) and blue (Mudstone). The results are displayed on a NW-SE cross-section that contains three wells (X1, X2 and X3) and a 2D view of the proportional slice depicting the facies generated. Figure 47e, results from PSVM and Figure 47f results from GTM.

Furthermore, the results from PSVM can be correndered with the elastic volumes to obtain a different insight about the changes in the reservoir properties along the area. In this way, it is feasible to visualize changes along an apparent same sand body (see Figure 48).

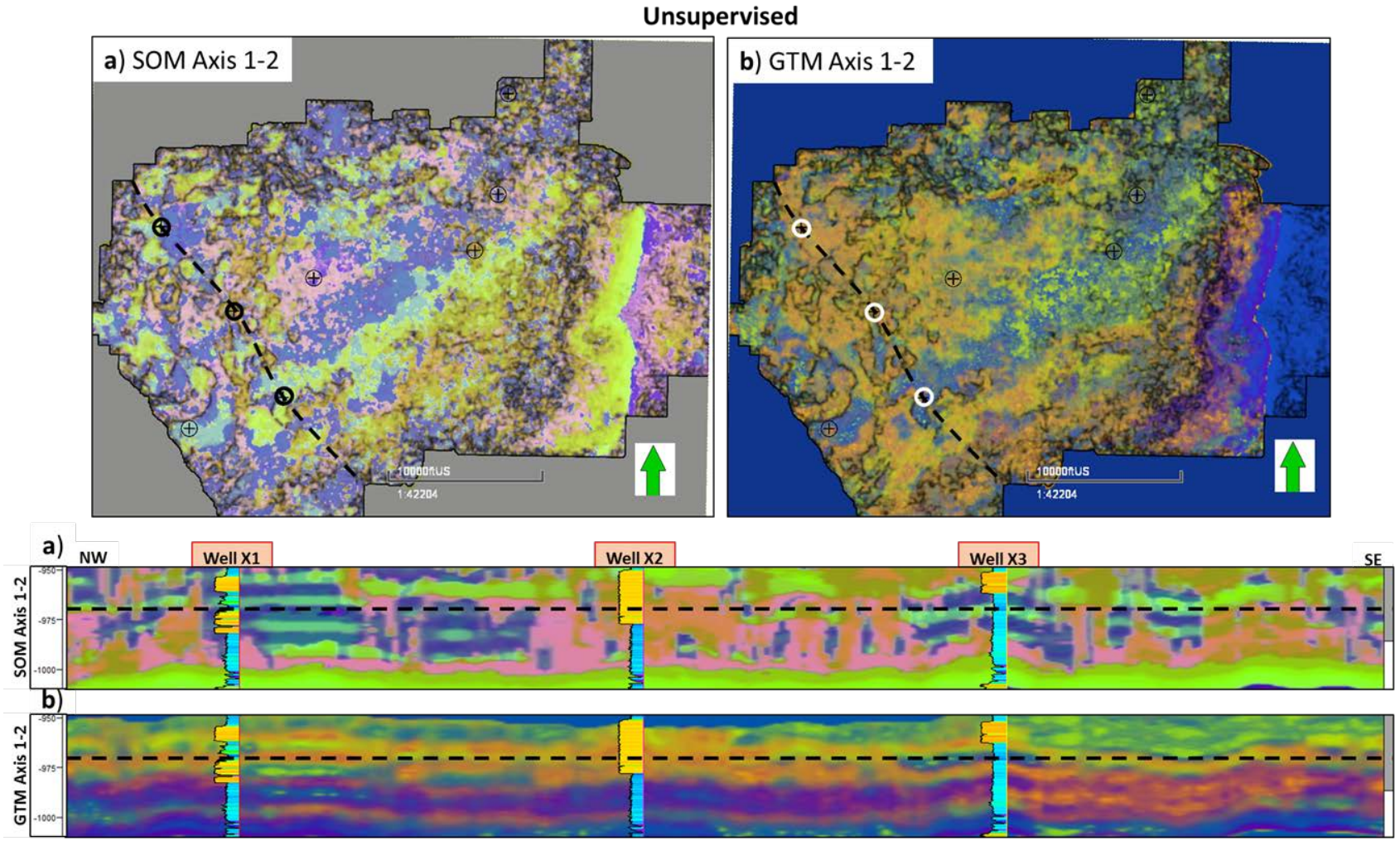

Figures 47. a) SOM and b) GTM axis 1 and 2. Dotted black line represents the cross section and time slice location. Ovals on 2D view represents the well locations

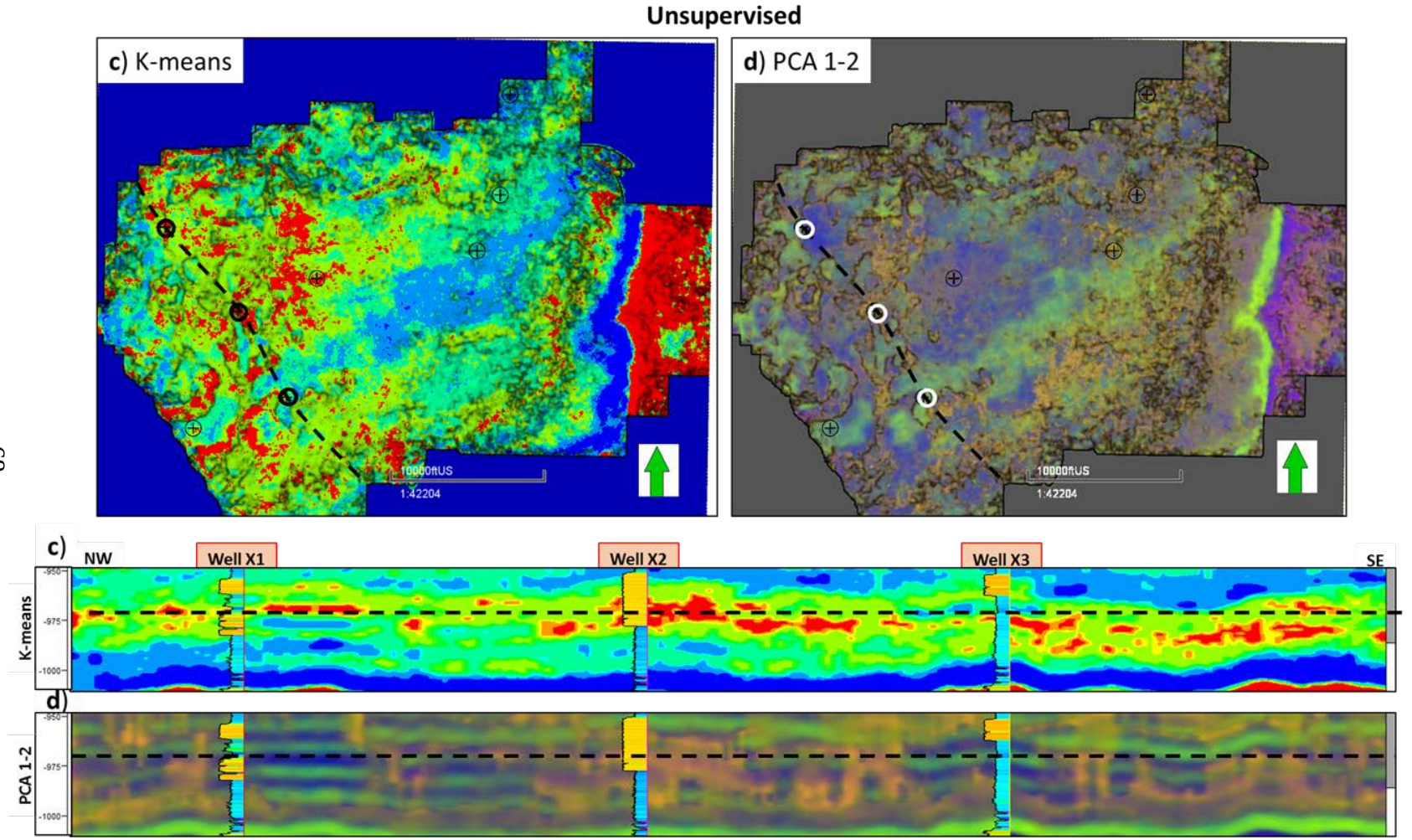

Figures 47. c) K-means and d) PCA 1 and PCA 2. Dotted black line represents the cross section and time slice location. Ovals on 2D view represents the well locations

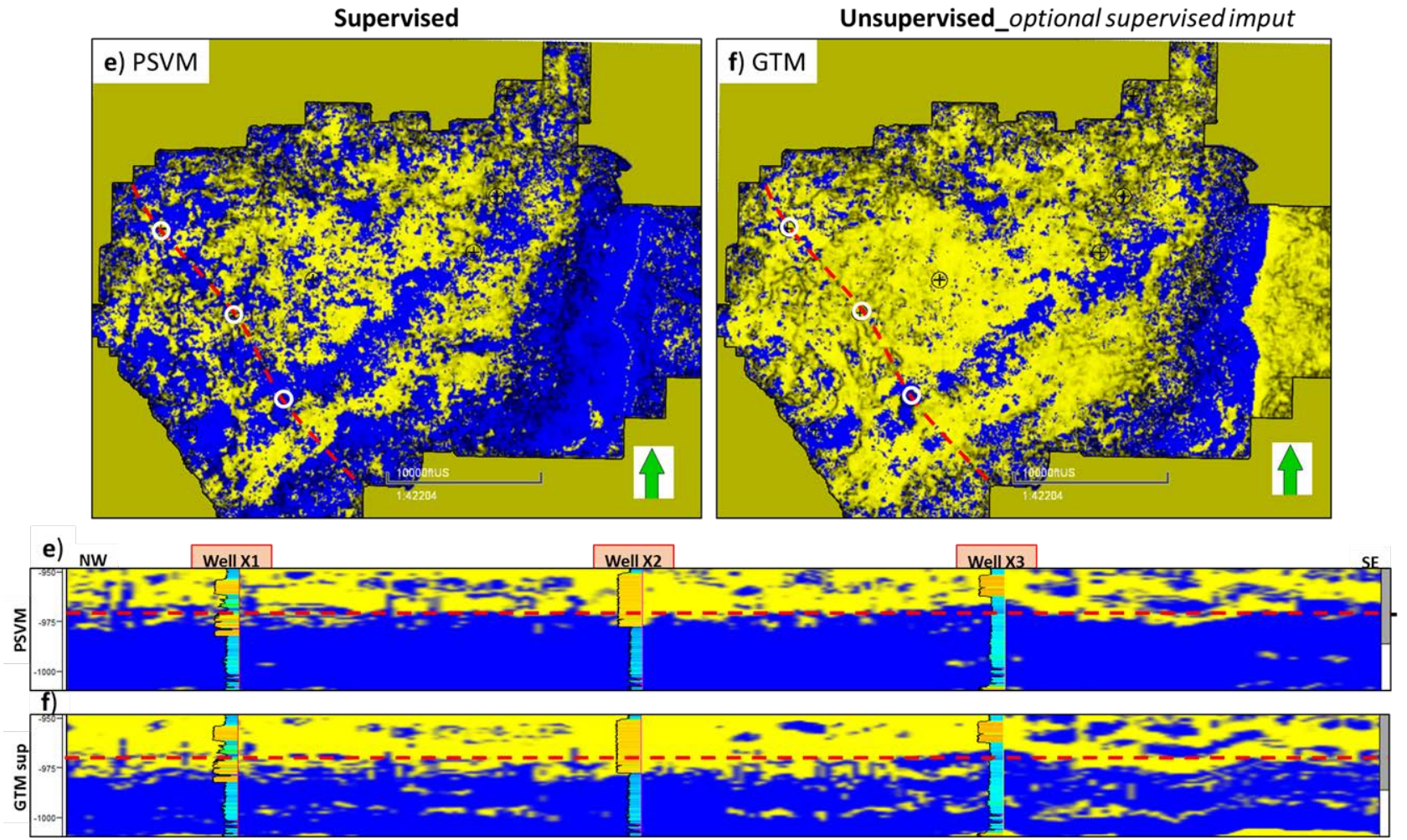

Figures 47. e) PSVM and f) GTM_*optinal supervised imput*. Dotted red line represents the cross section and time slice location. Ovals on 2D view represents the well locations

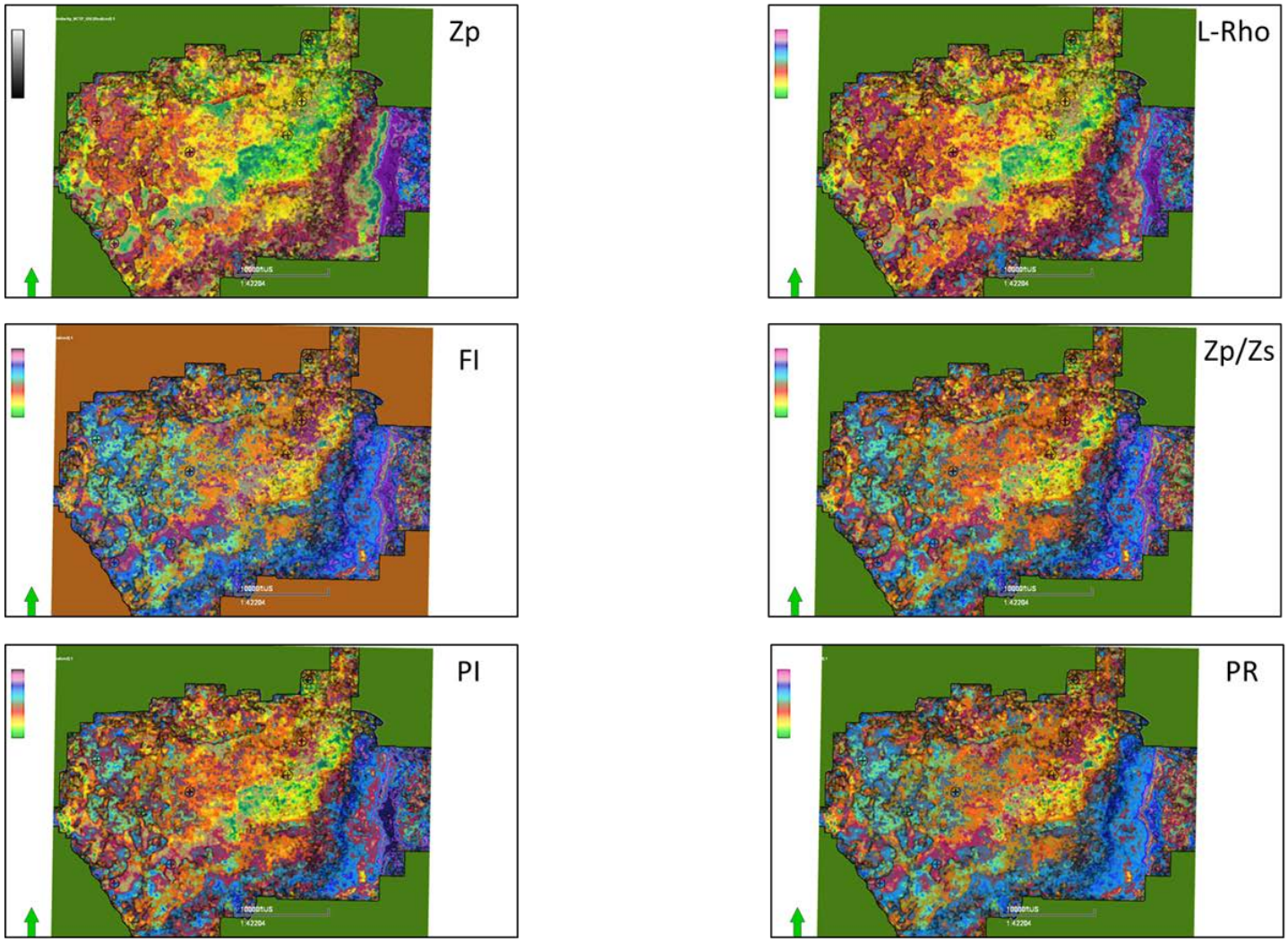

Figures 48. Seismic facies classification from PSVM correndered with each one of the six elastic volumes used to run the process.

From Figure 48 it is visualizing that even when it is the same facies (sandstone-yellow), when it is correndered with different elastic attributes, it is possible to discriminate different types of sandstones based upon their rock properties which also are making visible the channel-like features and different seismic facies.

From these previous results, the P-impedance will be used to validate the results on well logs (see Figure 49. Figure 50 is showing a 3D view of the selected time slice with the correndered attributes. By visualizing the Gamma-ray log response over the seismic attributes, is clear the there is a match between the well logs and the seismic facies classification. White arrows are showing the log response (shale) over the seismic attribute corresponding to shale. In the same way the black arrow is pointing out the match between the log response in well X2 and the seismic facies classification results.

Figure 51 is showing a tentative interpretation of the architectural elements cutting through a proportional slice. Some of the seen features are more evident than other; however, is clearly that by correndering the seismic facies classification resulting from the supervised method (PSVM-two facies) and the P-impedance, it is possible to extract some variations within the reservoir that show up easily these architectural elements.

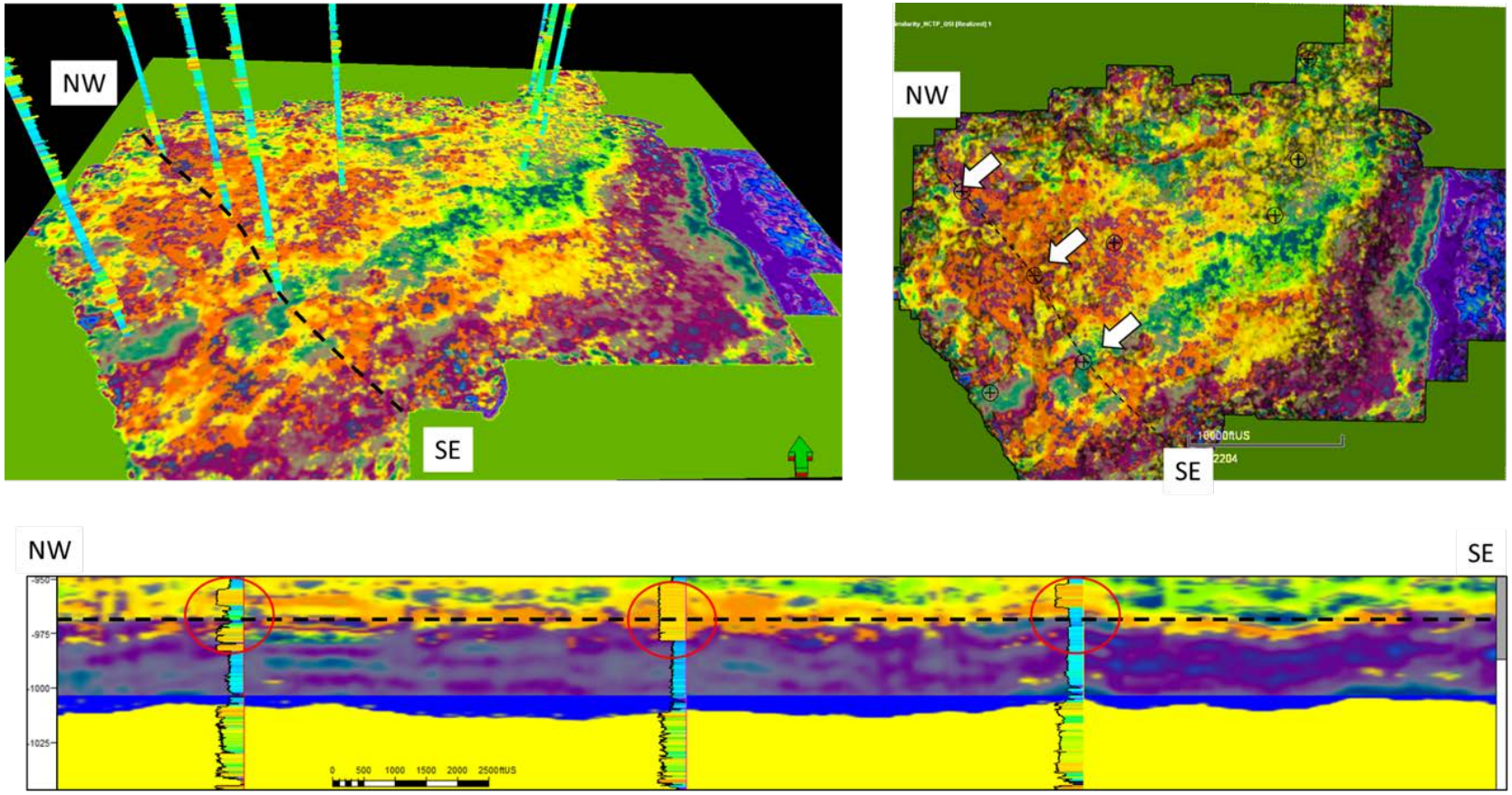

Figures 49 is illustrating on 2D, 3D and vertically, the results of the facies classification using PSVM correndered with P-impedance.

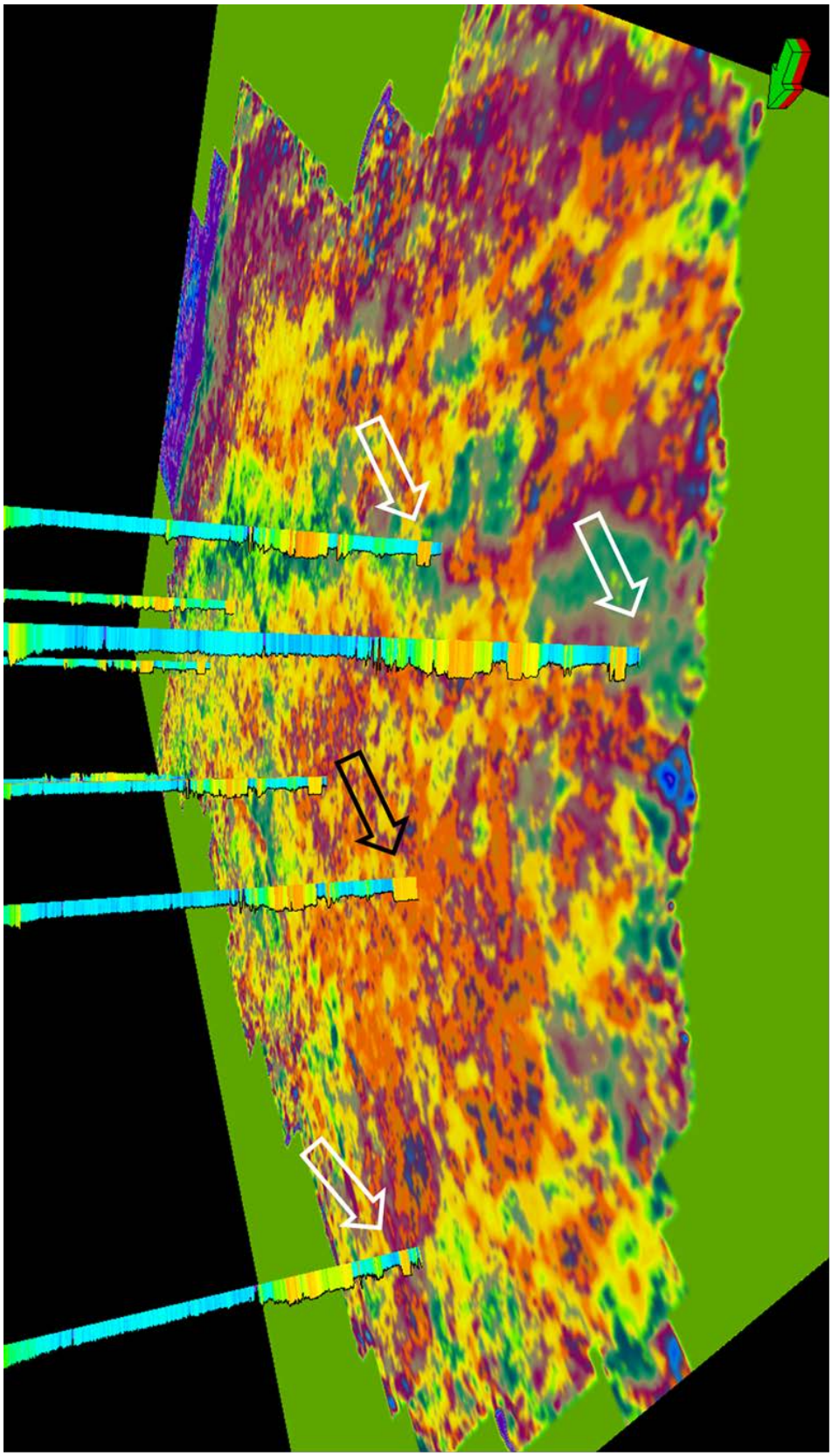

Figures 50. 3D view of the match between log response and the resulting seismic facies classification.

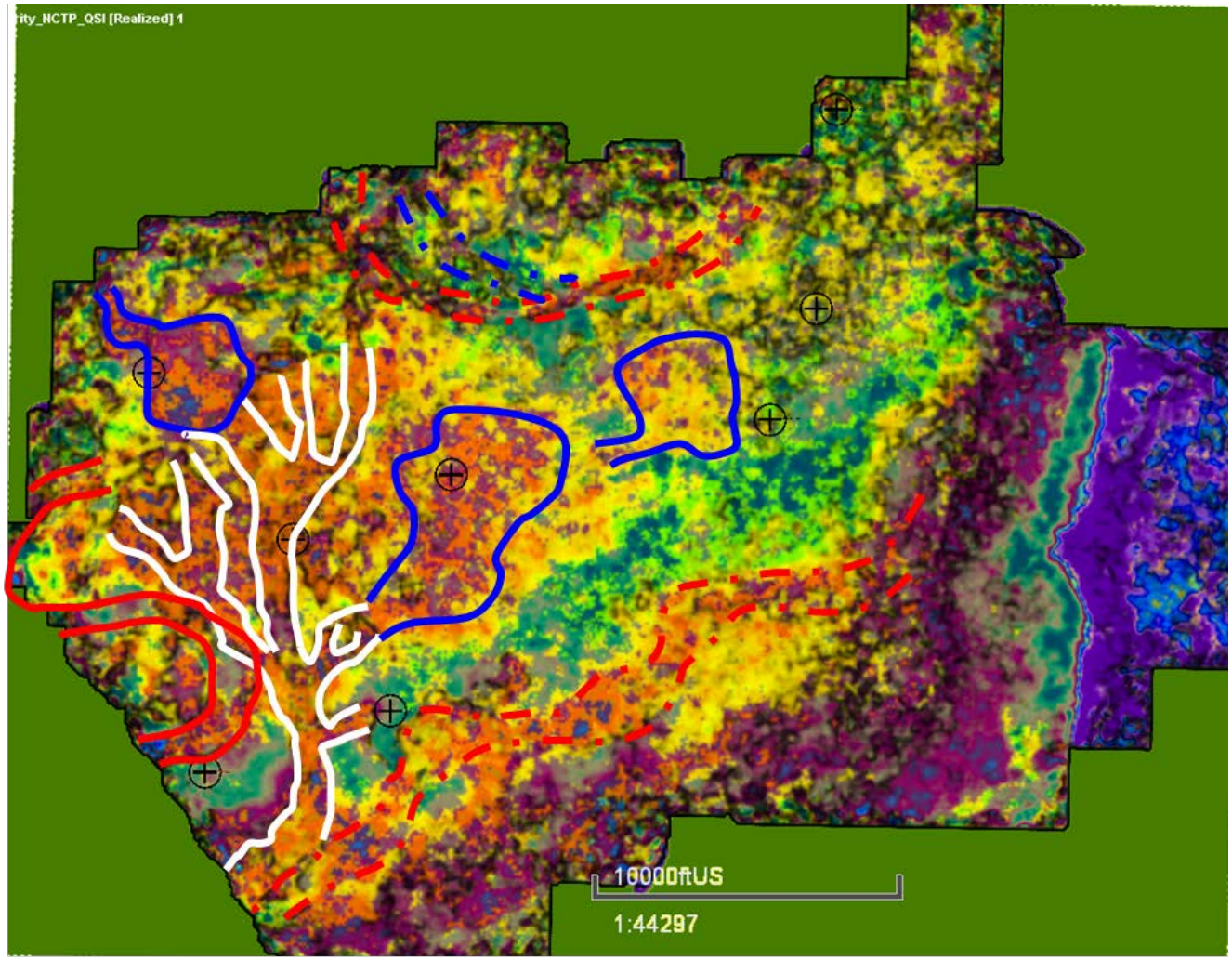

Figures 51. Sketch showing a possible architectural elements interpretation resulting from previous processes on a proportional slice.

Chapter 6: Results and Discussion

From the seismic facies classification processes, the supervised method (principal support vector machines_PSVM) that use seismic and well log data showed good results doing a binary classification between sandstone (reservoir) and mudstone. This outcome honors the well log information and depending on the quality of the seismic information, can better image and discriminate the classes. Furthermore, and just from the perspective obtained from this workflow, this supervised binary classification can be the foundation for a more complex seismic facies discrimination by merging its results with the impedance and rock physics attributes extracted from simultaneous inversion. Thus, it is feasible not only to discriminate seismic facies (sandstones and mudstones) but also variations along them like those seen on Figure 51 in which it is possible to interpret that though the yellow color is discriminating sandstones, the P-impedance attribute can be discriminating coarsening areas of the architectural elements and also boundaries among them.

The foundation of the outcome from this supervised method (PSVM) comes from two main points:

The training file used as input for classification which corresponds to the lithological discrimination between sandstones and mudstones based on the Gamma-ray value in each well (sandstone: GR<100 API); mudstone GR>101API). In this case a Gamma-ray value of 100 corresponds to a very very fine sandstone.

The relative stratal location. The target interval is the Lower Strawn Formation. This interval was used as training file boundary, a constrain that limits the results only to the target unit.

In this sense, the results from the supervised principal support vector machines method provided a reliable geological meaning that, combined with attribute maps, can help to better image the reservoir characteristics. Notwithstanding, the results from the unsupervised processes can be used as insights in case well log information is not available because their results are not far from those obtained by supervised methods.

The use of P-impedance, S-impedance and elastic attributes can pave the path towards a more quantitative interpretation. For this thesis, by using principal components analysis to reduce the dimensionality of the input attributes, P-impedance was found to be the most contributing attribute to the total variability of the data and was used to find differences along the supervised seismic facies classification. Furthermore, these rock physics attributes can be used to map heterogeneities and characterize changes within the target unit.

On the other hand, by analyzing the evolution and behavior of the sand bodies through geologic time, different sources of sediments can be inferred. As previously seen from regional geology, Gun (1979) stated that the sediment present along the Knox-Baylor Trough can come in part from the Muenster-Wichita mountain system; however, from these seismic facies analysis made with the data set available, it is possible to propose other directions for the source of sediments that were deposited on this specific area of the Knox-Baylor Trough. Figure 53 a-e shows a cartoon with the time-evolution of the sand bodies and main features present within the survey. From this, at least three source directions can be inferred: from north, from south and from north-west. Each direction provided different

sand bodies. From this study, a north-east direction for the source of sediments could not be inferred and this could be interpreted as sediments coming from the Muenster-Wichita mountain system just started to fill into the Knox-Baylor Trough once the deepwater deposits were deposited in early Desmoinesian time. That means that the deposits that were analyzed are not the same sandstone bodies that Gun (1979) studied. This could make sense since Brown (1973) stated that the Lower Strawn deposits are associated with slope depositional systems. If those deposits that were analyzed by Gun (1979) are associated with slope depositional systems, the sand bodies described in this thesis are older and can correspond to deposits of the deepest part of the basin. Also, this idea makes sense to propose a sequence stratigraphic framework for the Desmoinesian-Missourian interval (Figure 54-55) in which the poorly studied Lower Strawn deposits are related to deep water settings and the overlying strata correspond to the extensively studied Upper Strawn Formation deltaic deposits; all occurring within one major sea level cycle of Lowstand through Highstand.

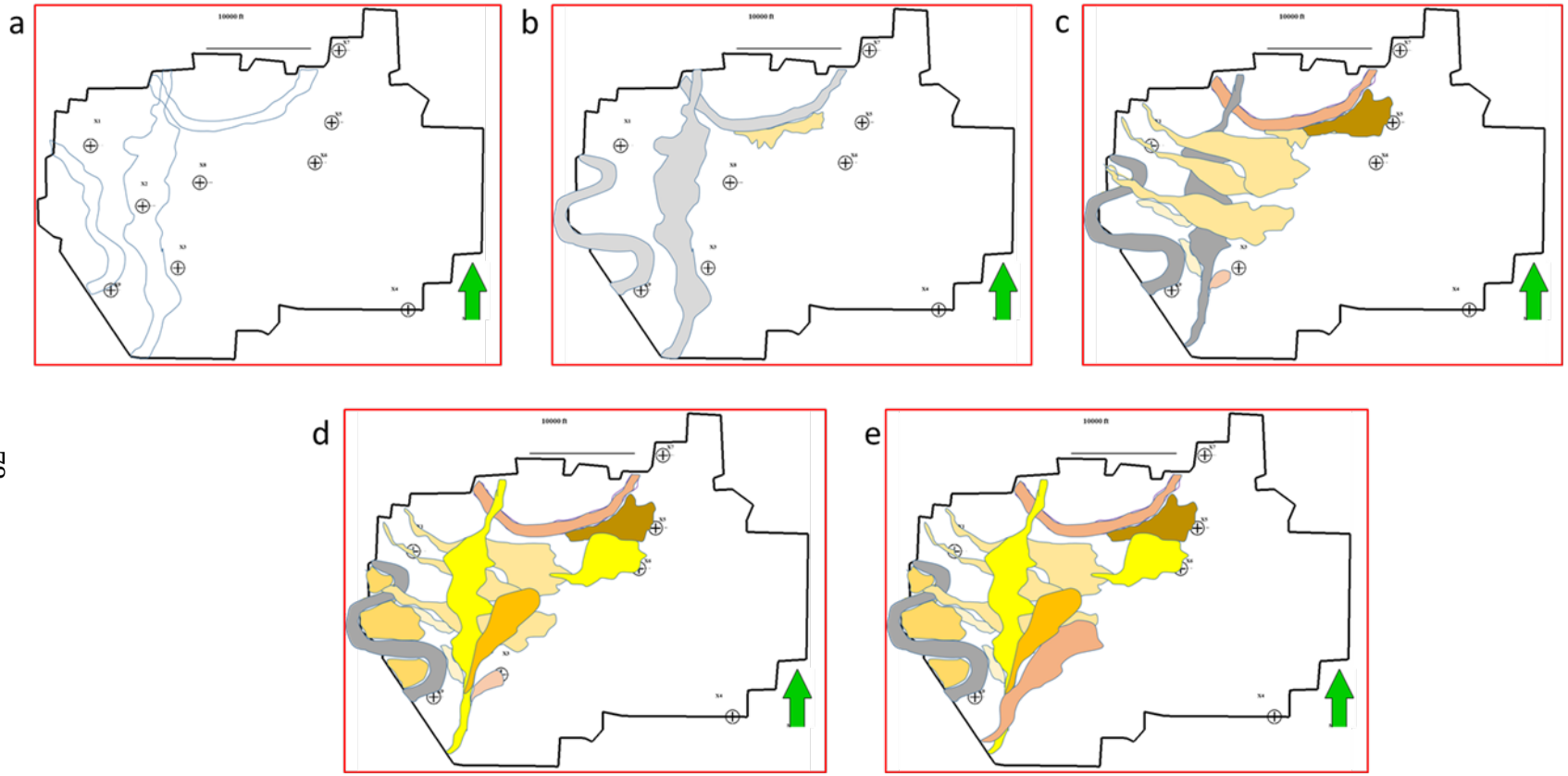

Figures 53. a) Early stages of channel-carving and sinuous meandering channel. b) Carved features started to fill with mudstone and some sand as overbank deposits. c) Fan features start coming from a north-west direction and also some pulses of sand sedimentation from the south form levee deposits. d) and e) Pulses of sand coming from the north and south start filling the main channel complex as well as the sinuous meandering channel starts forming point bars.

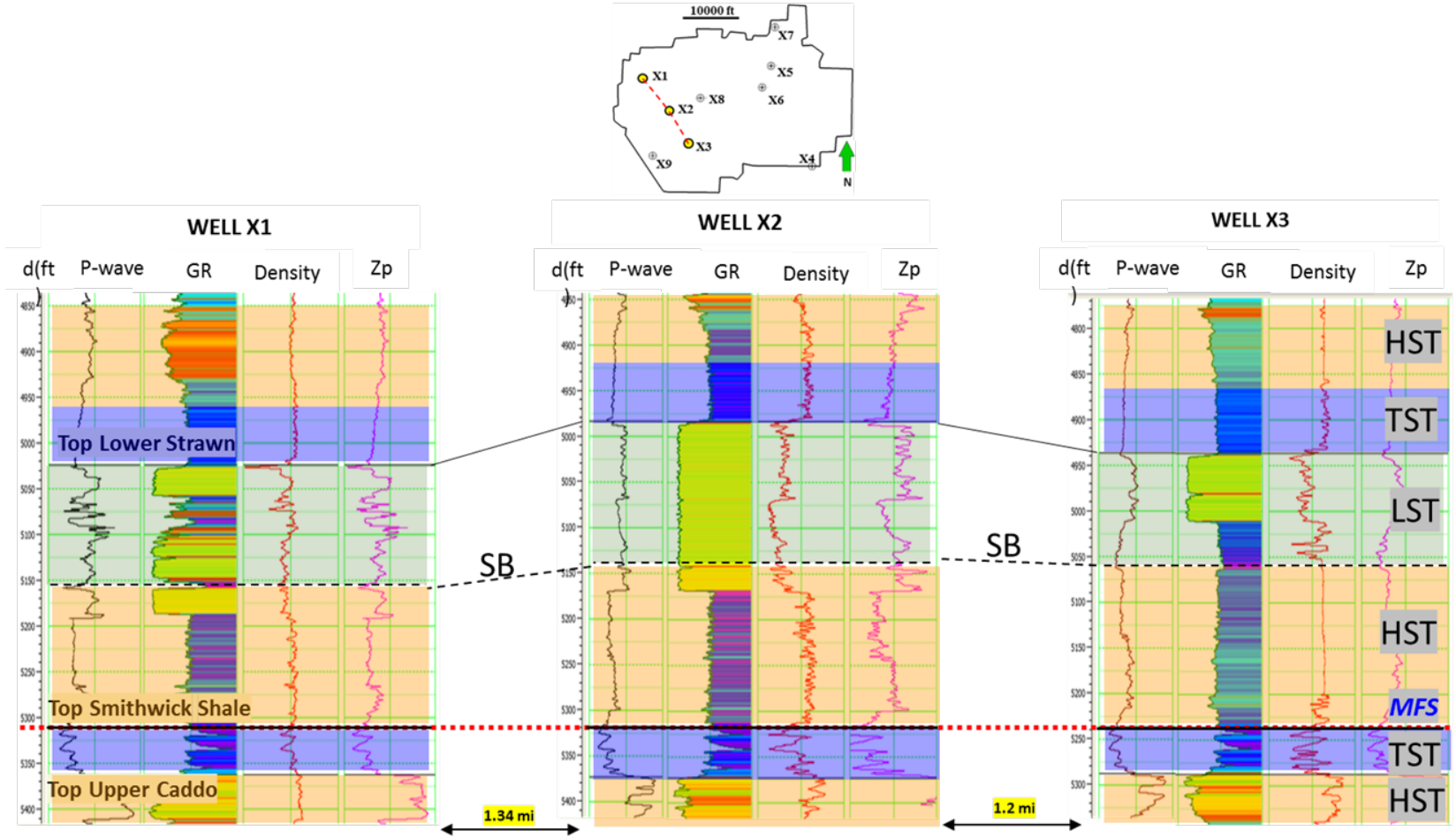

Figures 54. Proposed sequence stratigraphic framework for the study area for the wells X1, X2 and X3.

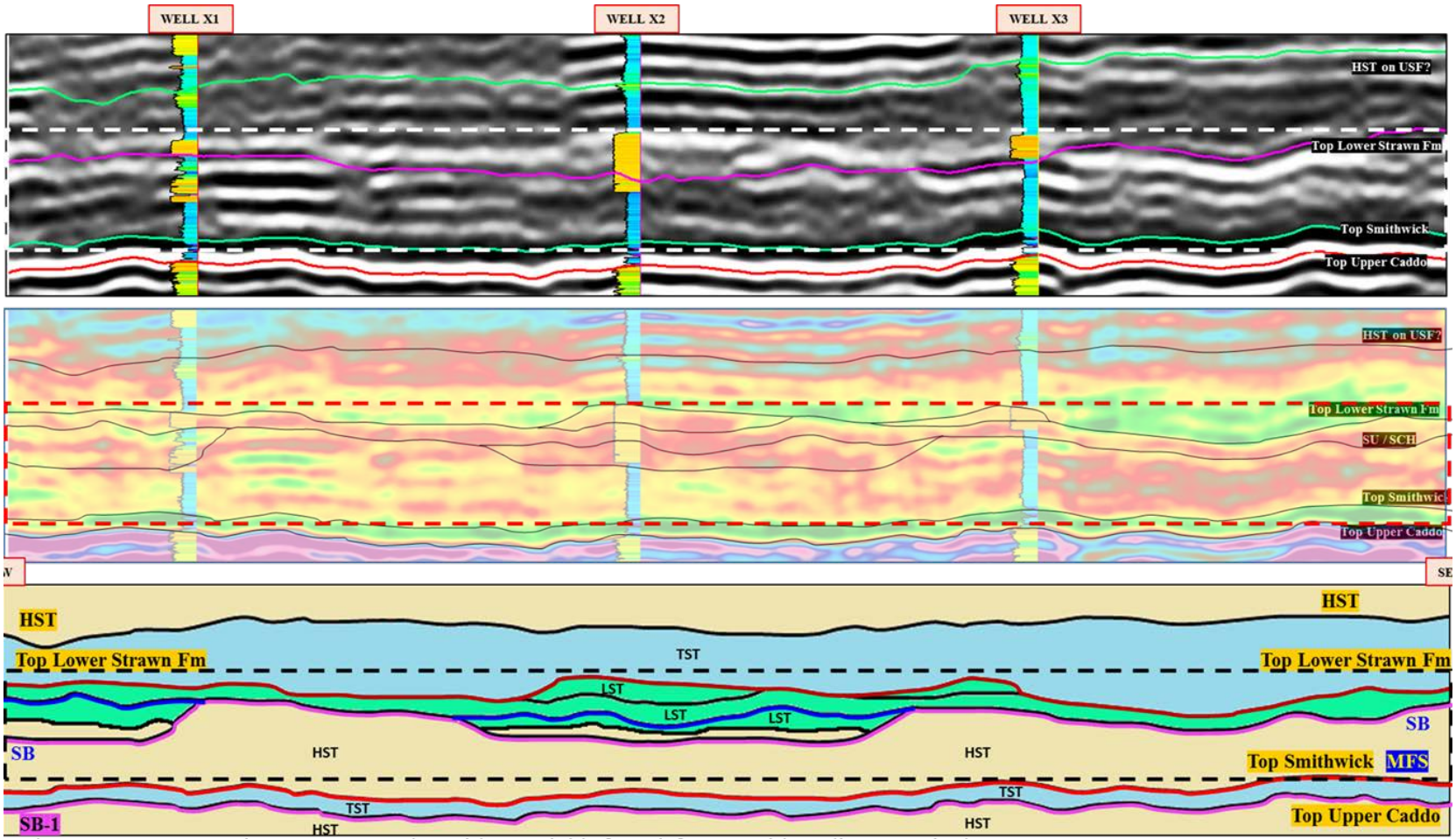

Figures 55. Proposed Sequence stratigraphic model inferred from multi-attribute analysis.

HST TST LST SB MFS

Chapter 7: Conclusions and Limitations

From the results obtained through the development of this workflow, it is possible to propose a new set of directions for the source of Desmoisnesian Lower Strawn Formation sediments in Knox-Baylor basin. A south to north direction of a channel complex geometry has been imaged along with a set of architectural elements from the seismic facies classification obtained from supervised principal support vector machines method (PSVM). Another source of sediments came from the north-west in the form of fan deposits with a partial input from the north (Brown, 1973; Gun, 1979). Even if the sand bodies of the Lower Strawn Formation in north-central Texas are areally extensive, they are the product of continuous pulses of sediments from multiple directions. Thus, thicker sandstones are located at the intersections of these different depositional events.

Due to the lack of seismic resolution within the target unit (Lower Strawn Formation), a conventional seismic approach to visualize the architectural elements and the location and directions of these sand bodies could not be performed. A novel set of machine learning techniques were used for quantitative seismic interpretation (Unsupervised and supervised seismic facies classifications). However, it was the supervised one (Principal support vector machines) with its binary classification (Sandstone and mudstone) combined with different attributes like P-impedance, which gave more confidence in the interpretation of stratigraphic features (architectural elements), their heterogeneities and their evolution through the time within the Lower Strawn Formation.

From the fact that the overlying deposits of the Upper Strawn Formation have been extensively characterized as deltaic deposits, the evolution and geomorphological characteristics of the sand bodies analyzed in this thesis (channel complex, fans, levees, sinuous channels), a sequence stratigraphic framework is proposed for the target unit in which the deepwater nature for the Lower Strawn Formation can be inferred.

Finally, to improve the results of this study, map heterogeneities and characterize changes, the recommendation is to perform the workflow presented in this thesis by using the seismic volumes product of simultaneous elastic inversion (pre-stack inversion) along with the conditioned well logs. Running the process with elastic inputs (P-impedance, S-impedance and Density) will provide a better image of the depositional events present, giving a more reliable seismic-stratigraphic interpretation that can lead to the building of a better seismic facies classification, and a more robust sequence stratigraphic framework for the whole Strawn Formation. Also the use of other seismic volumes within the area of study can lead to a more regional geological model avoiding misinterpretations due to the small size of the current survey.

References

Ball, M. M., and W. J. Perry, 1996, Bend Arch– Fort Worth Basin province (045), in D. L. Gautier, G. L. Dolton, K. I. Takahashi, andK. L. Varnes, eds., 1995 national assessment of United States oil and gas resources— Results, methodology, and supporting data: U.S. Geological Survey Digital Data Series DDS-30, release 2, CD-ROM.

Brown, L. F., Jr., Cleaves, A. W., II, and Erxleben, A. W., 1973, Pennsylvanian depositional systems in north-central texas—a guide for interpreting terrigenous clastic facies in a cratonic basin: The University of Texas at Austin, Bureau of Economic Geology Guidebook 14, 122 p.

Burgess, W. J., 1976, Geologic evolution of mid-continent and Gulf Coast areas; plate tectonics view: Gulf Coast Association of Geological Societies Transactions, v. 26, p. 132–143.

Charma, R. K., and S. Chopra, 2013, Poisson Impedance: A promising tool for determination of sand quality: GeoConvention 2013: Integration.

Chopra, S., and K.J. Marfurt, 2007, Seismic attributes for prospect identification and reservoir characterization: Society of Exploration Geophysics.

Chopra, S., and K.J. Marfurt, 2014, Seismic facies analysis using generative topographic mapping: SEG Denver 2014 Annual Meeting.

Cleaves, A., 1982, Upper Strawn depositional systems of northcentral Texas, in C. A. Martin, ed., Petroleum geology of the Fort Worth Basin and Bend Arch area: Dallas Geological Society, p. 49– 95.

Cortes, C., and V. Vapnik, 1995, Support-vector networks: Machine Learning, 20, 273–297, doi: 10.1023/A:1022627411411.

Flawn, P. T., A. Goldstein, Jr., P. B. King, and C. E. Weaver, 1961, The Ouachita system: University of Texas, Bureau of Economic Geology, Report 6120, 401 p., 6 sheets.

Flippin, J. W., 1982, The stratigraphy, structure, and economic aspects of the Paleozoic strata in Erath County, north central Texas, in C. A. Martin, ed., Petroleum geology of the Fort Worth Basin and Bend Arch area: Dallas Geological Society, p. 129–155.

Gunn, R.D., 1979, Desmoinesian depositional systems in the Knox-Baylor Trough, in Hyne, N.J., ed., Pennsylvanian sandstones of the Mid-continent: Tulsa, OK, Tulsa Geological Society, p. 221-234.

Henry, J. D., 1982, Stratigraphy of the Barnett Shale (Mississippian) and associated reefs in the northern Fort Worth Basin; in C. A. Martin, ed., Petroleum geology of the Fort Worth Basin and Bend Arch area: Dallas Geological Society, p. 157– 178.

Kerans, C., 1988, Karst-controlled reservoir heterogeneity in Ellenburger Group carbonates of west Texas: AAPG Bulletin, v. 72, p. 1160– 1183.

Kohonen, T., 2001, Self-organizing maps (3rd ed.): Springer-Verlag.

Lahti, V. R. and W. F.Huber, 1982, The Atoka Group (Pennsylvanian) of the Boonsville field area, north-central Texas, in C. A. Martin, ed., Petroleum geology of the Fort Worth Basin and Bend Arch area: Dallas Geological Society, p. 377– 400.

Lovick, G. P., C. G. Mazzine, and D. A. Kotila, 1982, Atokan clastics; depositional environments in a foreland basin, in C. A. Martin, ed., Petroleum geology of the Fort Worth Basin and Bend Arch area: Dallas Geological Society, p. 193– 211.

Montgomery, S. L., D. M. Jarvie, K. A. Bowker, and R. M. Pollastro, 2005, Mississippian Barnett Shale, Fort Worth Basin: North-central Texas: Gas-shale play with multi-tcf potential: AAPG Bulletin, v. 89, p. 155–175.

Pranter, M. J., 1989, Facies analysis of the strawn submarine fan complex, Fort Worth Basin, central Texas. Master's thesis, Baylor University, 143 p.

Pollastro, R. M., R. J. Hill, D. M. Jarvie, and M. E. Henry, 2003, Assessing undiscovered resources of the Barnett– Paleozoic total petroleum system, Bend Arch– Fort Worth basin province, Texas (abs.): AAPG Southwest Section Convention, Fort Worth Texas, MArch 1– 5, 2003, 18 p.

Pollastro, R. M., D. M. Jarvie, R. J. Hill, and C. W. Adams, 2007, Geologic framework of the Mississippian Barnett Shale, Barnett- Paleozoic total petroleum system, Bend Arch–FortWorth Basin, Texas: AAPG Bulletin, v. 91, no. 4, p. 405–436.

Quakenbush, M., B. Shang, and C. Tuttle, 2006, Poisson impedance: The Leading Edge, 25, no. 2, 128–138.

Ray, A. K., and S. Chopra, 2016, Building more robust low-frequency models for seismic impedance inversion: First Break, volume 34, May 2016.

Roden, R., S. Thomas, and D. Sacrey, 2015, Geologic pattern recognition from seismic attributes: Principal component analysis and self-organizing maps: Interpretation, Nov 2015.

Roden, R., 2015, Distillation of seismic attributes to geologic significance: Offshore technology conference, 2015.

Sabeti, H., and A. Javerian, 2009, Seismic Facies Analysis Based on K-means Clustering Algorithm Using 3D Seismic Attributes: EAGE International Petroleum Conference and Exhibition , May 2009.

Sloss, L. L., 1976, Areas and volumes of cratonic sediments, western North America and Eastern Europe: Geology, v. 4, p. 272– 276.

Tai, D. T. W., 1979, Subsurface study of Atoka (lower Pennsylvanian) clastic rocks in parts of Jack, Palo Pinto, Parker, and Wise counties, north-central Texas: AAPG Bulletin, v. 63, p. 50– 66.

Thompson, D. M., 1982, Atoka Group (lower to middle Pennsylvanian), northern Fort Worth Basin, Texas: Terrigenous depositional systems, diagenesis, and reservoir quality: University of Texas, Bureau of Economic Geology, Report of Investigations, v. 125, 62 p.

Thompson, D. M., 1988, Fort Worth Basin; in L. L. Sloss, ed., The geology of North America: Geological Society of America, v. D-2, p. 346–352.

Tian, et. al., 2010, Reservoir prediction using Poisson Impedance in Quinhuangdao, Bohai Sea: SEG Denver 2010 Annual Meeting, 2261-2264.

Turner, G. I., 1957, Paleozoic stratigraphy of the Fort Worth Basin, in W. C. Bell, ed., Abilene and Fort Worth Geological Societies Joint Field Trip Guidebook, p. 57– 77.

Van-Wagoner, J., 1975, Paleoenvironmental analysis of the lower middle Pennsylvanian deep-water sediments Forth worth basin, Central Texas. Master's thesis, Rice University, May 1975.

Walper, J. L., 1977, Paleozoic tectonics of the southern margin of North America: Gulf Coast Association of Geological Societies Transactions, v. 27, p. 230–239.

Walper, J. L., 1982, Plate tectonic evolution of the Fort Worth Basin, in C. A. Martin, ed., Petroleum geology of the Fort Worth Basin and Bend Arch area: Dallas Geological Society, p. 237–251.

Zhao, T., V. Jayaram, K. J. Marfurt, and H. Zhou, 2014, Lithofacies classification in Barnett Shale using proximal support vector machines: 84th Annual International Meeting, SEG, Expanded Abstracts, 1491–1495.

Zhao, T., V. Jayaram, A. Roy, and K. J. Marfurt, 2015, A comparison of classification techniques for seismic facies recognition: Interpretation, 3, SAE29–SAE58, doi: 10.1190/INT-2015-0044.1.

Appendix: Additional Figures

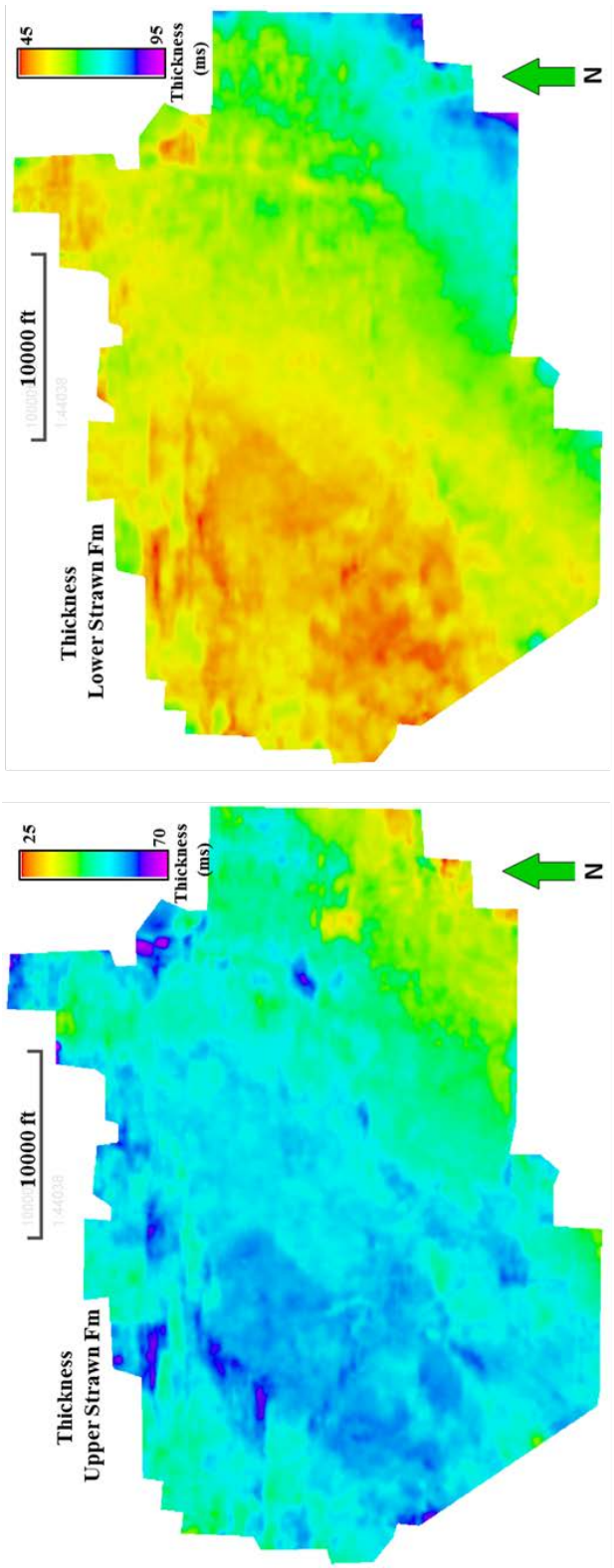

Figure A1. Thickness maps of Upper and Lower Strawn formations. Note the North-East area where the thickness of the Lower Strawn Fm increases, the thickness of the Upper Strawn Fm decreases.

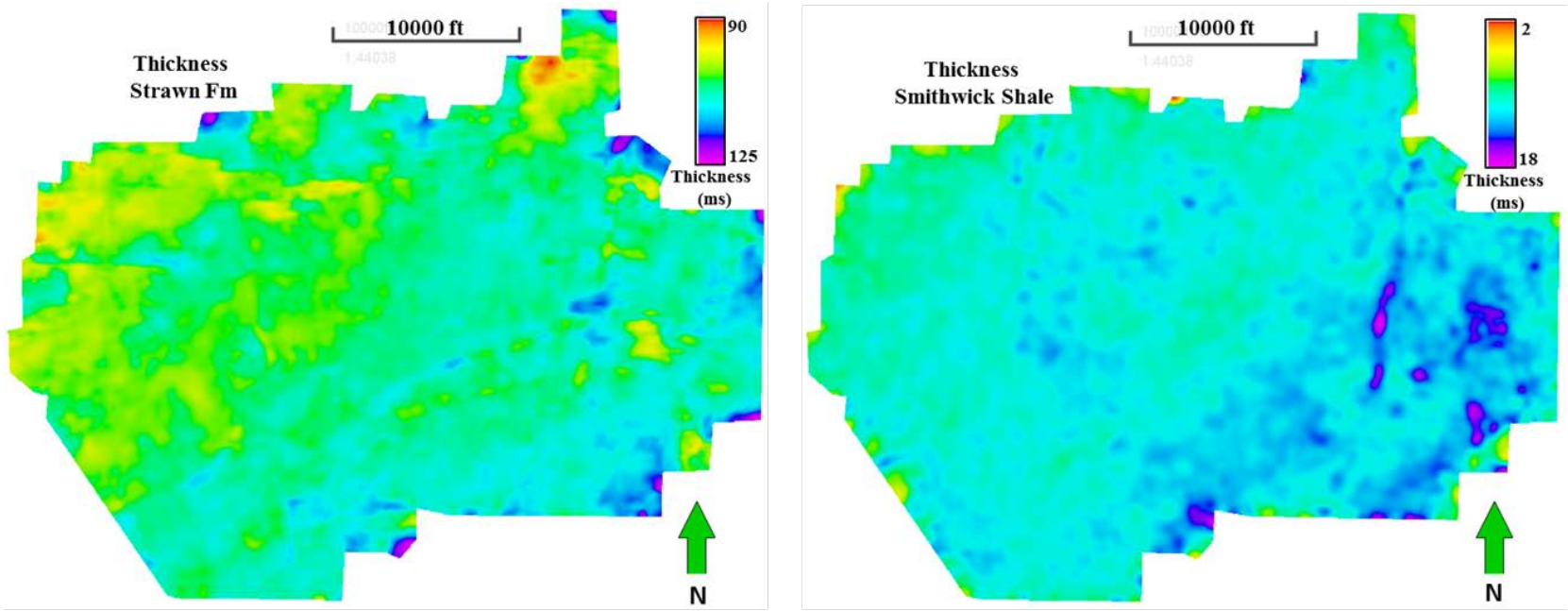

Figure A2. Thickness maps of the Strawn Formation and Smithwick shale.

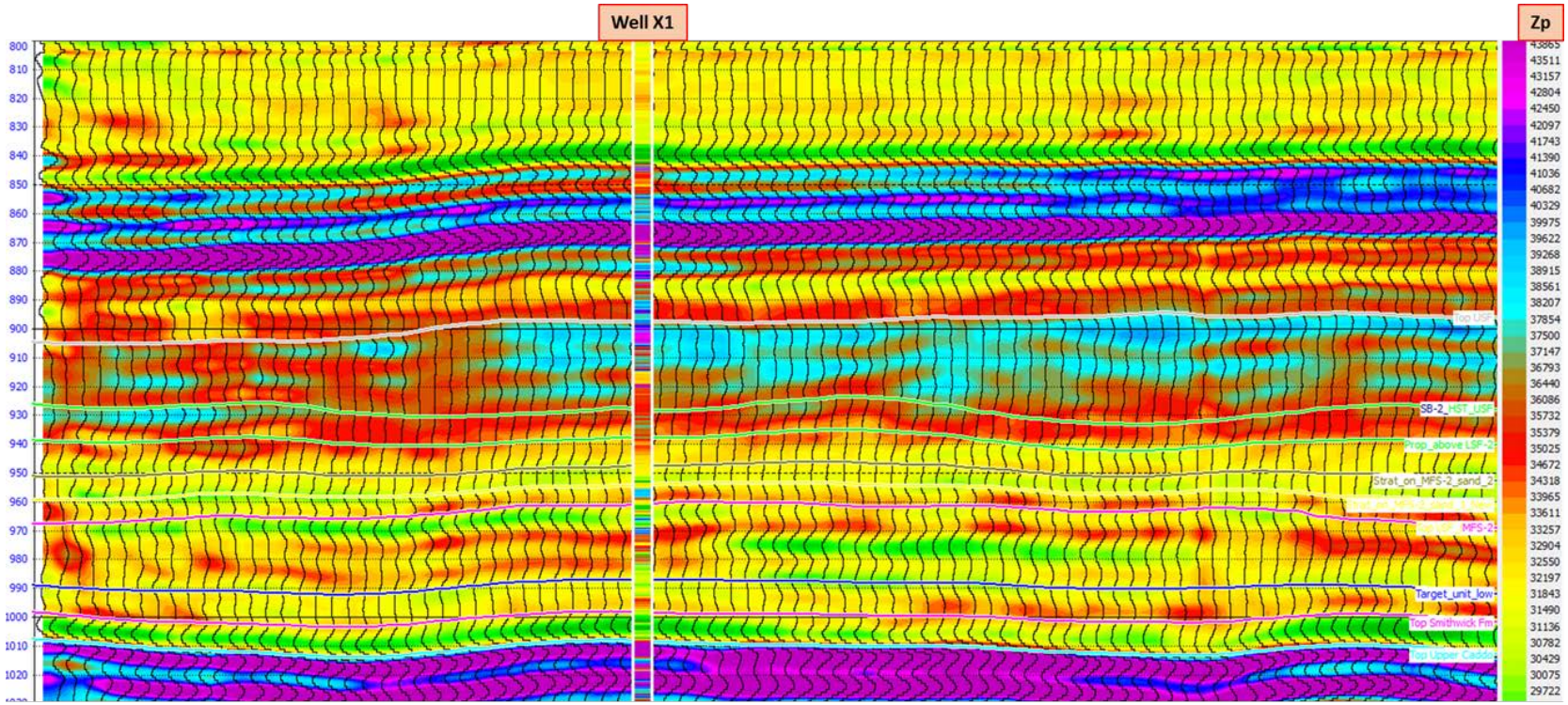

Figure A3. P-impedance inversion results showing well X1.

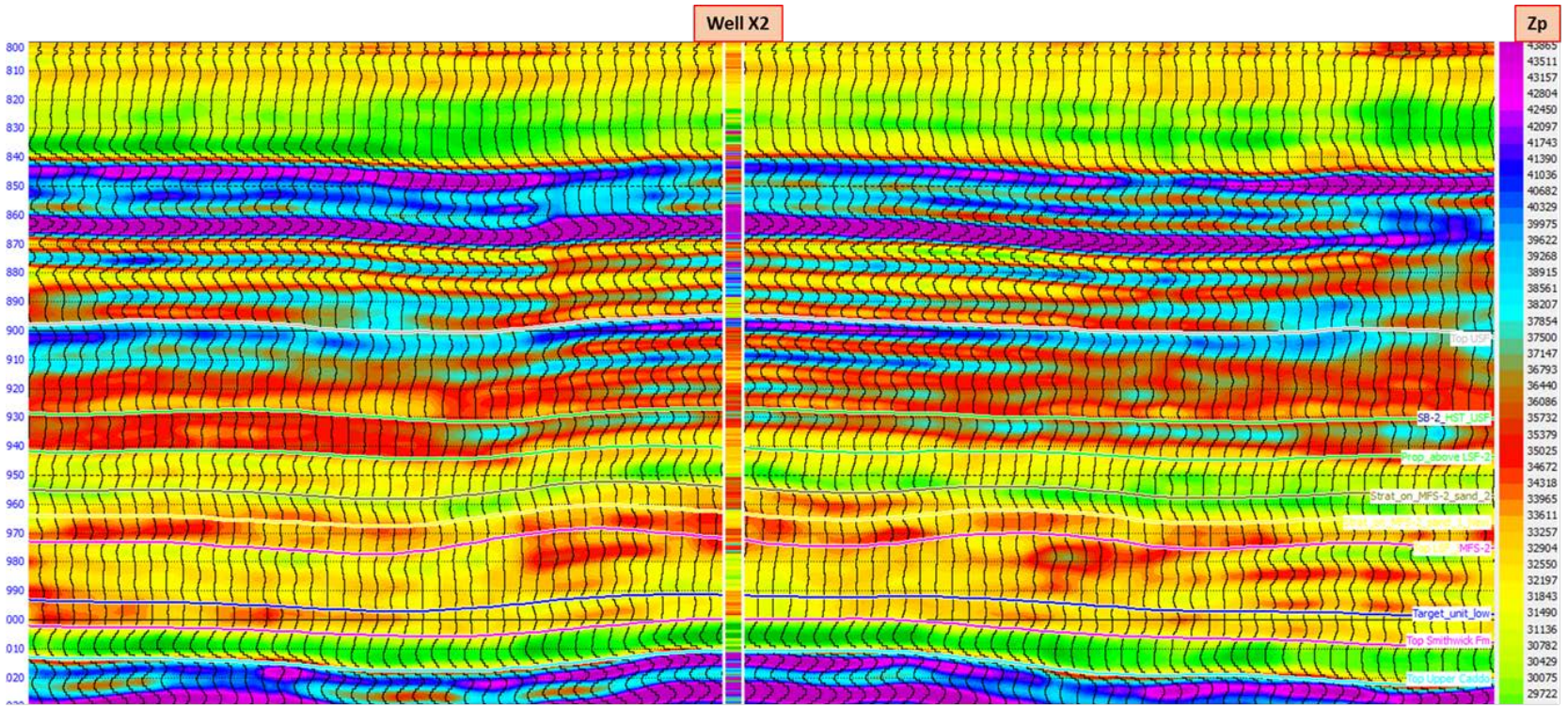

Figure A4. P-impedance inversion results showing well X2.

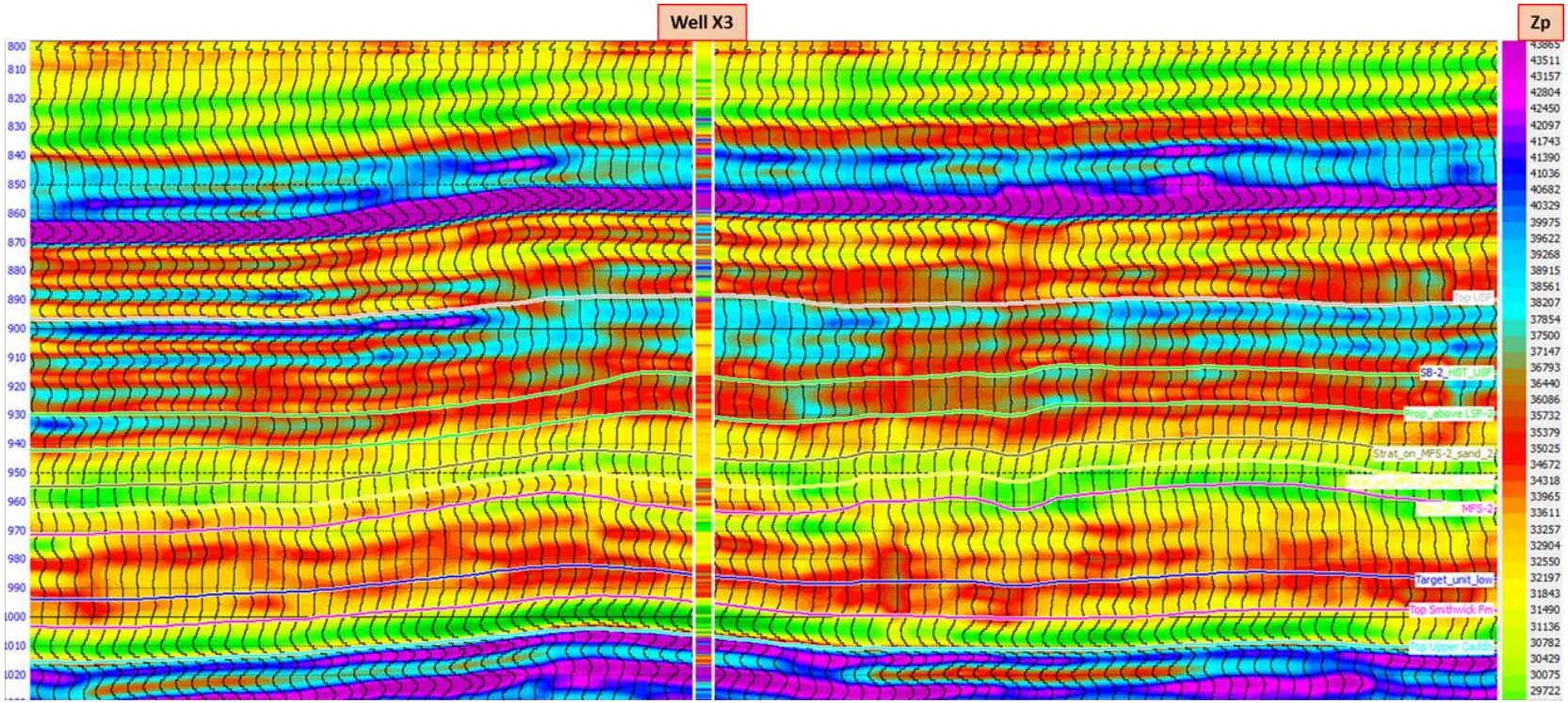

Figure A5. P-impedance inversion results showing well X3.

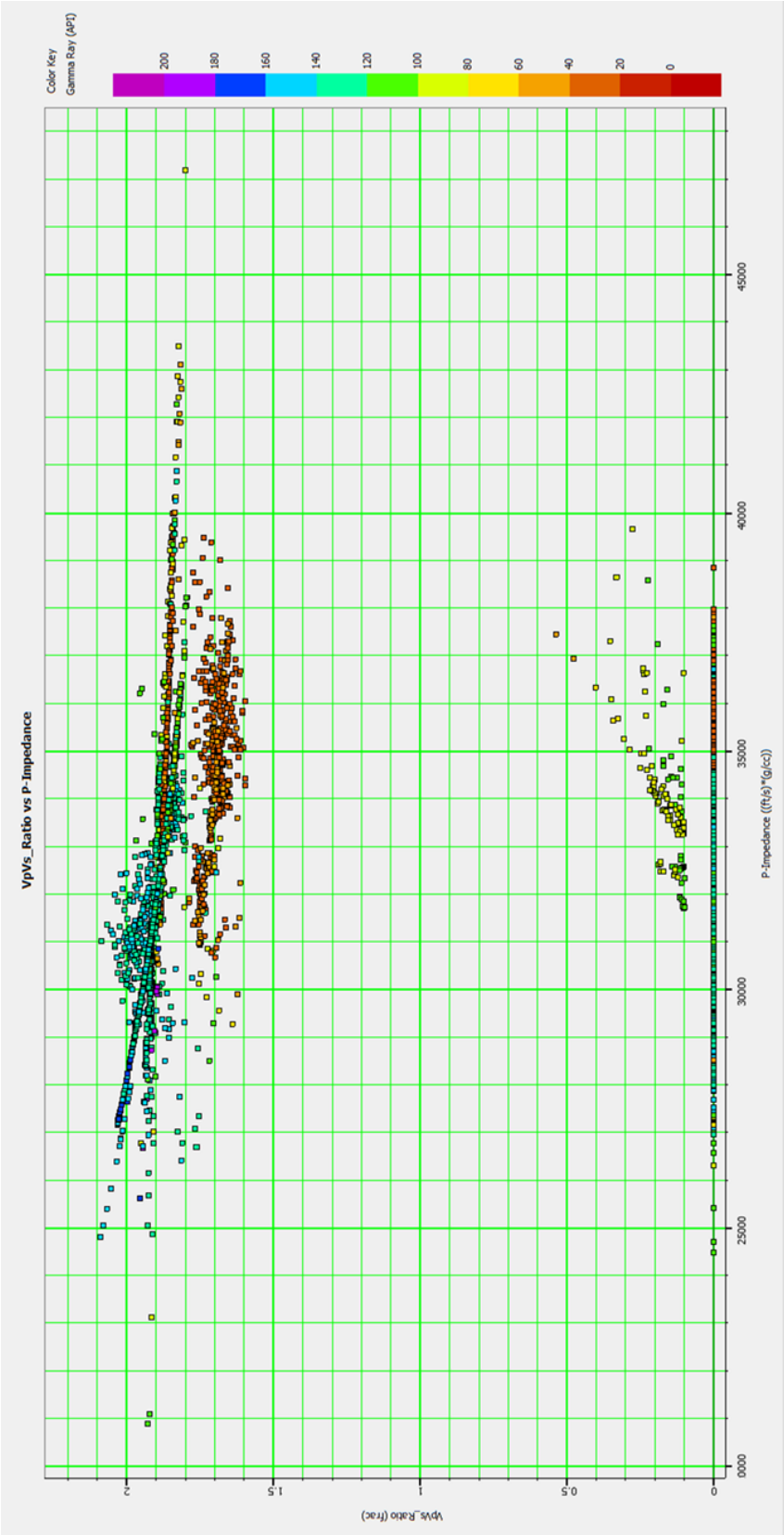

Figure A6. Vp/Vs vs Zp cross-plot from wells used for inversion. Gamma-ray value as color bar.

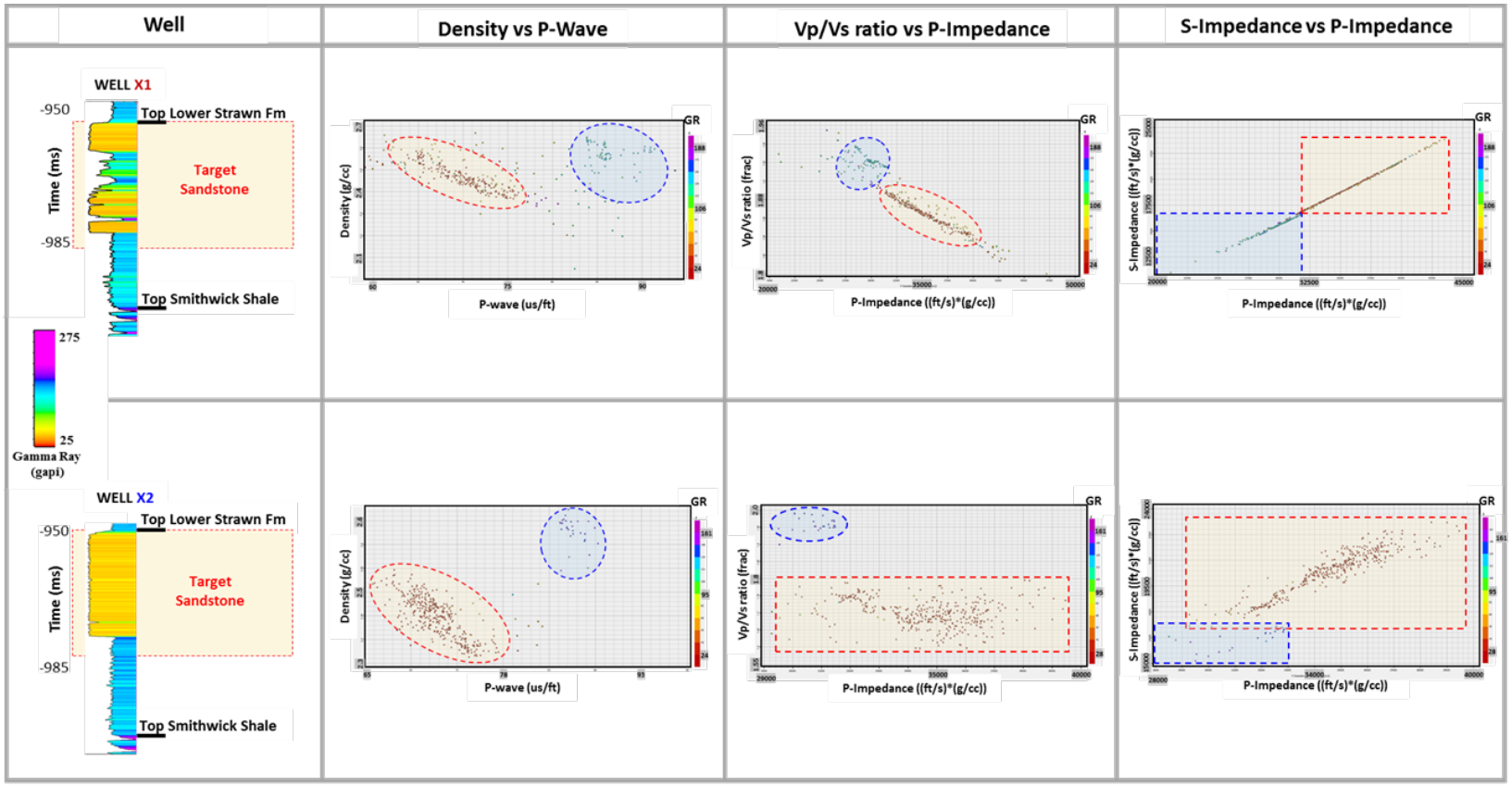

Figure A7. From left to right, wells showing Gamma-ray response over the target sandstone. Cross plots show the following relationships: Density vs. P-wave, Vp/Vs vs. P-impedance, and S-impedance vs. P-impedance constrained on this specific interval. Circles represent the possible discrimination of sandstone (light yellow) and mudstones (light blue). Vertical color bar corresponds to Gamma-ray values.

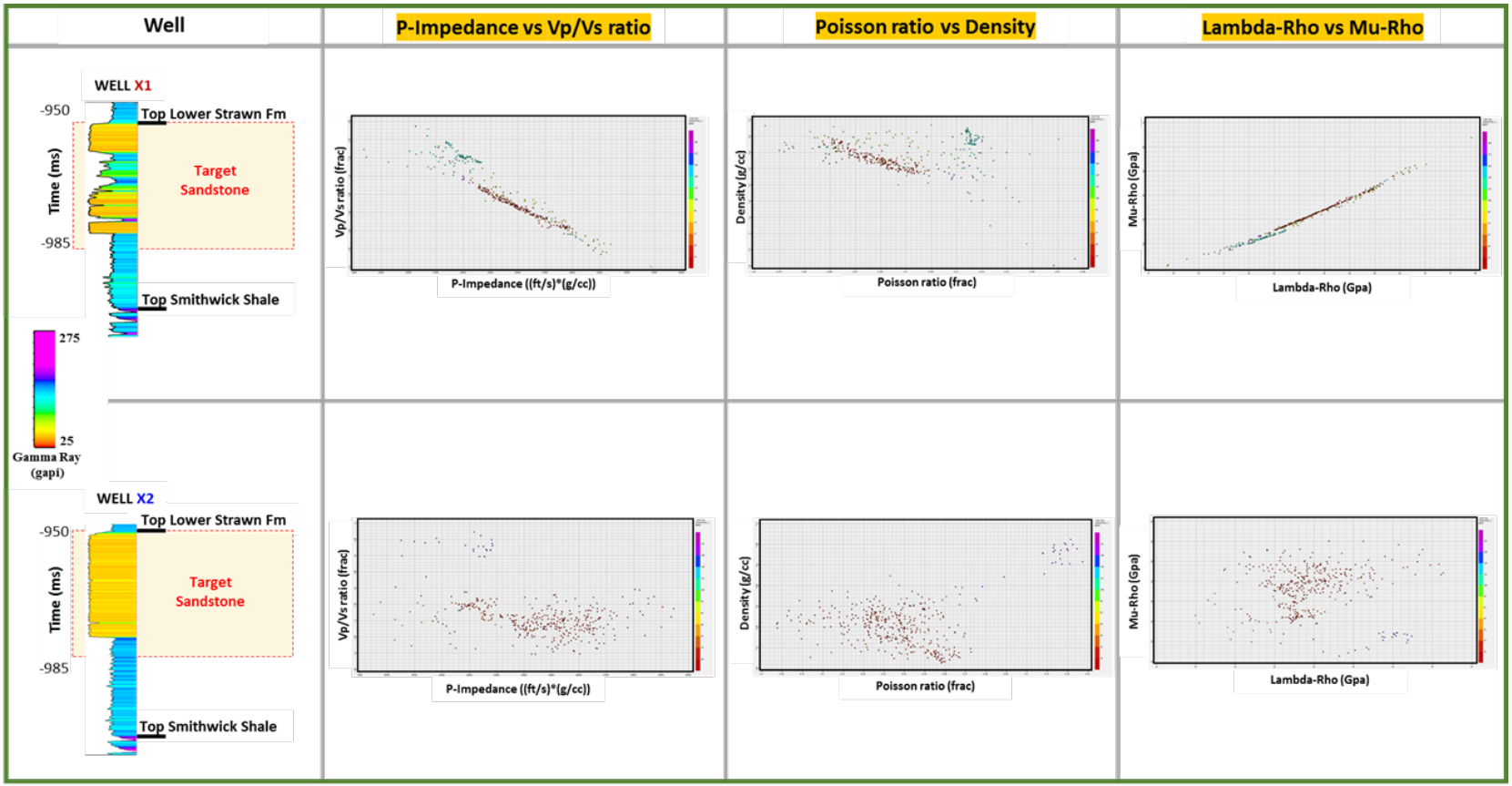

Figure A8. From left to right, wells showing Gamma-ray response over the target sandstone. Cross plots show the following relationships: Zp vs. Vp/Vs ratio; Poison ratio vs density, and Lambda-Rho vs Mu-Rho constrained on this specific interval. Vertical color bar corresponds to Gamma-ray values.

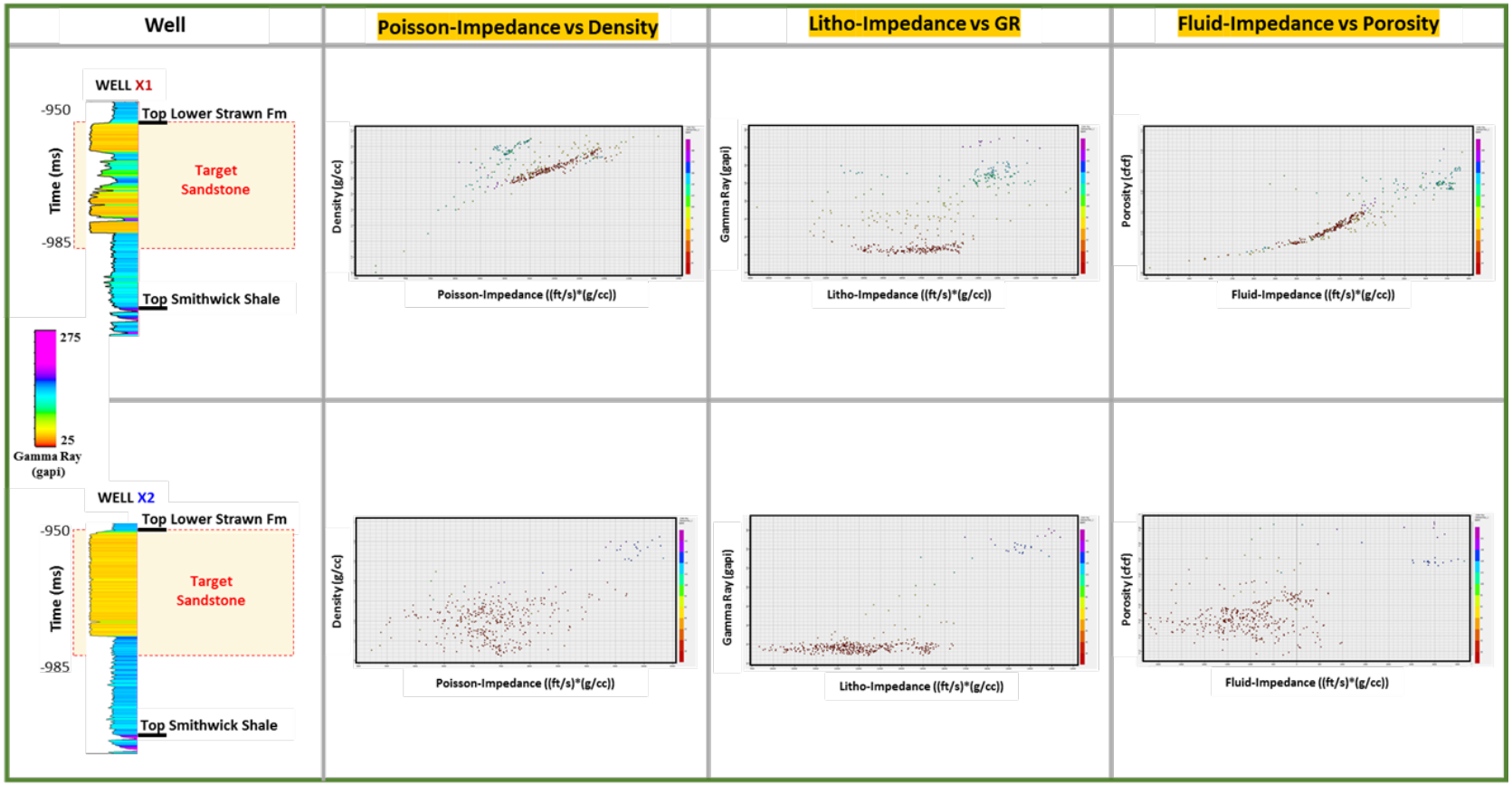

Figure A9. From left to right, wells showing Gamma-ray response over the target sandstone. Cross plots show the following relationships: Poisson Impedance vs density; Litho Impedance vs Gamma-ray, and Fluid Impedance vs porosity constrained on this specific interval. Vertical color bar corresponds to Gamma-ray values.

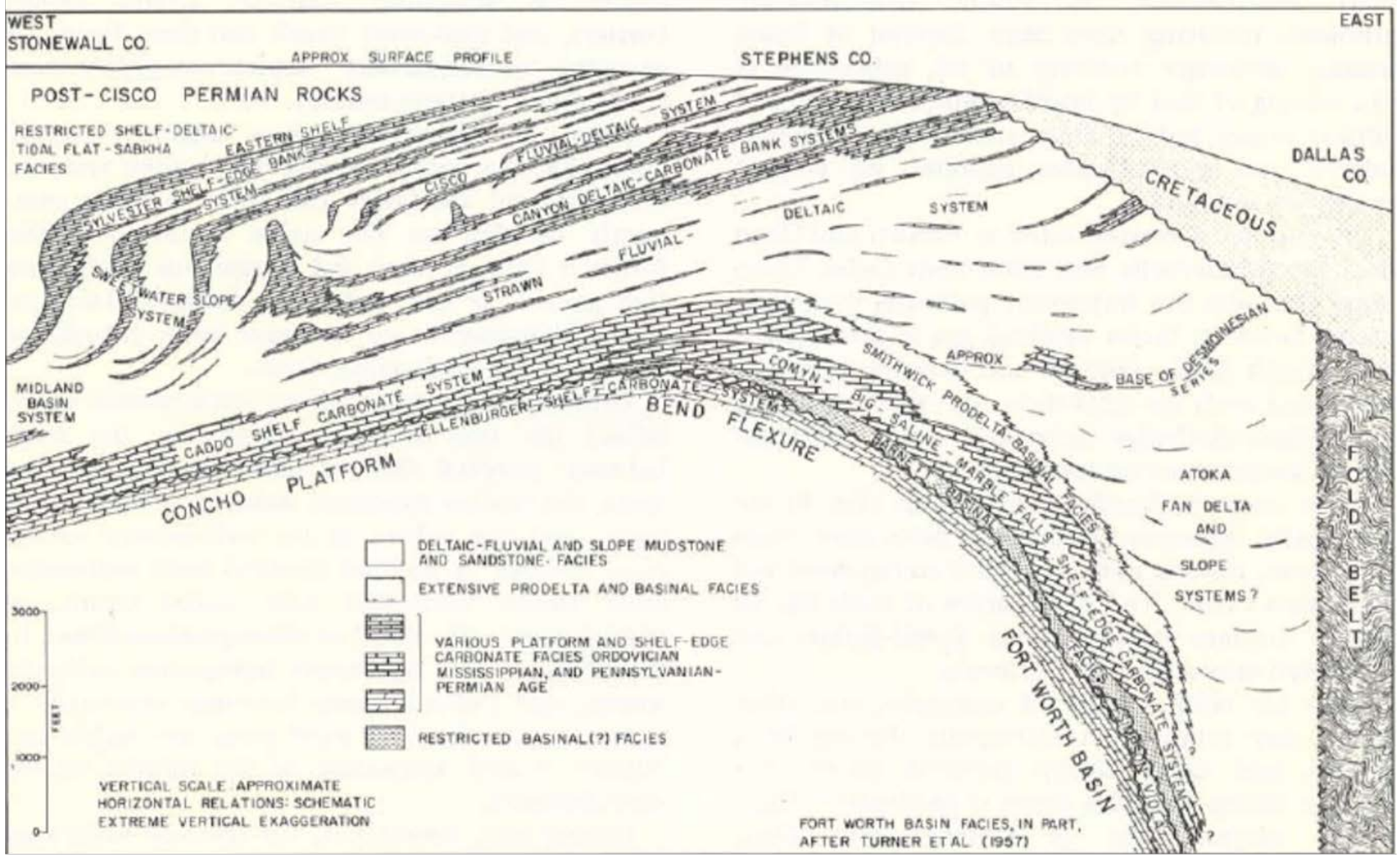

Figure A10. Evolution of depositional systems, North-Central Texas: Fort Worth Basin. (Brown et al, 1973)

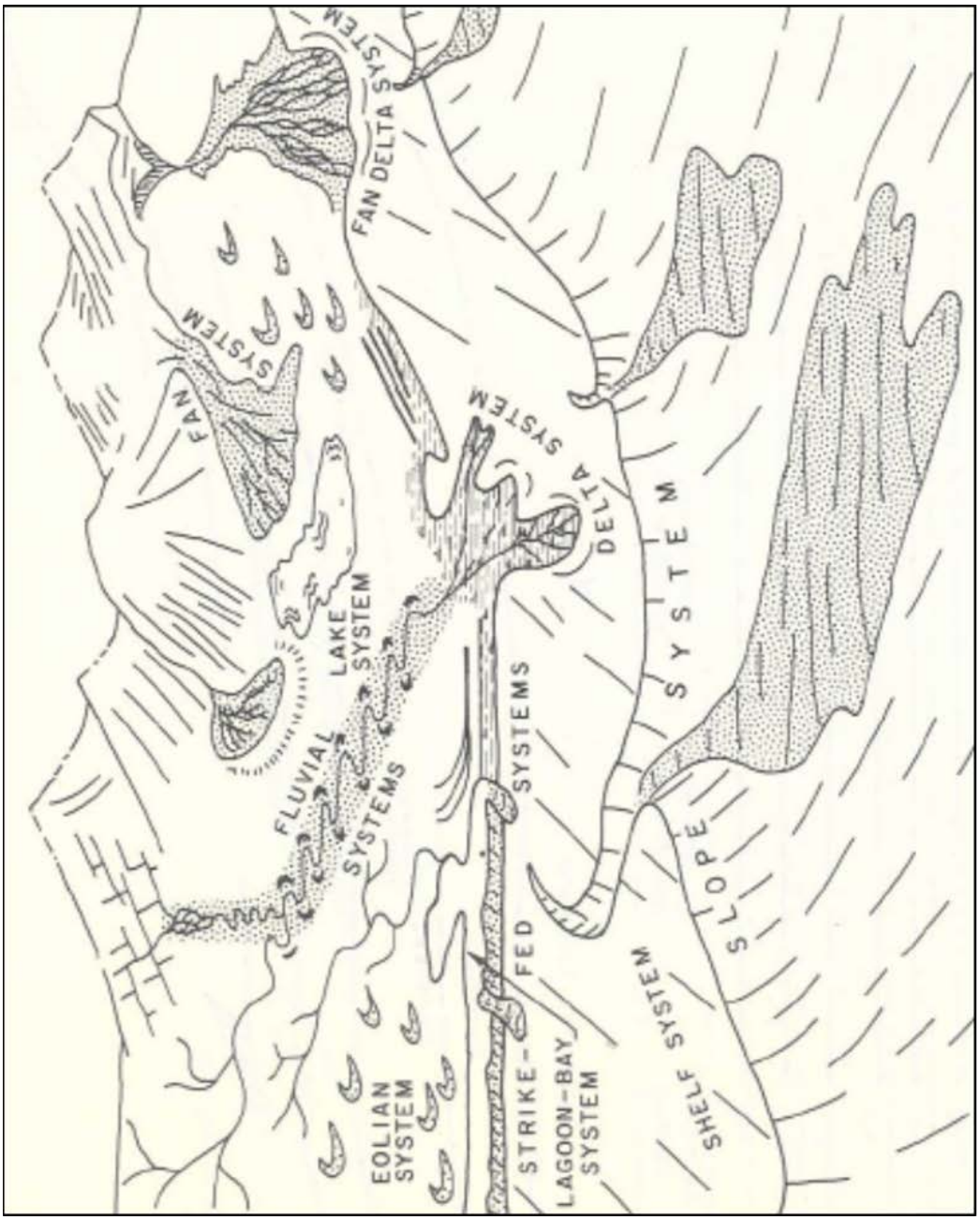

Figure A11. Schematic perspective of terrigenous depositional systems (Original by A.J. Scott. In Brown et al, 1973).